Clemson University
TigerPrints

All Dissertations | Dissertations

12-2014

The Effects of Secondary Trapping Mechanisms on Geologic Storage of Carbon Dioxide

Catherine Ruprecht
Clemson University, Cat.ruprecht@gmail.com

Follow this and additional works at: http://tigerprints.clemson.edu/all_dissertations

Part of the Environmental Engineering Commons

Recommended Citation
Ruprecht, Catherine, "The Effects of Secondary Trapping Mechanisms on Geologic Storage of Carbon Dioxide" (2014). *All Dissertations.* Paper 1284.

This Dissertation is brought to you for free and open access by the Dissertations at TigerPrints. It has been accepted for inclusion in All Dissertations by an authorized administrator of TigerPrints. For more information, please contact awesole@clemson.edu.

THE EFFECTS OF SECONDARY TRAPPING MECHANISMS ON GEOLOGIC STORAGE OF CARBON DIOXIDE

A Dissertation

Presented to

the Graduate School of

Clemson University

In Partial Fulfillment

of the Requirements for the Degree

Doctor of Philosophy

Environmental Engineering and Science

---

by

Catherine Marie Ruprecht

December 2014

Accepted by:

Dr. Ronald Falta, Committee Chair

Dr. Lawrence Murdoch

Dr. Sally Benson

Dr. Cindy Lee

ABSTRACT

The goal of this dissertation is to further the understanding of secondary trapping mechanisms in geologic CO_2 storage systems to improve storage design and security. This dissertation takes the form of three chapters. The objective of the first chapter was to analyze the storage performance of supercritical and brine saturated CO_2 injection strategies to determine their advantages and disadvantages on distribution and immobilization of CO_2 and pressure buildup. Results showed dissolved CO_2 injection was favorable in terms of storage security in all cases as it resulted in smaller areal extents on the caprock and did not migrate appreciably beyond the injection period. However, the distribution of dissolved CO_2 was more influenced by formation heterogeneities than supercritical CO_2. In cases with high permeability zones, the storage efficiency of dissolved CO_2 was less than supercritical CO_2. Supercritical CO_2 injection was favorable in highly heterogeneous dipping formations where trapping was enhanced. The second chapter presents results from an experimental investigation of hysteresis in residual trapping and relative permeability of CO_2 in a CO_2 /water system at 50ºC and 9 MPa in a Berea sandstone core. Three flooding cycles were completed at a constant total volumetric flow rate by incrementally increasing and decreasing the fractional flow rates of supercritical CO_2 and water. Results showed the CO_2 saturations trapped during wetting-phase imbibition increased with the maximum CO_2 saturations reached during each cycle. A linear model with coefficient 0.5 describes the nonwetting trapping relationship. The CO_2 relative permeability data can be represented well by making a minor modification to the Van Genuchten-Burdine relative permeability data to account

for hysteresis. The third chapter demonstrates an approach to optimizing CO_2 storage design by determining economically efficient injection strategies that increase storage security through enhanced secondary trapping mechanisms. Optimizations considered 5 different water/CO_2 co-injection strategies. These strategies were all compared to a base case of standard supercritical CO_2 injection. Results showed simultaneous water and gas injection, water alternating gas injection, and water flush strategies reduced costs and increased secondary CO_2 trapping. Dissolved CO_2 injection increased the cost, but trapped the most CO_2 by secondary mechanisms of any method. Ultimately, results may be used to design CO_2 injection strategies that take advantage of CO_2 trapping behavior.

DEDICATION

This dissertation is dedicated to my parents Sandy Knuth, Richard Ruprecht, and Daryl Knuth for working hard to provide me every opportunity to make this doctoral degree possible. I'd also like to thank Kimberly Ruprecht, Julie Gerdes, and Andrew Yonkofski for their constant support, motivation, and hours of proofreading. Lastly, I'd like to thank my little brother, Ricky Ruprecht, for teaching me to follow my dreams.

ACKNOWLEDGMENTS

I'd like to acknowledge my major advisor Dr. Ron Falta, who has mentored me for six years, from undergraduate research to my PhD. He has provided me with direction in my career and opportunities for growth as a scientist that I will always be grateful for. I'd also like to thank Dr. Larry Murdoch for inspiring me with his seemingly constant curiosity of the world around us. I'd like to thank my other committee members Dr. Sally Benson and Dr. Cindy Lee for being my role models as successful women in science. Lastly, I'd like to thank Dr. Ronny Pini for his mentoring, collaboration, and support.

This research was funded by EPA STAR grant #834383, with experimental needs provided by Stanford University's Global Climate and Energy Project (GCEP).

Table of Contents

Page

List of Figures ix

List of Tables xi

CHAPTER ONE: INTRODUCTION TO CARBON CAPTURE AND STORAGE 1

Carbon Dioxide Trapping Mechanisms 2

Objectives 4

Works Cited 5

CHAPTER TWO: A COMPARISON STUDY OF SUPERCRITICAL CO_2 AND CO_2 SATURATED BRINE INJECTION STRATEGIES 7

Introduction 7

Methods 13

Numerical Simulation 13

Model Set up 18

Carbon Dioxide Injection 24

Model Assessment 25

Results 27

CO_2 Plume Behavior 27

Pressure Buildup 40

Discussion 43

Conclusions 46

Works Cited 48

CHAPTER THREE58 HYSTERETIC TRAPPING AND RELATIVE PERMEABILITY OF CO_2 IN SANDSTONE AT RESERVOIR CONDITIONS 58

Introduction 58

Theory 62

Materials and methods 66

Equipment 67

Rock and fluid properties 70

Porosity measurement 70

Absolute permeability measurement 71

Experimental procedure 72

Results 77

CO_2 saturations 77

Relative permeability measurements 81

Residual trapping 84

Discussion 86

Conclusions 92

Works Cited 95

CHAPTER FOUR: COST EFFECTIVE CO_2 STORAGE DESIGN TO ENHANCE SECONDARY GAS TRAPPING 102

Introduction 102

Co-injection Methods 104

Objectives 107

Methods 108

TOUGH2 model set-up 108

Cost analysis 113

Minimization Algorithm 127

Results 130

Discussion 139

Conclusions 143

Works Cited 145

CONCLUSION 152

APPENDICIES 155

List of Figures

Figures ***Page***

Figure 2. 1.Space discretization used in the IFDM. 14

Figure 2. 2.Conceptual model for CO_2 injection into a homogeneous formation showing the hydrostatic pressure gradient. 19

Figure 2. 3. Set up of stratified formation radial model..... 22

Figure 2. 4. Three dimensional model set up for flat and dipping formations 23

Figure 2. 5. Cross section of permeability modifiers..... 24

Figure 2. 6 a and b. Homogeneous formation CO_2 plumes at end of injection and end of monitoring period..... 29

Figure 2. 7 c and d. Homogeneous formation CO_2 plumes at end of injection and end of monitoring period..... 29

Figure 2. 8 a and b. Stratified formation CO_2 plumes at end of injection and end of monitoring period..... 31

Figure 2. 9 c and d. Stratified formation CO_2 plumes at end of injection and end of monitoring period..... 31

Figure 2. 10 a and b. $scCO_2$ injection into flat-lying heterogeneous formation 34

Figure 2. 11 c and d. Dissolved CO_2 injection into flat-lying heterogeneous formation..35

Figure 2. 12. a and b. $scCO_2$ injection into 5° dipping heterogeneous formation 38

Figure 2. 13 c and d. Dissolved CO_2 injection into 5° dipping heterogeneous formation 39

Figure 2. 14. Pressure buildup around the injection well. 40

Figure 2. 15. Pressure buildup in the homogeneous case 41

Figure 2. 16. Pressure buildup and material layers in the stratified case 42

Figure 2. 17. Lateral pressure buildup within the top layer of storage formation. 42

Figure 2. 18. Vertical pressure buildup 10 m from injection well. 43

Figure 2. 19. Class II injection wells in the USA. 46

Figure 3. 1. Horizontal core flooding experimental setup 68

Figure 3. 2. Slice-averaged porosity along the core..... 71

Figure 3. 3. Steady state measurements of pressure drop 72

Figure 3. 4. CO_2 injection scheme 73

Figure 3. 5. Average pressure drop at steady-state 75

Figure 3. 6. Slice-averaged CO_2 saturation profiles. 78

Figure 3. 7. CT scan of CO_2 distributions. 79

Figure 3. 8. CO_2 phase fractional flow versus saturation plot 80

Figure 3. 9. Core-average relative permeability measurements 82

Figure 3. 10. Hysteresis in CO_2 relative permeability measurements. 83

Figure 3. 11. Nonhysteretic water relative permeability measurements. 84

Figure 3. 12. Residual saturation 85

Figure 3. 13. Van Genuchten-Burdine models 87

Figure 3. 14. Residual saturation from Akbarabadi and Piri (2013). 90

Figure 3. 15. Van Genuchten-Burdine model fit to Akbarabadi and Piri (2013). 91

Figure 4. 1. Historical and predicted electricity prices. 116

Figure 4. 2. Five-spot injection patterns 120

Figure 4. 3. Levenberg-Marquardt minimization algorithm. 129

Figure 4. 4. Model initializatiom 111

Figure 4. 5. Water production model set up..... 113

Figure 4. 6. Supercritical CO_2 injection..... 132

Figure 4. 7. Dissolved CO_2 injection. 133

Figure 4. 8. WAG injection..... 134

Figure 4. 9. SWAG injection 135

Figure 4. 10. Direct co-injection 137

Figure 4. 11. Post- CO_2 injection water flush. 138

Figure 4. 12. Cost function of each injection strategy over time. 140

Figure 4. 13. Secondary trapping performance of each injection strategy over time. 141

List of Tables

Tables ***Page***

Table 2. 1. Hydrogeologic properties of the homogenous storage formation. 20

Table 2. 2. Hydrogeologic properties of the stratified storage formation..... 22

Table 3. 1. Commonly used nonwetting relative permeability parameters. 65

Table 3. 2. Average absolute permeabilities (k) for the same Berea core. 72

Table 3. 3. Fractional flows of CO_2 (ff_{CO_2}). 74

Table 3. 4. Results by fractional flow of CO_2 for pressure drop 76

Table 3. 5. Results by fractional flow of CO_2 for core average water saturation and relative permeability data 83

Table 3. 6. Unweighted best fit comparison between common hysteretic nonwetting relative permeability functions 89

Table 3. 7. Unweighted best fit comparison between common wetting relative permeability functions. 89

Table 4. 1 CO_2 injection schemes. 110

Table 4. 2. Hydrogeologic properties of the storage formation. 111

Table 4. 3. Monitoring Costs. 124

Table 4. 4. Monitoring costs of injection strategies 125

Table 4. 5 Cost of Pore space leasing per injection strategy. 125

Table 4. 6. Best estimates for water injection rates. 130

Table 4. 7. Minimized cost functions 130

Table 4. 8. Plume properties. 131

Table 4. 9. Water production design. 139

CHAPTER ONE:

INTRODUCTION TO CARBON CAPTURE AND STORAGE

In the recent decade carbon capture and storage (CCS) has emerged as a favorable technology for reducing anthropogenic greenhouse gas emissions while allowing the continued use of fossil fuel resources (IPCC, 2005; IEA, 2013). CCS technologies aim to safely sequester industrially produced CO_2 in deep geologic formations. CCS is performed in four basic steps. First, gaseous CO_2 is separated from smokestacks of large point source emitters. The captured CO_2 is then compressed to a near supercritical phase for transport. The CO_2 is transported via pipeline to a suitable geologic formation where it is injected as a supercritical fluid for long term storage. Potential geologic storage options include direct sequestration into depleted oil and gas reservoirs or deep saline formations, or secondary storage after being used for enhanced oil and gas recovery (EOR) or enhanced coal bed methane recovery (ECBM) (IPCC, 2005).

Carbon capture and storage is considered to be an integral part of mitigation scenarios where long-term global average temperature increases are limited to less than 4°C, particularly for the 2°C goals set by the Copenhagen Accord (UNFCCC, 2009; IEA, 2013). Under business as usual conditions, a cumulative mass of approximately 120 $GtCO_2$ would need to be captured and stored between 2015 and 2050 across all regions of the globe in order to achieve the 2°C target (IEA, 2013). This CO_2 reduction would account for 17% of the necessary emissions reductions by 2050 (IEA, 2012).

The Global CCS Institute recently reported on the worldwide status of CCS and current CCS project standings in terms of the stage they are at in the project lifecycle (GCCSI, 2013, 2014). The CCS project lifecycle consists of three planning stages (Identify, Evaluate, and Define), three active stages (Execute, Operate, and Closure), and the final Post-closure stage (GCCSI, 2013). As of February 2014, there are 21 large-scale projects in Execute (construction) or Operate stages, a 50% increase since 2011. These have the capacity to capture up to 40 $MtCO_2$ per year. The United States currently has 19 large scale injection projects (LSIPs) at various stages of the CCS project lifecycle, both planning and active. Additionally, the world's first two power sector projects with CCS will begin operation in North America in 2014. Elsewhere in the world, the Middle East has moved to the Execute stage for the world's first large-scale CCS project in the iron and steel sector and China has doubled the number of CCS projects since 2011 with 12 large-scale CCS projects in all stages, ranking second to the US (GCCSI, 2013, 2014).

Carbon Dioxide Trapping Mechanisms

Geologic carbon sequestration schemes rely on four major trapping mechanisms to ensure long term security: structural and stratigraphic, residual (or capillary), solubility, and mineral trapping (IPCC, 2005). Over time, the amount of CO_2 immobilized by each mechanism shifts and the storage security increases. The structural barrier, or seal, is the primary trapping mechanism containing the CO_2 plume. Ideally, the seal will have low permeability, high capillary entry pressure, and fully enclose the expected extent of the CO_2 plume. The remaining mechanisms are known as secondary trapping mechanisms.

Residual trapping becomes the dominant secondary form of CO_2 immobilization immediately following injection (IPCC, 2005). This mechanism occurs within the pore space due to capillary forces between the CO_2 and native brine. In a two-phase water-wet system, the aqueous wetting phase has an affinity to the rock grain and travels along the pore surface, while the CO_2 rich non-wetting phase travels between wetting phase interfaces. During CO_2 injection, water is drained from pores as CO_2 enters. Following injection, the aqueous phase re-enters pores at the trailing edge of the plume, breaking off bubbles of CO_2 and rendering them immobile. Over time trapped CO_2 bubbles will dissolve into formation water as carbonic acid.

Dissolution trapping occurs as a natural equilibration process of the CO_2 mixing with native brine on the scale of tens to hundreds of years post-injection (IPCC, 2005). Following Henry's Law at targeted injection depths (greater than 800 m), CO_2 can have solubility 50 times higher than at surface conditions, 50 g/L compared to 1 g/L (Falta et al., 2013). This property allows for efficient storage in the aqueous phase. Another advantageous property of CO_2 saturated brine is that it has a higher density than native brine and will tend to sink over time, increasing storage security (Zuo et al., 2012).

If appropriate mineralogy is present, dissolved CO_2 will eventually react (on the scale of hundreds to thousands of years) with reservoir minerals to form carbon-bearing ionic species (e.g. HCO_3^-, $CaHCO_3^+$, $MgHCO_3^+$, $NaHCO_3^0$) (IPCC, 2005; Czernichowski-Lauriol et al., 2006). This is sometimes called ionic trapping (IPCC, 2005). Further breakdown of these minerals could precipitate new carbonate minerals

(e.g. $CaCO_3$, $CaMg(CO_3)_2$, $MgCO_3$, $FeCO_3$, $NaAlCO_3(OH)_2$), securing injected CO_2 for thousands to millions of years (IPCC, 2005; Czernichowski-Lauriol et al., 2006).

The storage security is a qualitative measure that increases as CO_2 progresses from a mobile free phase gas to residual gas to a dissolved solution to carbonate minerals (IPCC, 2005). For example, residually trapped CO_2 has the potential for remobilization in the case of secondary CO_2 injection or cyclic drainage processes; therefore, CO_2 in the aqueous phase is considered to be stored more securely than residually trapped CO_2 gas. When mobile and trapped CO_2 (or CO_2 trapped by secondary methods) in a system are discussed in terms of storage security it is important to consider which trapping mechanism(s) are being referred to.

Objectives

The goal of this dissertation was to further the understanding of the effects of secondary trapping mechanisms on CO_2 storage systems to improve storage design and security. The first study compares the storage performance of supercritical CO_2 and dissolved CO_2 injection strategies based on plume distribution and pressure effects using numerical simulations. The second study reports experimental results from an investigation into hysteretic trapping and relative permeability of supercritical CO_2 at reservoir conditions. The third study uses inverse modeling techniques to optimize water/CO_2 co-injection schemes based on cost and secondary trapping. Ultimately, results may be used to enhance storage security by designing CO_2 injection strategies that take advantage of CO_2 trapping behavior at targeted depths.

Works Cited

Czernichowski-Lauriol, I., Rochelle, C.A., Gaus, I., Azaroual, M., Pearce, J., Durst, P., 2006. Geochemical interactions between CO_2, pore-waters and reservoir rocks (pp. 157-174). Springer Netherlands.

Falta, R., Zuo, L., Benson, S., 2013. Migration of exsolved CO_2 following depressurization of saturated brines. Greenhouse Gases: Science and Technology, 3(6), 503-515.

Global CCS Institute (GCCSI), 2013.The Global Status of CCS: 2013.

Global CCS Institute (GCCSI), 2014. The Global Status of CCS: February 2014.

International Energy Agency (IEA), 2012. Technology Perspectives 2012. IEA, Paris, France.

International Energy Agency (IEA), 2013. Technology Roadmap: Carbon capture and storage. IEA, Paris, France.

Intergovernmental Panel on Clim. Change (IPCC), 2005. Underground geologic storage: IPCC special report on carbon dioxide capture and storage, Chap. 5. Cambridge University Press, New York.

U.N. Framework Convention on Climate Change (UNFCCC), 2009. Copenhagen Accord. Report, Conference of the Parties, Fifteenth Session. United Nations. Copenhagen, Denmark. December 7-18, 2009.

Zuo, L., Krevor, S., Falta, R., Benson, S., 2012. An experimental study of CO_2 exolution and relative permeability measurements during CO_2 saturated water depressurization. Transort in Porous Media, 91(2), 459-478.

CHAPTER TWO:

A COMPARISON STUDY OF SUPERCRITICAL CO_2 AND CO_2 SATURATED BRINE INJECTION STRATEGIES

Introduction

The standard injection strategy for geologic storage of CO_2 (GCS) is in the supercritical phase ($scCO_2$). This method optimizes the mass of CO_2 injected by volume and relies predominantly on structural and capillary CO_2 trapping mechanisms to immobilize the majority of CO_2 in the tens of years post-injection (IPCC, 2005; IEA, 2013). Under $scCO_2$ injection schemes, multi-phase flow occurs with the migration of the $scCO_2$ plume being dependent on the in situ fluid and formation properties. At targeted reservoir conditions in deep saline formations there is a density difference near 300 kg/m^3 between resident brine and free phase CO_2. This density difference drives a buoyant migration of $scCO_2$ upward toward the structural trap, or seal (Bachu, 2002; IPCC, 2005; Eke et. al., 2009). Ideally, the seal will have low permeability, high capillary entry pressure, and fully enclose the expected extent of the $scCO_2$ plume. These properties will act as a barrier to flow and cause the $scCO_2$ to migrate laterally. In addition to density differences, the viscosity of $scCO_2$ can be less than the viscosity of the aqueous phase by a factor of 15 at storage conditions (Lemmon et al., 2011).

A thorough description of the expected plume distribution and behavior is necessary to evaluate the potential storage performance of a GCS project. Plume behavior can be quantified using the mobility ratio, the storage efficiency, the maximum areal

extent, and the Darcy velocity of the plume. The mobility ratio describes if the plume front will be stable. A simplification of the mobility ratio often used for sharp interface models is given by

$$M = \frac{\lambda_{CO2}}{\lambda_w} \tag{2.1}$$

$$\lambda_\beta = \frac{k^*_{r\beta}}{\mu_\beta} \tag{2.2}$$

Where M is the mobility of the injected CO_2 to the mobility of the formation brine, λ_β is the mobility of fluid β, $k^*_{r\beta}$ is the endpoint relative permeability of fluid β, and μ_β is the viscosity of fluid β (Lake, 1989; Van der Meer, 1992; Juanes et al., 2010). The mobility of CO_2 is taken within the plume region and the mobility of the formation brine is taken ahead of the displacement front, outside of the plume region (Juanes et al., 2010). Ratios less than one indicate hydrodynamic stability and larger than one indicate hydrodynamic instability. The mobility ratio of $scCO_2$ to brine is typically predicted to be about 10 during the injection period, with values varying between 5 and 40 depending on pressure and temperature conditions (Hesse et al., 2008; MacMinn and Juanes, 2009; Juanes et al., 2010).

If the plume front is unstable, it is likely to bypass pore-space in the form of viscous fingers or a gravity tongue below the sealing layer (Lake, 1989; Garcia, 2003; Garcia and Pruess, 2003; Qi et al., 2009). Viscous fingers take on the shape of waves or rounded lobes of $scCO_2$ saturation at the plume front (Homsy, 1987; Hagoort, 1988; Garcia, 2009). Gravity tongues are caused when the $scCO_2$ overruns the resident brine

due to the lower density and viscosity of the $scCO_2$ (Hagoort, 1988). The combined effect, also known as "gravity override", is the formation of a single viscous finger traveling along the top of the aquifer (Hagoort 1988). In addition to hydrodynamic instabilities, heterogeneities within the storage formation have been shown to lead to preferential flow paths also resulting in pore-space bypassing (Doughty and Pruess, 2004).

Mechanisms that promote pore-space bypassing reduce the storage efficiency of the injected CO_2 and increase the areal extent of the plume within the storage formation (Qi et al., 2009). The storage efficiency, E_S, represents the fraction of accessible pore volume occupied by free-phase CO_2 (Lake, 1989; Van der Meer, 1995; IEA, 2013).

$$E_S = \frac{Volume\ of\ injected\ CO_2}{Maximum\ storage\ volume} \tag{2.3}$$

where the volume of injected CO_2 is under reservoir conditions and the maximum storage volume is the total pore space of the assessed area that can be accessed by CO_2 (Van Der Meer, 1995; Gorecki et al., 2009). The storage efficiency is similar to the volumetric sweep efficiency, or the volume of rock contacted by a displacing agent, originally developed as a performance measure of enhanced oil recovery operations (Lake, 1989). It is also called the storage efficiency factor, the storage coefficient, and the capacity coefficient (Bachu et al., 2007; DOE 2007, 2008; Gorecki et al., 2009).

Targeted CO_2 storage formations can be open or closed systems (Gorlecki et al., 2009). In a closed system, the storage formation may be highly faulted and compartmentalized, allowing for very little fluid flow or pressure relief at the boundaries

(Gorecki et al., 2009). In an open system, the storage formation is relatively unfaulted with consistent hydrogeologic properties over regional scales, making it difficult to determine a precise value to use for the maximum storage volume in equation 2.3 (Gorecki et al., 2009; IEA, 2013). The two most common methods to determine storage efficiency are from the Department of Energy (DOE) and the Carbon Sequestration Leadership Forum (CSLF) (Bachu, 2008; DOE 2007, 2008, Gorlecki et al., 2007). By the DOE method, the maximum storage volume is calculated by equation 2.4 and by the CSLF method, the maximum storage volume is calculated by equation 2.5.

$$V_{\text{smax}} = A \times h \times \varphi \tag{2.4}$$

$$V_{\text{smax}} = A \times h \times \varphi \times (1 - S_{\text{wirr}}) \tag{2.5}$$

where A is the geographic area that defines a basin or region being assessed for CO_2 storage, h is gross thickness of the CO_2 storage formation assessed within the basin or region defined by A, ϕ is average porosity of the entire formation over gross thickness h, and S_{wirr} is the irreducible water saturation, or the maximum residual water saturation (S_{wr}), under injection conditions (Bachu, 2008; DOE 2007, 2008; Gorecki et al., 2009).

The CO_2 plume is expected to migrate for several decades after injection is completed increasing the areal extent and decreasing the storage efficiency (Bachu et al., 2007; IEA, 2013). This leads to uncertainty over what representative storage efficiency factor should be used in assessment methodologies due to the dependence on the time at which A is evaluated (Bachu et al., 2007; IEA, 2013). In addition to temporal considerations, E_S is dependent on the injection pattern, pressure management methods,

reservoir thickness, relative permeability, residual saturations, areal and vertical formation heterogeneities, mobility ratio, density differences between fluids, and flow rate (IEA, 2013). Current analytical techniques and numerical simulation methods predict that 0.6-6% of the available pore volume will contain CO_2 if it is injected in a supercritical phase (Van der Meer, 1995; Bachu et al., 2007; DOE NETL, 2007, 2008; Gorecki et al., 2009; Fang et. al. 2010; Juanes et al., 2010; Okwen et al., 2010; Szulczewski et al., 2010; IEA, 2013).

The areal extent of the CO_2 plume is also directly related to the storage security, or risk of leakage. Leakage pathways include diffusion through the caprock, flow through unidentified geologic features, like faults or fractures; or flow through man-made conduits, like abandoned boreholes (Celia and Nordbotten, 2009). The risk of leakage via any of these pathways is site specific but generally increases with the areal plume extent on the caprock.

Alternative injection methods seek to improve GCS storage performance by enhancing CO_2 trapping mechanisms. Stacked injection methods take advantage of heterogeneities in the formation stratigraphy (Ambrose et al., 2006). In this case, injection occurs into a series of vertical aquifers separated by low permeability barriers. Proposed injection methods to increase capillary trapping use some form of water or brine/CO_2 co-injection, where the co-injection fluid is retrieved from the storage formation or overlying formations (Kumar et al, 2004; Keith et al., 2005; Leonenko et al, 2006; Juanes et al., 2006; Ide et al., 2007; Leonenko and Keith, 2008; Michael et al.,

2011). Co-injection schemes also enhance the dissolution of CO_2 through mixing and may improve the vertical sweep of the plume by reducing the mobility ratio between phases (Qi et al., 2009). Additionally, brine supply wells may be used to mitigate pressure elevations during injection and regulate the direction of plume flow and displacement of native brine (Leonenko and Keith, 2008; Jain and Bryant, 2011; Tao and Bryant, 2012). Another suggested method takes advantage of CO_2 solubility by fully dissolving CO_2 in formation brine ex-situ and injecting the mixture as a single phase saturated brine (Lake 1989; Burton and Bryant, 2007; Leonenko et al., 2006; Eke et. al. 2009; Fang et. al. 2010; Jain and Bryant, 2011).

Surface dissolution of the CO_2 in brine changes the mechanics of flow in the subsurface upon injection. Single phase flow occurs, eliminating complications associated with unfavorable mobility ratios, viscous fingering, and reduced phase permeabilities (Burton and Bryant, 2007). This single phase flow is expected to lead to a more uniform vertical sweep of the reservoir (Eke et. al. 2009, Fang et. al. 2010). Over time, the solution will tend to sink as a result of density differences with the native brine, removing the need for a perfect seal and allowing safe injection at shallower depths (Fang et. al. 2010). This method is estimated to require 3-9% additional power consumption and increase capital costs by 60%; however, there is expected to be a reduction in monitoring costs over $scCO_2$ injection (Burton and Bryant, 2009; IEAGHG, 2010).

The objective of this study was to determine the advantages and disadvantages of $scCO_2$ and dissolved CO_2 injection strategies on storage performance based on

distribution and immobilization of injected CO_2 and pressure buildup within the storage formation. Simulation cases increased in formation heterogeneity, becoming more realistic with each case. Initial simulations considered a homogeneous aquifer system, followed by simulations in a stacked, stratified aquifer system. Final simulations were in aquifer systems heterogeneous in all directions, both flat lying and dipping at 5 degrees.

Methods

Numerical Simulation

Regional scale multiphase flow models were run using Lawrence Berkeley National Laboratory's TOUGH2-ECO2N to simulate both supercritical and dissolved CO_2 injection into deep saline aquifers (Pruess, 2005). TOUGH2 is a numerical simulator for nonisothermal flows of multicomponent, multiphase fluids in one, two, and three-dimensional porous and fractured media (Pruess et al., 1999). All cases were run isothermally, solving governing flow equations only for mass transport of CO_2, water, and salt. TOUGH2 solves flow equations using the integral finite difference method (IFDM) for spatial discretization and a first-order backward finite difference method (FDM) for fully implicit time discretization (Edwards, 1972; Narasimhan and Witherspoon, 1976; Pruess et al., 1999). The mass balance equation and corresponding discretized form are given as

$$\frac{d}{dt}\int_{V_n} M^K dV_n = \int_{\Gamma_n} \mathbf{F}^K \bullet \mathbf{n} d\Gamma_n + \int_{V_n} q^K dV_n \tag{2.6}$$

$$\frac{dM_n^{\ K}}{dt} = \frac{1}{V_n}\sum_m A_{nm}F_{nm}^{\ K} + q_n^{\ K} \tag{2.7}$$

where, in equation 2.6, integration is over an arbitrary subdomain V_n, bounded by the closed surface Γ_n. M is mass per volume, K= 1, ..., NK labels the mass components (water, CO_2, NaCl), **F** is mass flux, q is the source/sink term, and **n** is a normal vector on surface element $d\Gamma_n$ pointing inward into V_n . The discretized version (equation 2.7) takes M_n (kg) as the volume average value of M over V_n (m^3), F_{nm} is the average value of the inward (normal) component of **F** over the surface A_{nm} between elements V_n and V_m (Figure 2.1) (Pruess, 1999).

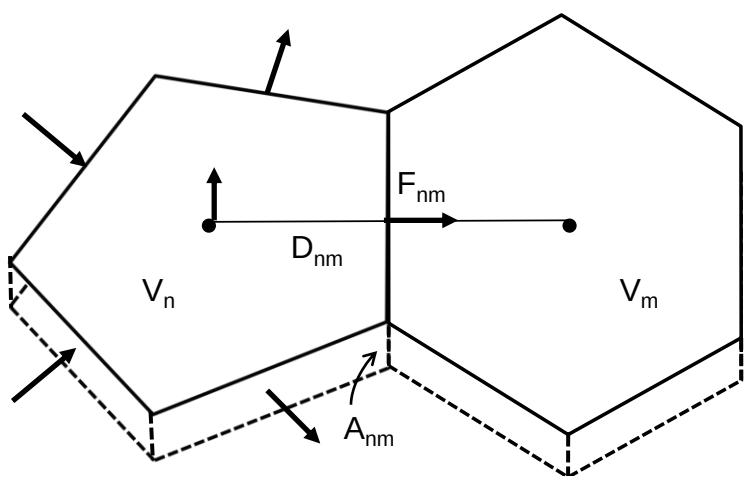

Figure 2. 1.Space discretization used in the IFDM.

Fluid advection is described by a discretized form of the multiphase extension of Darcy's Law where individual phase fluxes are given by

$$F_{\beta,nm} = -k_{nm}\left[\frac{k_{r\beta}\rho_{\beta}}{\mu_{\beta}}\right]_{nm}\left[\frac{P_{\beta,n} - P_{\beta,m}}{D_{nm}} - \rho_{\beta,nm}g_{nm}\right] \tag{2.8}$$

Subscript *nm* represents an averaging over the interface between volume elements V_n and V_m, and β represents the phase, *k* is absolute permeability (m^2), $P_{\beta,n}$ and $P_{\beta,m}$ are the phase fluid pressures (Pa) in each element, D_{nm} is the distance between the centers of elements (m), ρ_β is the phase density (kg/m^3), and g is gravitational acceleration (m/s^2) (Figure 2.1) (Pruess et al., 1999). During single phase flow of solute transport with upstream weighting as the interface averaging scheme, the numerical dispersivity of the advection term is equal to one-half the grid spacing in the direction of flow (Roache, 1972; Oldenburg et al., 2013). Previous work has shown that the gas phase in two phase flow is considered to have a self-sharpening front due to relative permeability effects and is expected to exhibit minimal effects of numerical dispersion (Doughty and Freifeld, 2013).

The IFDM does not reference a global coordinate system but requires the element volume, interfacial area between connecting elements, nodal distances between elements, and components of gravitational acceleration along nodal lines as input (Pruess, 1999). This allows for arbitrary irregular spatial discretization, such as polygonal (Voronoi) grids. Voronoi grids have been shown to reduce numerical dispersion produced by Cartesian grids due to the grid orientation effect, while allowing grid refinements strictly around areas of interest (Aziz 1993, Yamamoto and Doughty, 2011). Simulation meshes

were designed to take advantage of these properties using both regular, radial grids and three-dimensional Voronoi grids in models.

ECO2N is a TOUGH2 module that includes a comprehensive description of the thermodynamics and thermophysical properties of H_2O-NaCl-CO_2 mixtures, which reproduces fluid properties for the temperature, pressure, and salinity at conditions of interest for geologic storage (10 ˚C ≤ T ≤ 110 ˚C, P ≤ 60 MPa, salinity up to full halite saturation) (Pruess, 2005). A full description of the module can be found in Pruess (2005). In summary, TOUGH2-ECO2N represents up to three phases: liquid, gas, and solid (precipitated salt). The only chemical reactions modeled by ECO2N are equilibrium phase partitioning of water and carbon dioxide between the aqueous and gaseous phases, and precipitation and dissolution of solid salt. The partitioning of H_2O and CO_2 between liquid and gas phases is modeled as a function of temperature, pressure, and salinity by the correlations of Spycher and Pruess (2005). Dissolution and precipitation of salt is treated by means of local equilibrium solubility (Pruess, 2005).

Secondary equations were modified to include a simple linear nonwetting phase trapping model in both capillary pressure and relative permeability calculations. These modifications are discussed in detail by Patterson (2011) and Patterson and Falta (2012). The linear trapping model is given by

$$S_{nr} = f_r S_{ni} \tag{2.9}$$

where S_{nr} is the trapped nonwetting phase saturation, S_{ni} is turning point saturation (maximum nonwetting saturation achieved prior to imbibition), and f_r is the fraction of S_{ni} trapped. The turning point saturation was adjusted to account for CO_2 dissolution over time.

The nonwetting residual trapped saturation was then used to calculate the effective wetting phase saturation (equation 2.10) for use in nonwetting phase capillary curves and relative permeability functions (Luckner et al., 1989).

$$\hat{S} = \frac{S_w - S_{wr}}{1 - S_{wr} - S_{nr}} \tag{2.10}$$

where $\hat{S}$ is the effective saturation, S_w is the wetting phase saturation, and S_{wr} is the wetting phase residual saturation. In this case, the effective saturation takes into account nonwetting phase entrapment. By this method, if the local history of saturation is known for the nonwetting phase, the effective saturation is continuously updated as CO_2 saturations increase and decrease during injection and migration.

The effective saturation was used to calculate the hysteretic Van Genuchten and Van Genuchten- Mualem models of capillary pressure and relative permeability (equations 2.11 and 2.12) (Mualem, 1976; Van Genuchten, 1980; Luckner et al., 1987).

$$P_c = -P_0 \left(\hat{S}^{-1/m} - 1 \right)^{1-m} \tag{2.11}$$

$$k_{rCO_2} = \sqrt{1 - \hat{S}} \left(1 - \hat{S}^{1/m} \right)^{2m} \tag{2.12}$$

where P_c is the capillary pressure, P_0 is the entry pressure, k_{rCO_2} is the CO_2 relative permeability, and m is a scaling factor describing the grain size and porosity distribution. By this method, characteristic functions are continuously differentiable as $\hat{S}$ is continuously updated. The nonhysteretic Van Genuchten-Mualem model was chosen to represent relative permeability of the liquid phase (equations 2.13 and 2.14) (Mualem, 1976; Van Genuchten, 1980).

$$k_{rw} = \sqrt{\bar{S}_w}\left[1-(1-\bar{S}_w^{\,1/m})^m\right]^2 \tag{2.13}$$

$$\bar{S}_w = \frac{S_w - S_{wr}}{1-S_{wr}} \tag{2.14}$$

where $\bar{S}_w$ is the effective wetting phase saturation for use in wetting phase capillary curves and relative permeability functions (Luckner et al., 1989).

Model Set up

Homogeneous Formation Case

The first set of models was used to develop a preliminary understanding of injected $scCO_2$ and injected dissolved CO_2 behavior. Simulated injection was into a 200 m thick, anisotropic, homogeneous storage formation represented using a radial grid refined around the injection well and extending out 200 km. The grid was refined such that the well was approximately 0.16 m^2 (18 inch diameter). The CO_2 injection well was screened over the entire thickness of the storage formation. These patterns were chosen to produce an opportunity for maximum contact with pore space during $scCO_2$ injection while minimizing well bore pressure during dissolved CO_2 injection.

The storage formation was bounded above and below by a no flow boundary condition and at formation edge by a fixed state boundary condition. Relevant hydrogeologic properties were characteristic of the deep saline aquifers under consideration for GCS. A hydrostatic pressure and geothermal temperature gradient was established between the bottom of the storage formation at 20 MPa and 50ºC and the top at 18 MPa and 46.1ºC. The formation was uniformly given a salinity of 50,000 mg/L with full property dependence on salinity allowing for possible salt precipitation and aqueous density changes. Values of the storage formation and saturation curve parameters are given in Table 1. Parameters were adapted from Birkholzer et al. (2009), Barnes et al. (2009), and Zhou et al. (2010).

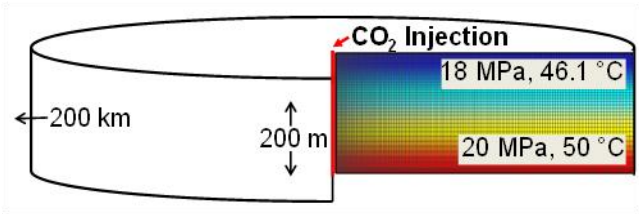

Figure 2. 2.Conceptual model for CO_2 injection into a homogeneous formation showing the hydrostatic pressure gradient.

Table 2. 1. Hydrogeologic properties of the homogenous storage formation.

Porosity	φ	0.24
Horizontal permeability	$\mathbf{k_r}$	100 mD
Vertical permeability	$\mathbf{k_z}$	10 mD
Pore compressibility	β_p	3.71×10^{-10} Pa^{-1}
Van Genuchten parameter	**m**	0.41
Residual brine saturation	$\mathbf{S_{lr}}$	0.30
Residually trapped fraction of S_{CO2} max.	$\mathbf{f_{snr}}$	0.50
Capillary entry pressure	α^{-1}	4×10^3 Pa

Stratified Formation Case

The second set of regional models depicts a stratified formation. Carbon dioxide injection into a geology characterized by alternating, laterally extensive layers of higher and lower permeability is anticipated to increase storage efficiency. In order to simulate this type of geology, material types were based on those of the Illinois Basin. The Illinois Basin is one of the most important target aquifers systems for geologic storage of carbon dioxide in the United States (Birkholzer and Zhou, 2009). A 2 km thick, 200 km radial model was developed, refined about the injection well. The injection well was screened over the entire thickness of the storage formation (Figure 2.3).

At the base of the model was a storage formation based on the Mt. Simon sandstone that contained five layers of aquifer material that alternated horizontal permeability by two orders of magnitude and vertical permeability by one order of

magnitude, the capillary entry pressure was kept the same (Table 2.2). The three higher permeability layers were 66, 66, and 67 meters thick and the two lower permeability layers were 6 meters thick. The lower permeability layers acted as stratigraphic traps for the injected CO_2. The storage formation was capped by a material layer with a lower capillary entry pressure, permeability, and porosity representing the Eau Claire formation. This was the primary seal and structural trapping mechanism for the injected CO_2. Eight material layers extended to near surface conditions above the Eau Claire. Hydrogeologic properties were assigned based on characteristic aquifer properties of the Ordovician, Silurian-Devonian, Mississippian, Pennsylvanian, and Quaternary systems (Visocky et al., 1985; Mast and Howard, 1990; Lloyd and Lyke, 1995; Kiraly, 2002). A secondary seal and tertiary seal are included above the Ordovician and Devonian aquifers. These eight layers were included to observe the hydraulic head changes near surface. Pressure and temperature gradients were established from the bottom of the storage formation at 20 MPa and 50ºC to near surface conditions at 13500 Pa and 30ºC. All formations were uniformly given a salinity of 50,000 mg/L. Characteristic curves were given the same parameters as the previous case (Table 2.1); all other hydrogeologic properties are found in Table 2.2.

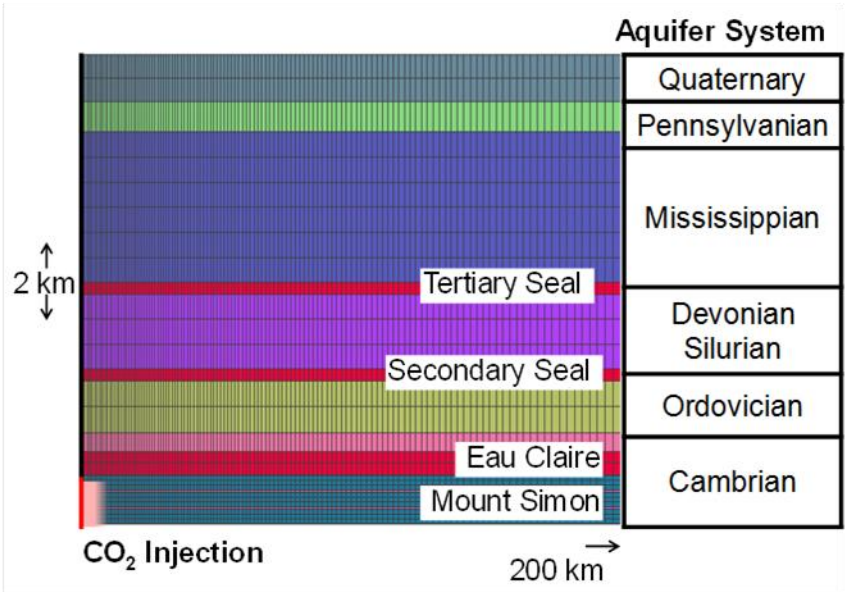

Figure 2. 3. Set up of stratified formation radial model.

Table 2. 2. Hydrogeologic properties of the stratified storage formation.

Aquifer System		Porosity, Φ [-]	Horizontal Permeability, k_r	Vertical Permeability, k_z	Pore Compressibility, β_p
Cambrian	Mt. Simon I	0.24	100 mD	10 mD	3.71×10^{-10} Pa^{-1}
	Mt. Simon II	0.24	1 mD	1 mD	3.71×10^{-10} Pa^{-1}
	Eau Claire	0.15	0.01 mD	0.001 mD	7.421×10^{-10} Pa^{-1}
	Ironton-Galesville	0.18	100 mD	10 mD	3.71×10^{-10} Pa^{-1}
Ordovician		0.18	100 mD	10 mD	3.71×10^{-10} Pa^{-1}
Devonian-Silurian		0.13	10 mD	1 mD	3.71×10^{-10} Pa^{-1}
Mississippian		0.15	100 mD	10 mD	3.71×10^{-10} Pa^{-1}
Pennsylvanian		0.18	100 mD	10 mD	3.71×10^{-10} Pa^{-1}
Quaternary		0.30	10 D	1 D	1.0×10^{-10} Pa^{-1}
Seals		0.15	0.01 mD	0.001 mD	7.421×10^{-10} Pa^{-1}

Heterogeneous Formation Cases

Two heterogeneous plume scale models were constructed using a 31.3 km^2 by 1 km thick three dimensional Voronoi grid refined about the well. One model was horizontal, and the other was dipping at 5 degrees to further mimic the geology of the Illinois basin. As in the stratified case, a 200 m storage formation was bounded by a no flow boundary on the bottom and several hydrogeologic material layers above. Outer boundaries were fixed state. The storage formation was capped by the Eau Claire material followed by Ordovician, Silurian-Devonian, and Mississippian aquifer materials with secondary and tertiary seals above the Ordovician and Devonian aquifers. At a five degree dip, material layers extended to near surface conditions (Figure 2.4). The storage formation was initialized as the Mt. Simon I material from Table 2.2. Pressure and temperature gradients were established so injection occurred at 20 MPa and 50ºC. All formations were uniformly given a salinity of 50,000 mg/L.

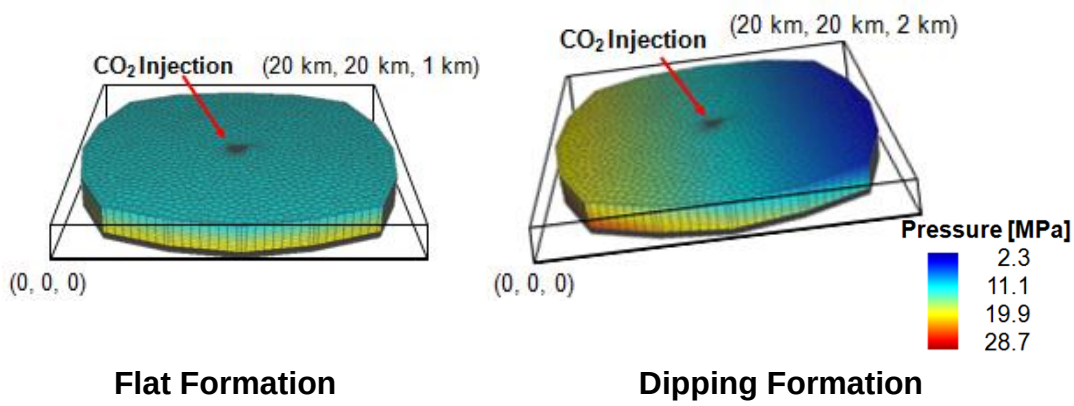

Figure 2. 4. Three dimensional model set up for flat and dipping formations. Polygonal gridding was refined around the injection well. Hydrostatic pressure distribution is shown to highlight differences. Vertical exaggeration 2x.

LBNL's iTOUGH2-GSLIB was used to generate heterogeneous, random, spatially correlated permeability fields using Sequential Gaussian simulation (SGSIM) (Finsterle, 1999). Using parameters similar to Barnes et al. (2009), the intrinsic permeability was given a log-normal distribution with a variance of 2.0 about the average permeability. SGSIM was used to create a spherical variogram model of log permeability with a vertical range of 1 m. A long horizontal to vertical ratio of 10,000 to 1 was assumed for the variogram length (Barnes et al., 2009). This model was mapped to the existing homogeneous storage formation to modify the existing permeability field (Figure 2.5). The capillary pressure was not varied by this method.

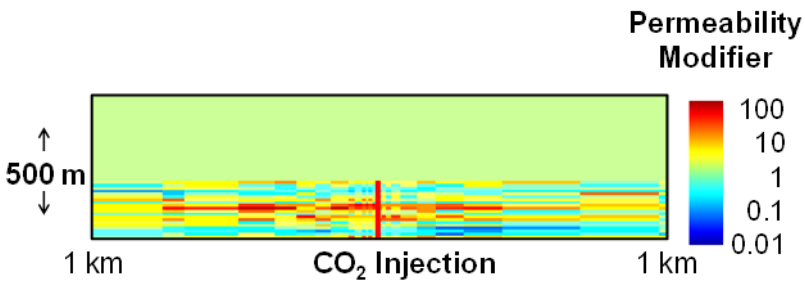

Figure 2. 5. Cross section of permeability modifiers. Mapped to the grid 1km about the CO_2 injection point. The color-flood shows the logarithmic distribution of modifiers where yellow is near 1.0.

Carbon Dioxide Injection

In each model, injection was performed at a rate of 5 kg/s CO_2 for 20 years, resulting in 3.16 Mt total. Injection rates were selected so as not to exceed the fracture pressure of the formations, set at approximately 1.5 times the hydrostatic pressure. For perspective, a typical 500 MW coal burning power plant generates about 3 $MtCO_2$ per

year and would likely require several injection wells for complete storage (Orr, 2009). The same mass of CO_2 was injected in each case; therefore, a much greater total mass (brine plus CO_2) was injected for the CO_2 saturated brine cases. A 21 to 1 brine to CO_2 ratio was needed to fully dissolve CO_2 at these temperatures, pressures, and salinity levels.

Model Assessment

Storage performance comparisons of the injection scenarios were made immediately following the end of injection at 20 years and 80 years post-injection at 100 years. The comparisons included the areal extent of the CO_2 plumes, the storage efficiencies, the mobility ratios, the maximum plume velocities, and the pressure buildup resulting from CO_2 injection. The $scCO_2$ plume was used for assessment of $scCO_2$ injection scenarios and the dissolved CO_2 plume was used for dissolved CO_2 injection scenarios. The pressure buildup was only compared for regionally extensive cases as the homogeneous and stratified cases provide upper and lower predictions of pressure buildup. Additionally, the $scCO_2$ mass dissolved into formation brine was recorded at the end of injection and the end of the monitoring period to observe trapping performance in the different model set-ups for $scCO_2$ injection.

The areal extent was used to calculate the storage efficiency and as a measure of the risk of leakage. The areal extent was determined in two ways. For radial grids, the maximum lateral distance of the CO_2 plume from injection well was used in a simple πr^2 calculation of plume area. For three-dimensional grids, the areal sum of elements

containing CO_2 was taken from the grid layer containing the largest CO_2 plume. In the dissolved case, an aqueous CO_2 mass fraction of 0.001 was used to determine the plume boundary. The areal extent was used as *A* (equation 2.4) to calculate the maximum storage volume for use in storage efficiency calculations (equation 2.3). The storage efficiency calculations assumed the CO_2 volume injected to be the equivalent total volume of $scCO_2$ injected at reservoir pressures and temperatures; this corresponds to the volume of CO_2 pre-dissolution for the dissolved case and does not include the injected volume of brine.

The mobility ratio of the $scCO_2$/brine system is provided as an indicator of plume stability. It was calculated by equation 2.1 using the endpoint relative permeabilities reached and the average fluid viscosities at those points (Juanes et al., 2010). For sharp-interface models, this approach assumes uniform gas saturations and aqueous concentrations within the plume, immiscibility of phases, and homogeneous, isotropic, isothermal conditions (Juanes et al., 2010). For these numerical simulations, this simplified mobility ratio should be considered to be the maximum mobility ratio of the system and *not* a representative value for the entire plume. Similarly, the maximum Darcy velocity of the plume is given to compare the lateral flow of supercritical and dissolved plumes to each other; it is *not* an average plume velocity.

Results

CO_2 Plume Behavior

Homogeneous Formation Case

Homogeneous formation simulations calculated the $scCO_2$ plume traveled 875 m from the well along the caprock during the injection period resulting in an areal extent of 2.41 km^2 and storage efficiency of 3.5% (Figure 2.6a). The plume was unstable, with a maximum mobility ratio of CO_2 to brine of 9. The maximum Darcy velocity was 10 cm/day along the caprock. To put this in perspective, native formation brine in targeted GCS storage formations are likely to have Darcy velocities between 1 and 10 cm/year (Szulczewski et al., 2012). This is equivalent to natural Darcy velocities of ~0.03 to 0.3 mm/day.

The dissolved plume had near uniform sweep of the aquifer by the end of injection, radially spreading 800 m along the bottom of the aquifer and 770 m along the caprock. This resulted in a maximum areal extent of 1.99 km^2 and storage efficiency of 4.2% (Figure 2.6b). Despite the greater injected mass, the plume size was reduced by 17%. The maximum Darcy velocity was 6 cm/day along the bottom of the storage formation. This velocity was almost half of the supercritical injection case. The mobility ratio for dissolved CO_2 injection scenarios was approximately one in this and all cases due to single-phase flow conditions with small differences in viscosity (~2×10^{-6} Pa·s) between saturated and unsaturated brines.

At 80 years post-injection, the $scCO_2$ plume had migrated 300 m farther from the injection well, resulting in an extent of 4.3 km^2, reducing the storage efficiency to 1.9% (Figure 2.7c). The maximum mobility ratio of $scCO_2$ to brine remained at 9 as gas accumulated at the top of the storage formation, maintaining high saturations. The maximum velocity reduced by two orders of magnitude during the monitoring period to 3 mm/day along the caprock. Of the 3.16 Mt $scCO_2$ injected, 0.6 Mt dissolved into the aqueous phase during the injection period, and an additional 0.15 Mt dissolved into formation brine during the monitoring period, trapping nearly 24% in the dissolved phase.

The monitoring period for dissolved CO_2 injection showed less significant plume migration during the 80 years post-injection (Figure 2.7d). Downward buoyancy flow within the plume led to a maximum areal extent of 2.09 km^2, half the extent of the $scCO_2$ at the same time. Accordingly, the storage efficiency was twice that of the $scCO_2$ at 4.0%. The maximum Darcy velocity of the CO_2 saturated brine reduced to only 0.74 mm/day, a quarter of the $scCO_2$ plume velocity at the same time.

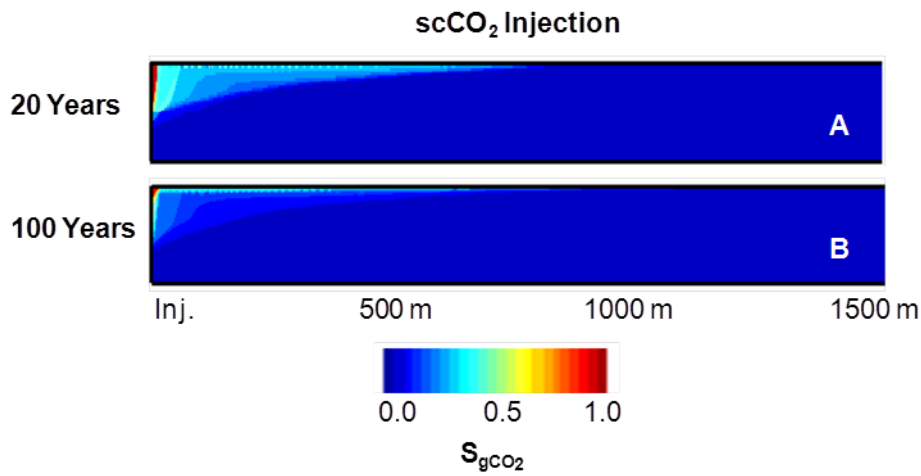

Figure 2. 6 a and b. Homogeneous formation CO_2 plumes at end of injection and end of monitoring period (Vertical exaggeration 2x).

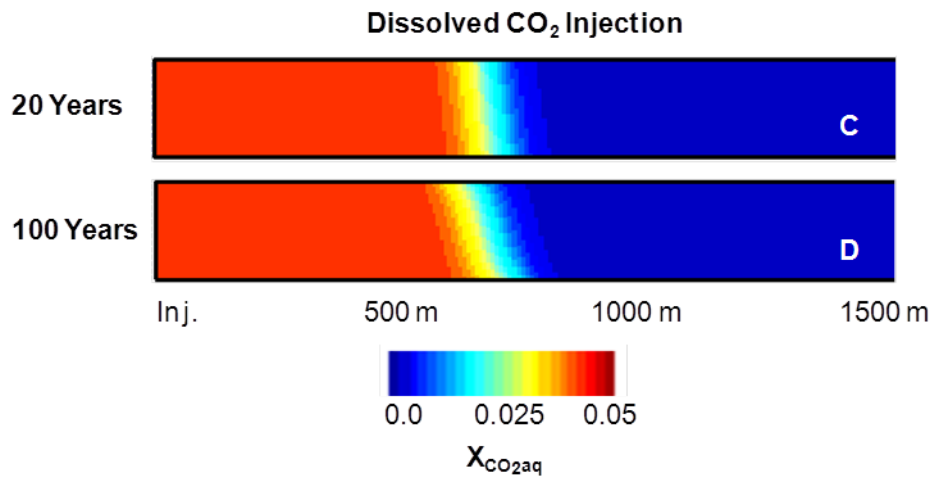

Figure 2. 7 c and d. Homogeneous formation CO_2 plumes at end of injection and end of monitoring period (V.E. 2x).

Stratified Formation Case

The extent of the $scCO_2$ plume was reduced in the stratified case as the plume separated into the three high permeability layers. The plume spread 860 m from the well during the injection period with areal extent of 2.23 km^2 and storage efficiency of 3.6%

(Figure 2.8a). The mobility ratio indicated unstable flow at 10**.** By the end of injection, the maximum Darcy velocity was 10 cm/day.

In contrast, the extent of the dissolved plume was increased in the stratified case due to higher pressure within the storage formation (discussed in the next results sub-section "Pressure Buildup"). The plume traveled 2.05 km^2 along the bottom of the aquifer during the injection period with storage efficiency of 4.2% (Figure 2.8b). The maximum velocity was 7 cm/day, higher than the homogeneous dissolved injection case.

The $scCO_2$ plume remained highly mobile during the 80 years following injection, reaching 300 m further from the injection well with an areal extent of 4.19 km^2 and a storage efficiency of 2.0% (Figure 2.9c). The mobility ratio of CO_2 to brine remained at 10. The maximum velocity reduced to 5 mm/day from 10 cm/day. While the plume extents were similar to the homogeneous case, $scCO_2$ dissolution was more effective in this case due to a larger plume surface area contacting the formation brine. 0.66 Mt CO_2 dissolved during injection and an additional 0.3 Mt dissolved into formation brine during the monitoring period, resulting in 31% of the CO_2 trapped in the dissolved phase.

The monitoring period showed the dissolved plume slightly sank, reaching maximum areal extent at 2.06 km^2 along the bottom of the storage formation with a storage efficiency of 4.1%, twice that of the $scCO_2$ at the same time (Figure 2.10d). The extent on the caprock remained unchanged at 1.91 km^2. The dissolved velocity was 0.71 mm/day as the plume slumped outward along the bottom of the storage formation.

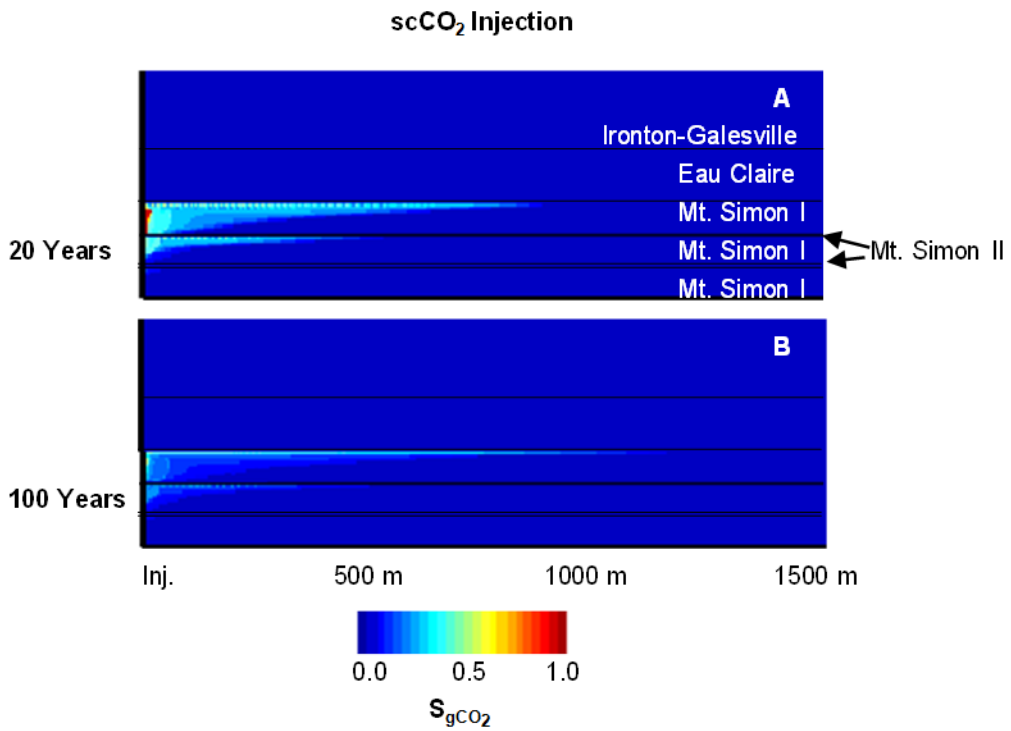

Figure 2. 8 a and b. Stratified formation CO_2 plumes at end of injection and end of monitoring period (V.E. 2x).

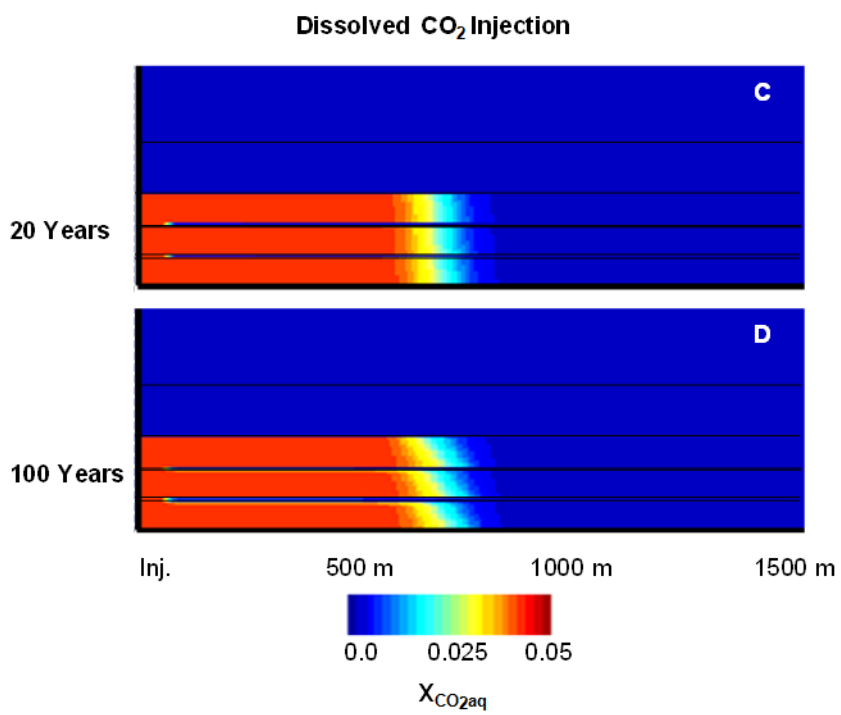

Figure 2. 9 c and d. Stratified formation CO_2 plumes at end of injection and end of monitoring

period (V.E. 2x).

Heterogeneous Formations

Flat-lying Formation

The $scCO_2$ plume spread 5.1 km^2 against the caprock after 20 years of injection into the more realistic, flat-lying heterogeneous storage formation. This was more than twice as far as simulated in the homogeneous model set-up and relates to a higher potential risk of leakage. The storage efficiency decreased to 1.6% (Figure 2.10). The flow was unstable with mobility ratio of 9 and a maximum velocity of 5 m/day in a high permeability zone near the top of the formation.

The dissolved CO_2 plume was more affected by the high permeability layers than the $scCO_2$ (Figure 2.10b). It spread farther than the $scCO_2$ plume along the caprock at 5.9 km^2 and reached a maximum extent of 15.9 km^2 within the formation. This resulted in a storage efficiency of 0.5%. At the end of injection, the dissolved CO_2 plume within the central high permeability layer was traveling at a maximum Darcy velocity of 32.9 m/day.

The $scCO_2$ plume spread to a total of 6.16 km^2 against the caprock in the 80 years post-injection, reducing the storage efficiency to 1.4% (Figure 2.11c). The plume remained unstable, with mobility ratio of 9. The maximum Darcy velocity was reduced to 7 mm/day from 5 m/day. Following from the stratified model set-up, the heterogeneous case yielded a higher dissolved portion of $scCO_2$ than the homogeneous models due to the increased surface area of the plume. By the end of the monitoring period, 35% of the

CO_2 was trapped in the dissolved phase with 0.94 $MtCO_2$ dissolved into formation water during the first 20 years and an additional 0.15 $MtCO_2$ dissolved into formation brine during the monitoring period.

The CO_2 plume post-dissolved injection did not significantly expand, remaining at 5.9 km^2 against the caprock and 15.9 km^2 within the formation (Figure 2.11d). The storage efficiency remained unchanged. The maximum Darcy velocity within the plume was 4 mm/day.

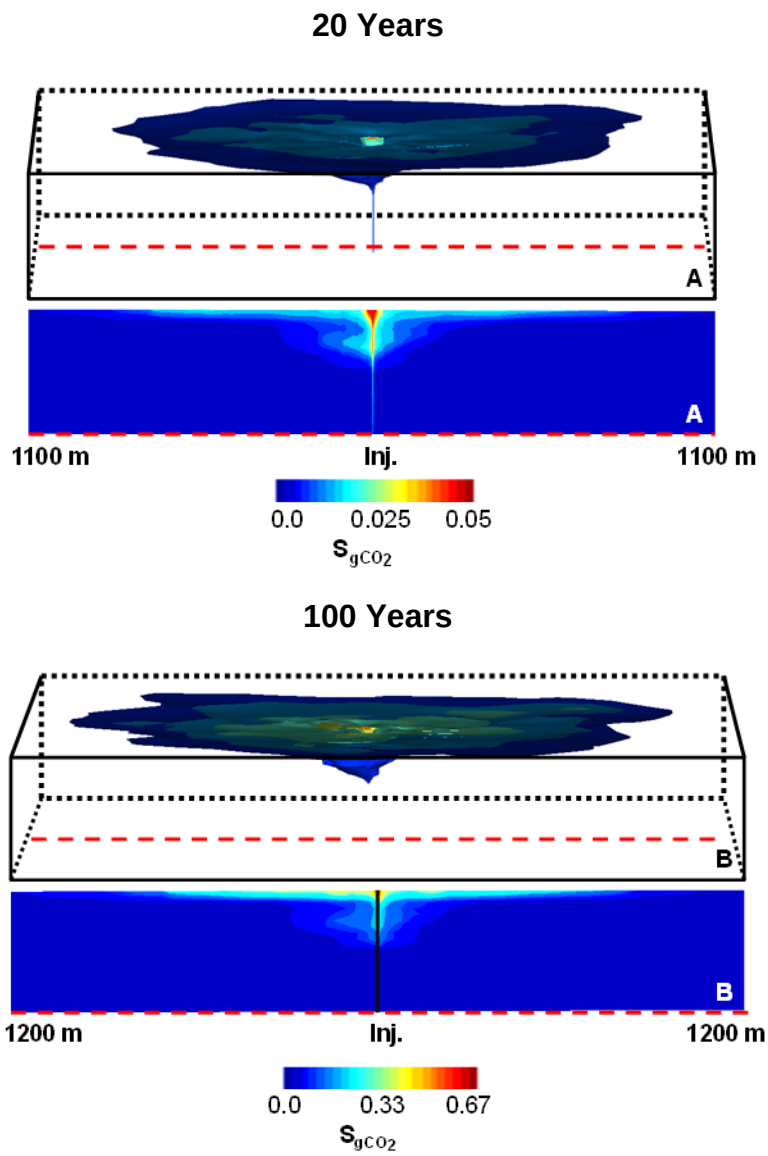

Figure 2. 10 a and b. $scCO_2$ injection into flat-lying heterogeneous formation. $ScCO_2$ plumes at the end of injection and end of monitoring period (V.E. 2x)

20 Years

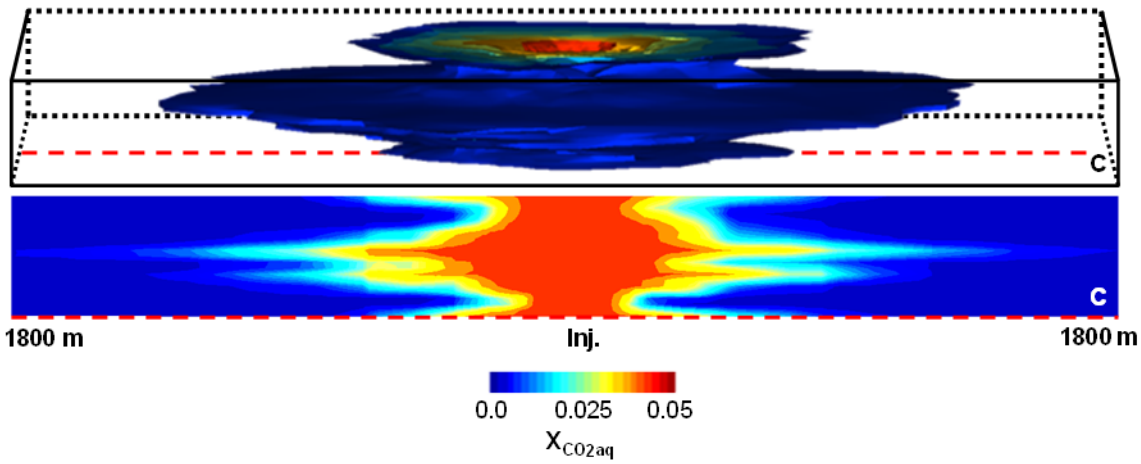

100 Years

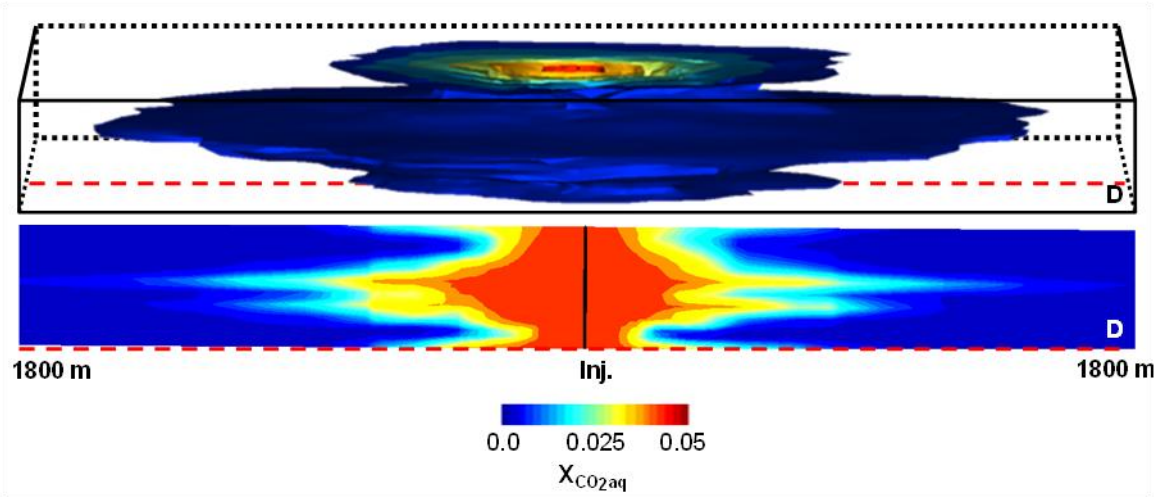

Figure 2. 11 c and d. Dissolved CO_2 injection into flat-lying heterogeneous formation. Plumes at the end of injection (c) and end of monitoring (d) period (V.E. 2x).

Dipping Formation

The 5º incline caused $scCO_2$ to spread up-dip across the formation thickness as it was injected. Therefore, the $scCO_2$ plume had a smaller footprint against the caprock following injection compared to the flat-lying case, at 3.73 km^2. This resulted in a storage efficiency of 2.2% (Figure 2.12a). The mobility ratio was 10. The maximum Darcy velocity was 1.1 m/day. This velocity was less than the maximum reached from the flat-lying case (5 m/day) because the high permeability zone that promoted the previous high velocity is on the down-slope side of this model.

The dissolved CO_2 plume was less affected by the dipping formation than the $scCO_2$ plume. The dissolved plume again spread 5.9 km^2 against the caprock. It showed a slightly increased extent within the formation due to gravity effects at 16.1 km^2 but resulted in the same storage efficiency of 0.5% (Figure 2.12b). The dissolved CO_2 plume traveled at a maximum velocity of 33 m/day in the central high permeability zone.

The $scCO_2$ plume spread 6.6 km^2 against the caprock during the monitoring period, reducing the storage efficiency to 1.4% (Figure 2.13c). This scenario resulted in the largest plume extent on the caprock and the lowest sweep efficiency of $scCO_2$. However, the mobility ratio was reduced to less than one as CO_2 contacted formation water more quickly in this case than the other cases. This was the only stable flow result in all the $scCO_2$ injection model set-ups. The maximum velocity was 1.7 cm/day. Supercritical CO_2 dissolution occurred more quickly than in any other case, with 1.19 $MtCO_2$ dissolving into formation water during the first 20 years and an additional 0.47

$MtCO_2$ dissolved into formation brine during the monitoring period. Overall, 53% of the injected $scCO_2$ was trapped in the dissolved phase by the end of monitoring.

The dissolved CO_2 plume continued to sink during the monitoring period, reducing the areal extent against the caprock to 5.8 km^2 and increasing to 16.2 km^2 within the formation (Figure 2.14d). This slight sinking led to no appreciable change in storage efficiency. The dissolved CO_2 was traveling predominantly down-dip at maximum velocity of 4.6 mm/day. This is the only case where dissolved CO_2 is traveling at a higher maximum velocity than $scCO_2$ after the monitoring period.

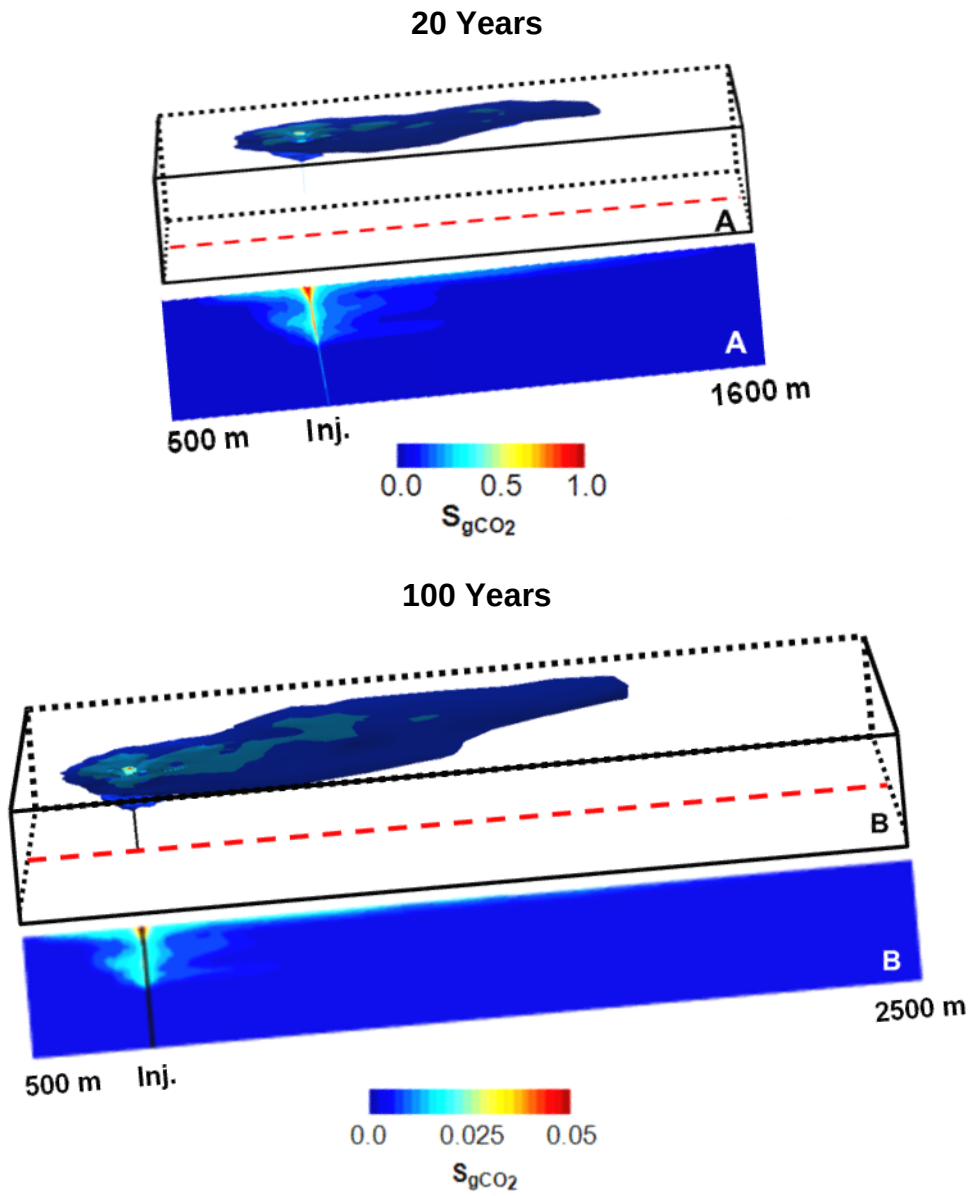

Figure 2. 12. a and b. $scCO_2$ injection into 5° dipping heterogeneous formation. $scCO_2$ plumes at the end of injection (a) and end of monitoring period (b) (V.E. 2x).

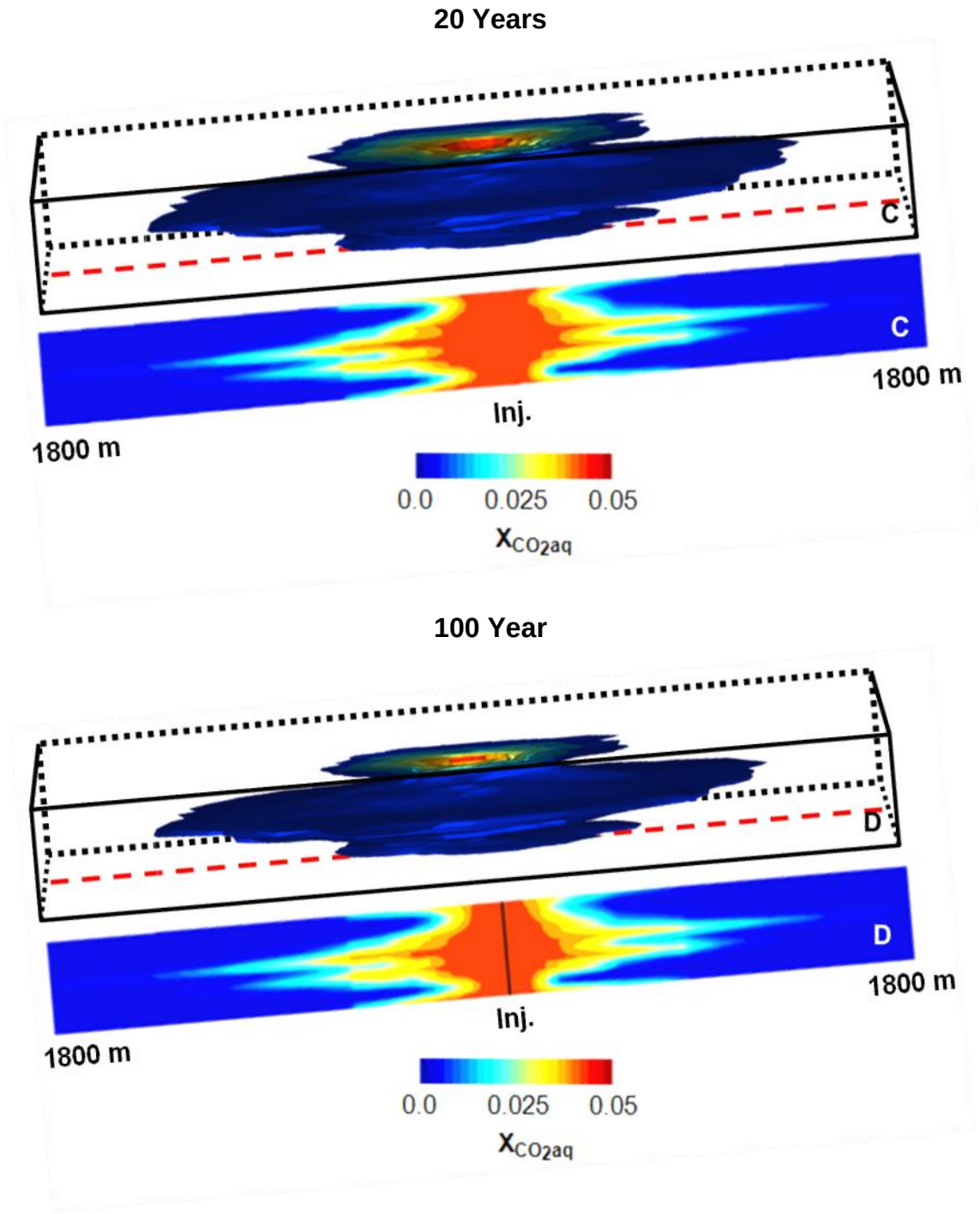

Figure 2. 13 c and d. Dissolved CO_2 injection into 5° dipping heterogeneous formation. Plumes at the end of injection (c) and end of monitoring (d) (V.E. 2x).

Compilations of CO_2 plume results are summarized in the tables in Appendix A.

Pressure Buildup

Regional scale models in the homogeneous and stratified cases allow for comparisons of the influence of the permeability variations on lateral and vertical pressure buildup in both injection scenarios. In the homogeneous case, pressure buildup equivalent to one meter of hydraulic head rise (0.01 MPa) extended laterally out 30 km beyond $scCO_2$ injection versus 70 km for dissolved CO_2 injection (Figure 2.14). Maximum pressure was applied along the caprock near $scCO_2$ injection reaching near 0.34 MPa (Figure 2.15). Pressure buildup was uniform, top to bottom, across the storage formation for dissolved CO_2 injection, reaching a maximum near the injection well at 5.3 MPa. During the monitoring period, the pressure buildup associated with the $scCO_2$ plume dissipated entirely beneath 1 m head rise. As the pressure footprint of the dissolved plume settled, it spread to 130 km from injection point.

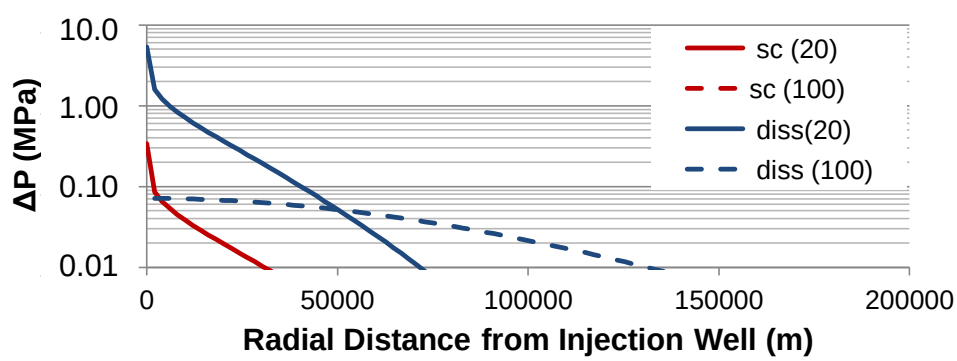

Figure 2. 14. Pressure buildup around the injection well.

Figure 2. 15. Pressure buildup in the homogeneous case. Contours to 10 m head rise. Distances from the injection at the bottom of formation

The stratified formation experienced a greater pressure buildup as confining layers within the storage unit hindered vertical pressure dissipation both during and after injection (Figure 2.16). This effect was more extreme for $scCO_2$ injection as most of the injected fluid flowed into the top storage layer. The top layer within the storage formation underwent a lateral pressure increase equivalent to 1 m head rise to 50 km and experienced a maximum pressure buildup near injection along the caprock of 0.45 MPa (Figure 2.17). The equivalent pressure buildup for the dissolved case reached 80 km, and the formation experienced a 6.14MPa increase near injection. Similarly, both scenarios recovered more slowly than in the homogeneous case, particularly the $scCO_2$ injection scenario. By the end of monitoring, the pressure buildup in both injection scenarios resulted in 2 m head rise to 150 km. In all stratified cases the sealing layers were able to contain the vertical pressure buildup by 1 km depth from the surface (Figure 2.18).

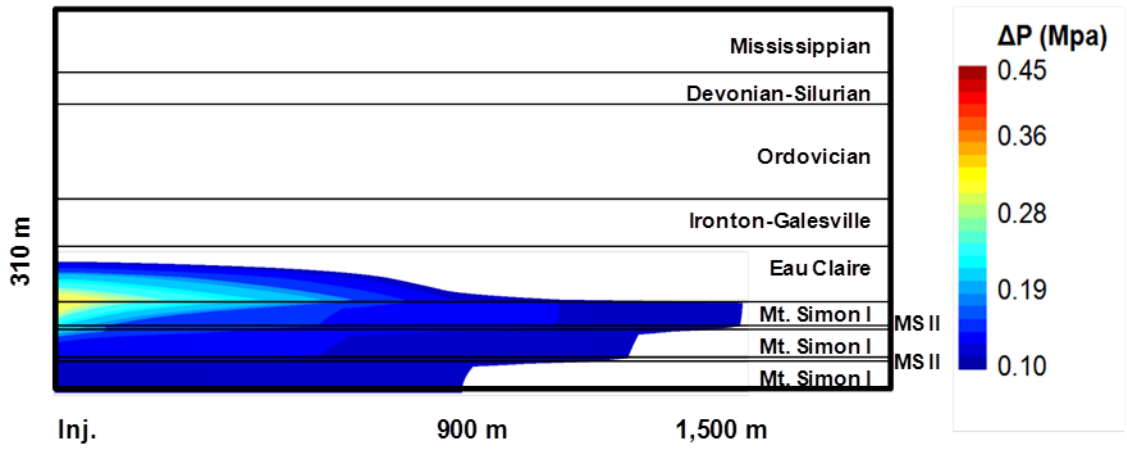

Figure 2. 16. Pressure buildup and material layers in the stratified case. Contours to 10 m head rise. Distances from injection at the bottom of formation.

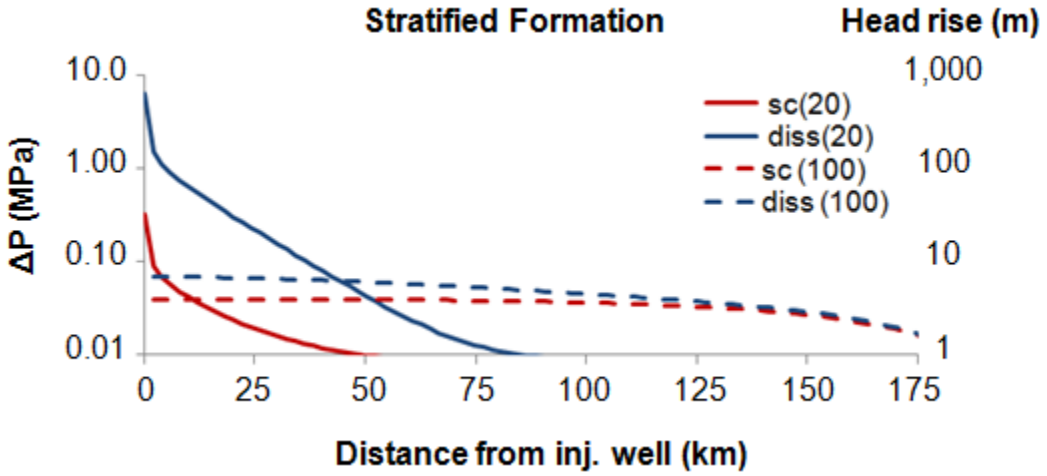

Figure 2. 17. Lateral pressure buildup within the top layer of storage formation.

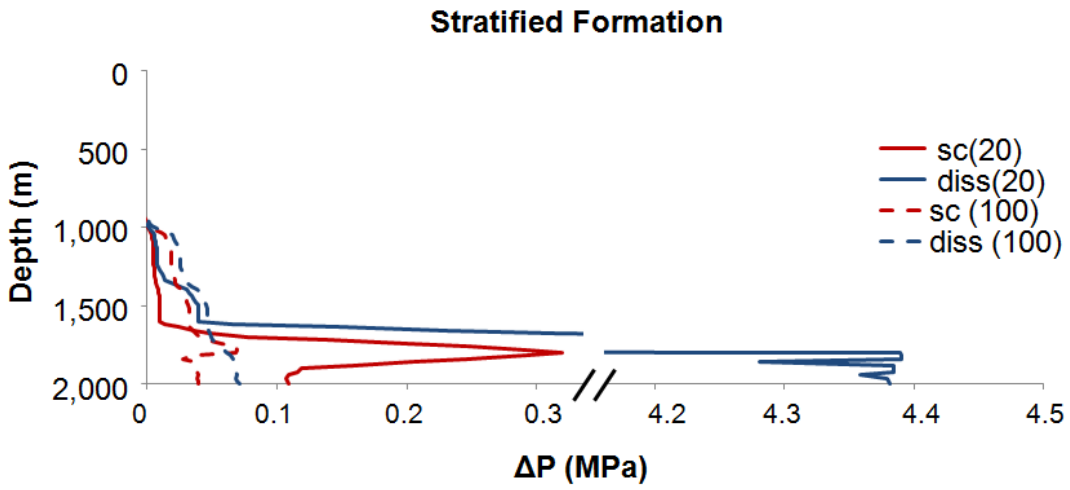

Figure 2. 18. Vertical pressure buildup 10 m from injection well.

Discussion

Supercritical CO_2 injection into the dipping heterogeneous model set-up resulted in an accelerated $scCO_2$ plume growth but also accelerated dissolution to 53% of the injected CO_2. This was the only case to reduce the average mobility ratio to unity. These results are in agreement with published literature that also found dipping formations enhanced dissolution and residual CO_2 trapping (Doughty et al., 2004; Hesse et al., 2008; MacMinn et al., 2010; Pruess and Nordbottom, 2011). By enhancing residual CO_2 trapping, the relative permeability of CO_2 to water was reduced, thus reducing the mobility and mobility ratio. This result suggests it may be favorable to inject $scCO_2$ into dipping formations, provided injection is far from structural imperfections or outcrops.

In the same heterogeneous cases, the dissolved CO_2 preferentially followed high permeability pathways while the $scCO_2$ plume was more influenced by buoyancy driven

flow. These results show that dissolved CO_2 injection into more realistic heterogeneous formations may not improve storage efficiency over standard $scCO_2$ injection as suggested by homogeneous model set-ups. In these models, the storage efficiency for dissolved CO_2 was actually less than the minimum estimates found in literature for $scCO_2$ storage. In general, the storage efficiency will be dependent on the highest permeability zone present in the storage formation. These results demonstrate the importance of including realistic heterogeneities in models as the different plume behavior between model set-ups leads to different conclusions.

Alternatively, the risks associated with the dissolved CO_2 plume are less than $scCO_2$ injection, improving the storage security. The dissolved CO_2 plume always had a smaller areal extent on the cap rock at the end of simulations due to the lack of buoyancy driven flow and there was not significant plume growth during the monitoring period. The plumes in the flat-lying and dipping formations showed the dissolved CO_2 plume was more influenced by the formation properties than the dipping aquifer.

At these rates, the biggest risk due to dissolved CO_2 injection is the greater pressure buildup. Results showed dissolved CO_2 injection increased lateral pressure buildup by tens of kilometers over $scCO_2$ injection. As in these models, it will be important to have several capping formations for GCS sites, not only to mitigate leakage but also to mitigate vertical pressure buildup. In addition, a pressure management scheme will be important to reduce regional scale brine migration, most likely through the use of supply wells within or near the storage formation.

One option for dissolved CO_2 injection may be to incorporate it into existing brine disposal operations. This would reduce risks associated with additional pressure buildup, as pressure monitoring and management strategies are already in place. It could be argued that this dissolved CO_2 injection could be regulated under Class II permits, in which case, the permitting process would be quicker than applying for a new Class VI permit. This option would also reduce costs as the injection wells are already drilled and completed.

There are approximately 144,000 Class II injection wells in operation in the United States injecting over 2 billion gallons of brine every day (EPA, 2014a). Most of this brine is derived from oil and gas production water, and is disposed of 1,500 m below surface on average (EPA, 2014a; CADOC, 2014). Hundreds to thousands of Class II wells exist in states considering GCS projects (Figure 2.19) (EPA, 2011). For example, Texas injected 235 billion gallons of brine via Class II wells in 2013 (TXRRC, 2014). Assuming a 1,500m deep formation with 50,000 mg/l NaCl at 40ºC, TOUGH2-ECO2N calculated a CO_2 solubility of 45 g/l. At these conditions, 40 $MtCO_2$ could be stored each year if all the brine disposal wells injected CO_2 saturated brine.

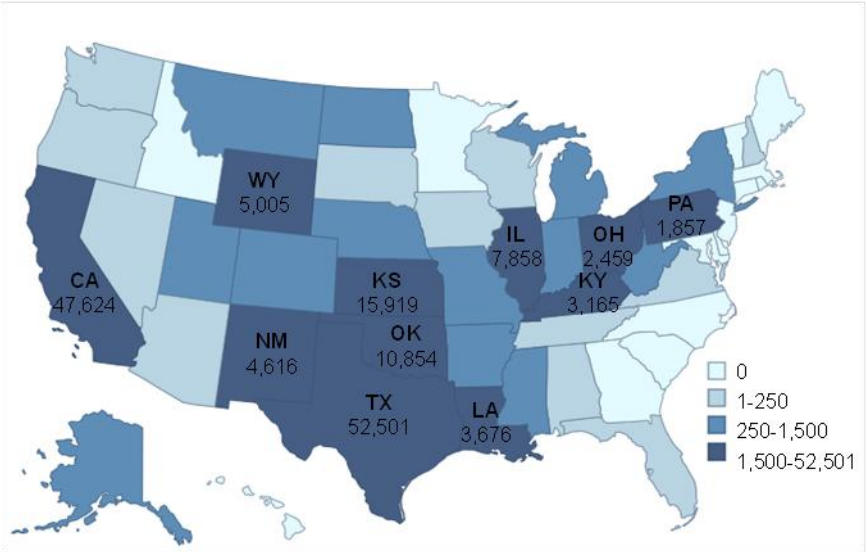

Figure 2. 19. Class II injection wells in the USA. Inventory data from the EPA (2011).

The actual CO_2 solubility in produced brine will vary between wells and will be dependent on pressure, temperature, salinity, and existing dissolved components. Produced water often contains salts and hydrocarbons and can also contain metals and trace elements (EPA, 2014b). Fortunately, vapor-liquid equilibria studies have shown in H_2O-CO_2-CH_4 systems the solubility of CO_2 in water increases in the presence of CH_4 for ranges and temperatures relevant to GCS (Qin et al., 2008; Oldenburg et al., 2013). Similar studies would need to be done to determine CO_2 solubility and associated chemical or physical reactions due to CO_2 dissolution for each potential site.

Conclusions

This paper compares supercritical and brine saturated injection strategies in order to determine the effects of injection methods on distribution and immobilization of injected CO_2 and pressure buildup within the storage formations. Simulation cases

increased in formation heterogeneity. Initially, simulations considered a homogeneous aquifer system, followed by simulations in a stacked aquifer system, and two final simulations were in aquifer systems heterogeneous in all directions, both flat lying and dipping at 5 degrees.

Based on results, the storage performance of $scCO_2$ injection was best in dipping formations where trapping occurred the most quickly, and flow was stabilized by the end of injection. In terms of storage security, dissolved CO_2 injection was favorable in all cases as it results in a smaller areal extent on the caprock and does not migrate appreciably beyond the injection period. However, in terms of storage efficiency, the dissolved CO_2 plume was less efficient than the $scCO_2$ plume. The pressure buildup due to dissolved CO_2 injection extended tens of kilometers farther than $scCO_2$ injection. Further work is recommended to explore possibilities of dissolved CO_2 injection via existing Class II brine disposal wells.

Works Cited

Ambrose, W., Ian Duncan, L., Holtz, M., Hovorka, S., Lopez, V., Lakshminarasimhan, S., 2006. Source-sink matching and potential for carbon capture and storage in the gulf coast. Technical report, The Gulf Coast Carbon Center, Bureau of Economic Geology, Jackson School of Geosciences, The University of Texas at Austin.

Bachu, S., 2002. Sequestration of CO_2 in geological media in response to climate change: road map for site selection using the transform of the geological space into the CO_2 phase space. Energy Convers Mgmt 43(1), 87-102.

Bachu, S., Bonijoly, D., Bradshaw, J., Burruss, R., Holloway, S., Christensen, N., Mathiassen, O., 2007. CO_2 Storage capacity estimation: methodology and gaps. Int. J. Greenh. Gas Control, 1(4), 430-443.

Bachu, S., 2008. Comparison between methodologies recommended for estimation of CO_2 storage capacity in geologic media—Phase III report. Carbon Sequestration Leadership Forum , Washington, D.C., USA., http://www.cslforum.org/publications/documents/PhaseIIIReportStorageCapacityEstimationTaskForce0408.pdf (Accessed May, 2014).

Barnes, D., Bacon, D., Kelley, S., 2009. Geological sequestration of carbon dioxide in the Cambrian Mount Simon Sandstone: regional storage capacity, site characterization, and large-scale injection feasibility. Environmental Geosciences, 16(3), 163-183.

Birkholzer, J. T., Zhou, Q., 2009. Basin-scale hydrogeologic impacts of CO_2 storage: capacity and regulatory implications. Int. J. Greenh. Gas Control, 3(6), 745-756.

Birkholzer, J., Zhou, Q., Tsang, C., 2009. Large-scale impact of CO_2 storage in deep saline aquifers. A sensitivity study on pressure response in stratified systems. Int. J. Greenh. Gas Control, 3(2), 181-194.

Burton, M., Bryant, S., 2007. Eliminating buoyant migration of CO_2 through surface dissolution: implementation costs and technical challenges. SPE 110650. SPE Ann. Tech. Conf. Exhib. Anaheim, CA.

Burton, M., Bryant, S., 2009. Surface dissolution: minimizing groundwater impact and leakage risk simultaneously. Energy Procedia, 1(1), 3707-3714.

California Department of Conservation (CADOC), 2014. Oil, gas, and geothermal-injection wells. http://www.conservation.ca.gov/dog/general_information/Pages/class_injection_wells.aspx (accessed May 2014).

Celia, M., Nordbottom, J., 2009. Practical modeling approaches for geologic storage of carbon dioxide. Groundwater, 47(5), 627-638.

Department of Energy NETL, 2007. Carbon sequestration atlas of the United States and Canada.

Department of Energy NETL, 2008. Carbon sequestration atlas of the United States and Canada.

Doughty, C., Pruess, K., 2004. Modeling supercritical carbon dioxide injection in heterogeneous porous media. Proceedings, TOUGH2 Symposium 2003. Lawrence Berkeley National Lab, Berkeley, CA, 12-14 May.

Doughty, C., Pruess, K., Benson, S., Freifeld, B., 2004. Hydrogeological and geochemical monitoring for a CO_2 sequestration pilot in a brine formation. Lawrence Berkeley National Lab, LBNL-55104.

Doughty, C., Freifeld, B., 2013. Modeling CO injection at Cranfield, Mississippi: Investigation of methane and temperature effects. Greenhouse Gas Sci Technol, 3(6), 475–490.

Edwards, A., 1972. TRUMP: A Computer Program for Transient and Steady State Temperature Distributions in Multidimensional Systems, National Technical Information Service, National Bureau of Standards, Springfield, VA.

Eke, P., Naylor, M., Haszeldine, S., Curtis, A., 2009. CO_2 -Brine surface dissolution and injection: CO_2 storage enhancement, Publication SPE 124711, Proceedings of the 2009 SPE Offshore Europe Oil & Gas Conference & Exhibition.Aberdeen, UK.

Environmental Protection Agency (EPA), 2011.UIC inventory by state 2011. http://water.epa.gov/type/groundwater/uic/upload/uicinventorybystate2011.pdf (accessed June 2014)

Environmental Protection Agency (EPA), 2014a. Class II wells – oil and gas related injection wells. http://water.epa.gov/type/groundwater/uic/class2/ (accessed June 2014).

Environmental Protection Agency (EPA), 2014b. Produced water reuse and recycling challenges and opportunities across major shale plays. http://www2.epa.gov/hfstudy/produced-water-reuse-and-recycling-challenges-and-opportunities-across-major-shale-plays (accessed May 2014).

Fang, Y., Baojun, B., Dazhen, T., Dunn-Norman, S., Wronkiewicz, D., 2010. Characteristics of CO_2 sequestration in saline aquifers. Pet. Sci., 7, 83-92.

Finsterle, S.,1999. iTOUGH2 User's Guide, Report LBNL-40040, Lawrence Berkeley National Laboratory, Berkeley, CA.

Garcia, J., 2003. Fluid dynamics of carbon dioxide disposal into saline aquifers. PhD Thesis, University of California at Berkeley, December 2003.

Garcia, J., K. Pruess, 2003. Flow instabilities during injection of CO_2 into saline aquifers. TOUGH Symposium 2003, Berkeley, California.

Gorecki, C., Sorensen, J., Bremer, J., Knudsen, D., Smith, S., Steadman, E., Harju, J., 2009. Development of storage coefficients for determining the effective CO_2 storage resource in deep saline formations. Society of Petroleum Engineers International Conference on CO_2 Capture, Storage and Utilization Proceedings, San Diego Calif., 2-4 November, SPE No. 126444..

Hagoort, J., 1988. Fundamentals of gas reservoir engineering. Elsevier Science Publ, 23.

Hesse, M., Orr, F., Tchelepi, H., 2008. Gravity currents with residual trapping. Journal of Fluid Mechanics, 611, 35-60.

Homsy, G. M., 1987, Viscous fingering in porous media. Ann. Rev. Fluid Mech., 19, 271–31.

Ide, S., Jessen, K., Orr, F., 2007. Storage of CO_2 in saline aquifers: effects of gravity, viscous, and capillary forces on amount and timing of trapping. Int. J. Greenh. Gas Control, 1(4), 481-491.

Intergovernmental Panel on Clim. Change (IPCC), 2005. Underground geologic storage: IPCC special report on carbon dioxide capture and storage, Chap. 5. Cambridge University Press, New York.

International Energy Agency Greenhouse Gas R&D Programme (IEAGHG), 2010. Injection strategies for CO_2 storage sites, 2010/04

International Energy Agency (IEA), 2013. Methods to assess CO_2 storage capacity: status and best practice. IEA, Paris, France.

Jain, L., Bryant, S., 2011. Optimal design of injection/extraction wells for surface dissolution CO_2 storage strategy. Energy Procedia, 4, 4299-4306.

Juanes, R., MacMinn, C., Szulczewski, M., 2010. The footprint of the CO_2 plume during carbon dioxide storage in saline aquifers: storage efficiency for capillary trapping at the basin scale. Transport in Porous Media 82(1), 19-30.

Keith, D., Hassanzadeh, H., Pooladi-Darvish, M., 2005. Reservoir engineering to accelerate dissolution of CO_2 in brines. Proceedings of 7th International Conference on Greenhouse Gas Control Technologies, Pergamon.

Kiraly, L., 2002. Karstification and groundwater flow. Proceedings of the Conference on Evolution of Karst: From Prekarst to Cessation. Postojna-Ljubljana, Institut za raziskovanje krasa, ZRC SAZU, 155-90.

Kumar, A., Noh, M., Pope, G., Sepehrnoori, K., Bryant, S., Lake, L., 2004. Reservoir simulation of CO_2 storage in deep saline aquifers. Proceedings, SPE/DOE Symposium on Improved Oil Recovery, Tulsa, OK, 17-18 April.

Lake, L. W., 1989. Enhanced Oil Recovery. NJ: Prentice Hall.

Lemmon, E.W., McLinden, M.O., Friend, D.G., 2011. Thermophysical properties of fluid systems. NIST chemistry WebBook. NIST Standard Reference Database Number 69. Eds. P.J. Linstrom and W.G. Mallard, National Institute of Standards and Technology, Gaithersburg MD.

Leonenko, Y., D. Keith, 2008. Reservoir engineering to Accelerate the dissolution of CO_2 dtored in aquifers. Environ. Sci. Technol. 42, 4742-2747.

Leonenko, Y., Keith, D., Pooladi-Darvish, M., Hassanzadeh, H., 2006. Accelerating the dissolution of CO_2 in aquifers. 8TH International Conference on Greenhouse Gas Control Technologies, Trondheim, Norwaym, 19-22 June.

Lloyd, O. B., Lyke, W. L., 1995. Illinois, Indiana, Kentucky, Ohio, Tennessee HA 730-K. ground water atlas of the United States. Reston, VA: U.S. Geological Survey.

Luckner, L., Van Genuchten, M.T., Nielson, D.R., 1989. A consistent set of parametric models for the two-phase flow of immiscible fluids in the subsurface. Water Resour. Res. 25(10), 2187-2193.

MacMinn, C., Juanes, R., 2009. Post-injection spreading and trapping of CO_2 in Saline Aquifers: Impact of the Plume Shape at the End of Injection. Comput. Geosci., 13, 483-491.

MacMinn, C., Szulczewsk, M., Juanes, R., 2010. CO_2 migration in saline aquifers. Part 1. Capillary trapping under slope and groundwater flow. Journal of Fluid Mechanics, 662, 329-351.

Mast, R. F., Howard, R. H., 1990. Oil and gas production and recovery estimates in the Illinois basin. Interior cratonic basins: AAPG Memoir, 51, 295-298.

Michael, K., Neal, P., Allison, G., Ennis-King, J., Hou, W., Paterson, L., Sharma, S., Aiken, T., 2011. Injection strategies for large-scale CO_2 storage sites. Energy Procedia, 4, 4267-4274.

Mualem, Y., 1976. A new model for predicting the hydraulic conductivity of unsaturated porous media. Water Resour. Res. 12(3), 513-522.

Narasimhan, T., Witherspoon. P., 1976. An integrated finite difference method for analyzing fluid flow in porous media. Water Resour. Res., 12(1), 57 – 64.

Oldenburg, C., Doughty, C., Spycher, N., 2013. The role of CO_2 in CH_4 exsolution from deep brine: implications for geologic sequestration. Greenhouse Gas Sci Technol., 3, 359-277.

Okwen, R., Stewart, M., Cunningham, J., 2010. Analytical solution for estimating storage efficiency of geologic sequestration of CO_2. Int. J. Greenh. Gas Control, 4(1), 102-107.

Orr, F., 2009. Onshore Geologic Storage of CO_2. Science 325, 1656.

Patterson, C., 2011. A history-dependent nonwetting-phase trapping model for multiphase flow characteristic curves. Master's Thesis, Clemson University, August 2011.

Patterson, C., Falta, R.W., 2012. A simple history-dependent nonwetting-phase trapping model for the TOUGH simulations. Proceedings of the TOUGH Symposium 2012. Lawrence Berkeley National Laboratory, Berkeley, California. 17-19 September 2012.

Pruess, K., 2005. ECO2N: A fluid property module for mixtures of water, NaCl, and CO_2. LBNL- 57952, Lawrence Berkeley National Laboratory, Berkeley, CA

Pruess, K., Oldenburg, C., Moridis, G., 1999. TOUGH2 user's guide, version 2.0, Report LBNL-43134, Lawrence Berkeley National Laboratory, Berkeley, CA. Updated September 2012.

Pruess, K., Nordbottom, J., 2011. Numerical simulation studies of the long-term evolution of a CO_2 plume in a saline aquifer with a sloping caprock. Transport in Porous Media. 90, 135-151.

Qin, J., Rosenbauer, R., Duan, Z., 2008. Experimental measurements of vapor-liquid equilibria of the H2O+CO2+CH4 ternary system. J. Chem. Eng. Data., 53(6), 1246-1249.

Roache, P., 1972. Computational fluid dynamics. Hermosa, Albuquerque, NM, USA.

Szulczewski, M., MacMinn, C., Herzog., Juanes, R., 2012. The lifetime of carbon capture and storage as a climate-change mitigation technology: Supporting Information. Proceedings of the National Academy of Sciences of the United States of America (PNAS), 109(14), 5185-5189.

Spycher, N., Pruess, K., 2005. CO2-H2O mixtures in the geological sequestration of CO_2. II. Partitioning in chloride brines at 12–100 °C and up to 600 bar, Geochim. Cosmochim. Acta, 69(13), 3309–3320.

Szulczewski, M., MacMinn, C., Juanes, R., 2010. Basin-scale CO_2 storage capacity estimates from fluid dynamics. Proceedings, XVIII International Conference on Water Resources.

Tao, Q., Bryant, S., 2012. Optimal control of injection/extraction wells for the surface dissolution CO_2 storage strategy. Carbon Management Technology Conference.

Texas Railroad Commission (TXRRC), 2014. H10 filing system: Fluid Type Query. http://webapps.rrc.state.tx.us/H10/h10PublicMain.do (Accessed May 2014).

Van der Meer, L., 1992. Investigations regarding the storage of carbon dioxide in aquifers in The Netherlands. Energy Convers. Manage., 33(5-8), 611-618.

Van der Meer, L., 1995. The CO_2 storage efficiency of aquifers. Energy Convers. Manage. 36(6-9), 513-513.

Van Genuchten, M.T., 1980. A closed-form equation for predicting the hydraulic conductivity of unsaturated soils, Soil Sci. Soc. Am. J. 44, 892-898.

Visocky, A. P., Sherrill, M. G., Cartwright, K., 1985. Geology, hydrology, and water quality of the Cambrian and Ordovician systems in northern Illinois. Illinois State Water Survey and the Illinois State Geological Survey.

Yamamoto, H., Doughty, C., 2011. Investigation of gridding effects for numerical simulation of CO_2 geologic sequestrations, Int. Journal of Greenhouse Gas Control.

Zhou, Q., Birkholzer, J.T., Mehnert, E., Lin, Y., Zhang, K., 2010. Modeling basin- and plume-scale processes of CO_2 storage for full-scale deployment. Ground Water, 48(4), 494-514.

CHAPTER THREE:

HYSTERETIC TRAPPING AND RELATIVE PERMEABILITY OF CO_2 IN SANDSTONE AT RESERVOIR CONDITIONS

Introduction

Carbon dioxide migration through storage aquifers is characterized by drainage and imbibition processes. During drainage, water saturation decreases as it is displaced by advancing CO_2. During imbibition, water re-enters the pore-space at the trailing edge of the CO_2 plume, disconnecting and immobilizing bubbles of CO_2. In some cases, cycles of drainage and imbibition may occur, which may cause the disconnected CO_2 bubbles to coalesce and flow again. When this occurs, the fluid saturations do not solely depend on the current drainage or imbibition process, but also on the history of previous drainage and imbibition cycles; this is known as hysteretic behavior. One of the consequences of hysteresis is that the relative permeability to the nonwetting phase during imbibition can go to zero with a significant fraction of the nonwetting phase remaining in the pore space. This phenomenon is called residual trapping and is considered a secondary immobilizing mechanism of injected CO_2 (IPCC, 2005). Experimental studies report trapped gas saturation up to 40% for maximum CO_2 saturation ranging between 60% and 80% (Pentland et al., 2011; Krevor et al., 2012; Akbarabadi and Piri, 2013). The maximum CO_2 saturation prior to imbibition is also often referred to as the turning point or initial nonwetting phase saturation. From a practical perspective, the effect of residual trapping is significant because it determines how far the CO_2 migrates (Doughty, 2007; Qi et al., 2009; Pentland et al., 2011) and, ultimately, the distribution of the CO_2 plume (Juanes et

al, 2006; Krevor et al., 20012; Killough, 1976).

Including hysteresis in numerical models can have important effects on the predicted CO_2 distribution. Numerical models that use non-hysteretic characteristic curves can over-predict the total trapped CO_2 saturation in the trailing edge of the CO_2 plume, while under-predicting the mobility of the leading edge of the CO_2 plume (Doughty, 2007). This effect was particularly strong where high residual saturations were used (Parker and Lenhard, 1987; Lenhard and Parker, 1987; Niemi and Bodvarsson, 1988; Kaluarachchi and Parker, 1992; Doughty, 2007; Fagerlund et al., 2008). For CO_2 storage in heterogeneous formations, Doughty (2007) showed that the use of hysteretic models during injection is of added importance, as both drainage and imbibition processes could occur throughout the whole simulation period due to the subtle interplay between fluid flow and geologic heterogeneity.

Following capillary pressure and relative permeability measurements for CO_2/brine systems, recent experimental studies have began investigating residual CO_2 trapping upon imbibition (Pentland et al., 2010, 2011; Krevor et al., 2012; Akbarabadi and Piri, 2013). Pentland et al. (2010) measured trapped nonwetting phase saturation as a function of initial saturation in sandpacks. Refined oil was used as an analog for supercritical CO_2 ($scCO_2$) in an oil/brine system. The sandpack columns were flooded with the fluids and saturations were analyzed by gas chromatography (GC). Four experiments were performed consisting of one drainage and one imbibition core flood. Average data were taken from 10 column slices. Experimental data were fit by several trapping models. The

best fits were provided by the linear trapping model of Aissaoui (1983), $R^2 = 0.974$, and the quadratic function of Spiteri et al. (2008), $R^2 = 0.969$. Pentland et al. (2011) measured primary drainage capillary pressure and the relationship between initial and residual nonwetting phase saturation for a $scCO_2$/brine and oil/brine systems in Berea sandstone by the semipermeable disk core-flood method. Drainage and imbibition steps were repeated to vary the initial saturation. Residual saturation measurements were taken using isothermal depressurization of the pore space. Krevor et al. (2012) investigated Berea sandstone and three potential reservoir rocks for $scCO_2$ injection using the steady-state method in a horizontal core-flooding apparatus with fluid distributions observed using X-ray computed tomography (CT). Primary drainage curves were measured in the four rocks, thus nonhysteretic capillary pressure and relative permeability curves were characterized. Following drainage, Krevor et al. (2012) performed one 100% water flood to collect residual gas saturation measurements. Trapping was characterized based on slice averaged saturations across the core at maximum and residual saturations. Results were fit by both Land (1968) and Spiteri et al. (2008) models. Akbarabadi and Piri (2013) performed unsteady and steady-state drainage and imbibition full-recirculation flow experiments in three different sandstone rock samples to study the effects of hysteresis on capillary trapping and relative permeability of $scCO_2$/brine systems at reservoir conditions. Carbon dioxide saturation was increased from zero each cycle. In this case, the ratio of residual to initial CO_2 saturation was shown to be higher for low initial saturations. Following these experiments, the question remains whether the CO_2 trapping relationships observed are consistent when a pore space undergoes *repeated* cycles of

drainage and imbibition. That is to say, a scenario in which secondary drainage occurs without returning to 100% water (or brine) saturation between cycles. Further, how does the hysteretic trapping relationship influence the CO_2 relative permeability and capillary pressure and how can the associated curves be characterized?

This study had three main objectives: (1) to characterize the relationship between residually trapped CO_2 saturations and turning point CO_2 saturations of a CO_2 /water system in sandstone at reservoir conditions, (2) to calculate hysteretic relative permeability data, and (3) to characterize an appropriate gas trapping model and hysteretic relative permeability curve for use in carbon storage applications. We investigated hysteresis in residual trapping and relative permeability of CO_2 in a CO_2 /water system at 50ºC and 9 MPa in a Berea sandstone core. Saturation data were measured with X-ray computed tomography (CT) using a steady-state method in a horizontal core-flooding apparatus. Water and supercritical CO_2 were simultaneously injected into a water-saturated core. Three cycles of drainage and imbibition were completed by incrementally increasing and decreasing the flow rates of CO_2 and water, while maintaining the total volumetric flow rate into the core. The cycles were performed such that the turning point saturation of each cycle was greater than that of the previous cycle. CT scans were taken to determine saturation, and pressure drop over the core was used to determine the relative permeability during the test. Residual CO_2 saturations were extrapolated from the minimum CO_2 saturations of each cycle.

Theory

The trapping characteristics of a given fluid-pair system are commonly presented through the so-called initial-residual (IR) curve, where the nonwetting phase residual saturation (S_{nr}) is plotted as a function of the saturation at turning point saturation (Lake, 1989). Several trapping models from petroleum engineering and contaminant transport literature have been fit to experimental data to characterize residual trapping in gas/water, gas/oil, or non-aqueous phase liquid (NAPL)/water fluid systems in consolidated and unconsolidated media (Land 1968; Aissaoui, 1983; Jerauld,1997; Kleppe et al., 1997; Steffy et al., 1997; Johnson and Adamski, 2005; Spiteri et al., 2008). The most commonly used nonwetting phase trapping model is the Land equation (Land, 1968)

$$S_{\mathrm{nr}} = \frac{S_{\mathrm{ni}}}{1 + CS_{\mathrm{ni}}} \tag{3. 1}$$

where S_{nr} is the trapped nonwetting phase saturation, S_{ni} is its turning point saturation and C is the Land coefficient. More recent trapping relationships use linear models of the form (Aissaoui, 1983; Kleppe et al., 1997; Steffy et al., 1997; Johnson and Adamski, 2005)

$$S_{\mathrm{nr}} = f_{\mathrm{r}} S_{\mathrm{ni}} \tag{3. 2}$$

where f_r is the fraction of S_{ni} trapped. In this paper, each of these models is fit to experimental data for comparison.

The trapping phenomenon affects the dynamics of multiphase flows through the dependency of the relative permeability curve on the local saturation history of the

porous medium. Therefore, the relationship between relative permeability and saturation should account for the trapping behavior described by one of the models listed above. For systems having a strong wettability preference (to either oil, water, or gas), the relative permeability to the wetting phase tends to depend solely on its own saturation and hysteresis can be neglected (Dullien, 1979); several methods are available to obtain a complete imbibition relative permeability curve for the nonwetting phase (Killough, 1976; Carlson, 1981). In the approach followed, we used an effective saturation that includes a trapping term (Patterson and Falta, 2012). Two definitions of the effective saturation were used, depending on whether the relative permeability to the wetting or to the nonwetting phase is considered:

$$\bar{S}_{\mathrm{w}} = \frac{S_{\mathrm{w}} - S_{\mathrm{wr}}}{1 - S_{\mathrm{wr}}} \tag{3. 3}$$

$$\hat{S}_{\mathrm{w}} = \frac{S_{\mathrm{w}} - S_{\mathrm{wr}}}{1 - S_{\mathrm{wr}} - S_{\mathrm{nr}}} \tag{3. 4}$$

where $\bar{S}$ is the effective wetting-phase saturation for the wetting curve, $\hat{S}$ is the effective wetting-phase saturation for nonwetting curves, S_{w} is the wetting phase saturation, and S_{wr} is the wetting phase residual (irreducible) saturation (Luckner et al., 1989).

Relative permeability for gas-liquid systems can be described by the wetting-phase relative permeability (Dury et al. 1999)

$$k_{\mathrm{rw}} = \bar{S}_{\mathrm{w}}{}^{C}\left[1-\left(1-\bar{S}_{\mathrm{w}}\right)^{A}\right]^{B} \tag{3. 5}$$

and the nonwetting phase relative permeability

$$k_{\mathrm{rnw}} = \left(1-\hat{S}_{\mathrm{w}}\right)^{C}\left(1-\hat{S}_{\mathrm{w}}{}^{A}\right)^{B} \tag{3. 6}$$

where *A*, *B*, and *C* are parameters that depend on the framework used to develop the relative permeability-saturation relationship (Table 3. 1). The first term, $\bar{S}_{\mathrm{w}}{}^{C}$ or $\left(1-\hat{S}_{\mathrm{w}}\right)^{C}$, is an empirical factor describing the connectivity and tortuosity of the pores (Kresic, 2007) and the second term, $\left[1-\left(1-\bar{S}_{\mathrm{w}}\right)^{A}\right]^{B}$ or $\left(1-\hat{S}_{\mathrm{w}}{}^{A}\right)^{B}$, represents the capillary model. When *A* and *B* are zero, a simple power function model is given (Fatt and Klikoff, 1959; Wyllie, 1962). The Burdine (1953) and Mualem models (1976) derive the second term from the definition of the capillary pressure curve, typically given by the Brooks and Corey (1964) or Van Genuchten (1980) equations. The resulting expressions for the parameters *A*, *B*, and *C* are summarized in Table 3. 1, giving commonly used *C* values for each of the corresponding models. In this paper, *A*, *B*, and *C* are fit to data for the Brooks and Corey-Burdine, Brooks and Corey-Mualem, Van Genuchten-Burdine and Van Genuchten-Mualem curves.

Table 3. 1. Commonly used nonwetting relative permeability parameters for use in equations 5 and 6.

Model	***A***	***B***	***C***
Power	-	-	3
Brooks and Corey - Burdine	$(2+\lambda)/\lambda$	1	2
Brooks and Corey - Mualem	$(1+\lambda)/\lambda$	2	0.5
Van Genuchten - Burdine	$1/m$	m	2
Van Genuchten - Mualem	$1/m$	$2m$	0.5

The effective saturation definitions are applied to a relative permeability relationship that takes the same functional form as a non-hysteretic function. In particular, in order to compute nonwetting phase relative permeability values, the method is applied as follows:

(1) S_{wr} is a constant and used as a fitting parameter.

(2) On the primary drainage curve, S_{nr}, and accordingly, $\hat{S}_w$, are continuously updated based on the actual saturation S_w, where $S_w = 1 - S_{ni}$.

(3) Imbibition scanning curves are constructed based on a constant S_{nr}, which depends on the saturation at the turning point, e.g. equation 1 or 2.

(4) Drainage scanning curves are set to be equal to the corresponding imbibition scanning curve until the primary drainage curve is reached.

Relative permeability can be experimentally measured using fractional flow theory. By this method, fractional flow of each phase is defined as the ratio between the volumetric flow rate of that phase and the total volumetric flow rate at reservoir conditions (Pope, 1980).

$$ff_{\beta} = \frac{Q_{\beta}}{Q_{TOT}} \tag{3. 7}$$

$$Q_{TOT} = \sum_{\beta} Q_{\beta} \tag{3. 8}$$

where ff_{β} is the fractional flow rate of the phase β, Q_{TOT} is the total volumetric flow rate, and Q_{β} is the volumetric flow rate (m^3/s) of the phase β. It is assumed that the fluids are incompressible; therefore, densities of both phases are taken to be constant. At steady state, the assumption is made that the pressure drop is the same in both phases due to the uniform saturation and hence capillary pressure is zero. The relative permeability in both phases is then calculated from Darcy's law for multiphase flow using

$$k_{r\beta}(S_{\beta}) = -\frac{Q_{\beta}\mu_{\beta}L}{kA\Delta P(S_{\beta})} \tag{3. 9}$$

where μ is viscosity (Pa•s), L is length of the core (m), k is absolute permeability (m^2), A is the transverse cross sectional area of the core (m^2), and ΔP is pressure drop across the core (Pa) at a particular saturation.

Materials and methods

A Berea sandstone core similar to potential CO_2 storage formations was used for experiments conducted at reservoir temperatures and pressures. Porosity and absolute permeability were determined prior to the relative permeability experiments. Pre-equilibrated $scCO_2$ and water were co-injected into the core using a steady-state method

in a horizontal core flooding apparatus. CT scans were taken of the core to measure fluid saturation. Three cycles of drainage and imbibition were conducted.

Equipment

Horizontal core flooding system

The core flooding apparatus was designed to allow immiscible fluids to continuously circulate through the system (Figure 3. 1) and is described in detail in previous studies (Perrin and Benson, 2009; Krevor et al., 2012). An aluminum core holder housed the rock core wrapped in heat shrinkable teflon to prevent fluid loss, a nickel foil layer to prevent CO_2 diffusion, a second layer of teflon, and a viton rubber sleeve. Two pressure transducers (Oil filled Digiquartz Intelligent Transmitter, model 9000-3K-101) were attached to the core holder, one at the inlet and one at the outlet. Two dual-pump systems (Teledyne Isco, model 500D) were used to simultaneously circulate fluids through a heat exchanger and into the core during experiments. Additionally, a displacement pump (Teledyne Isco, model 260D) was used to apply an overburden pressure on the core. This experiment included modifications to allow two injection lines into the inlet cap of the core holder. The inlet cap was carved to include tracks for both CO_2 and water to enter the core. The new design ensured the fluid phases entered the core separately and evenly, and allowed the pressure drop across the core within the wetting phase to be measured.

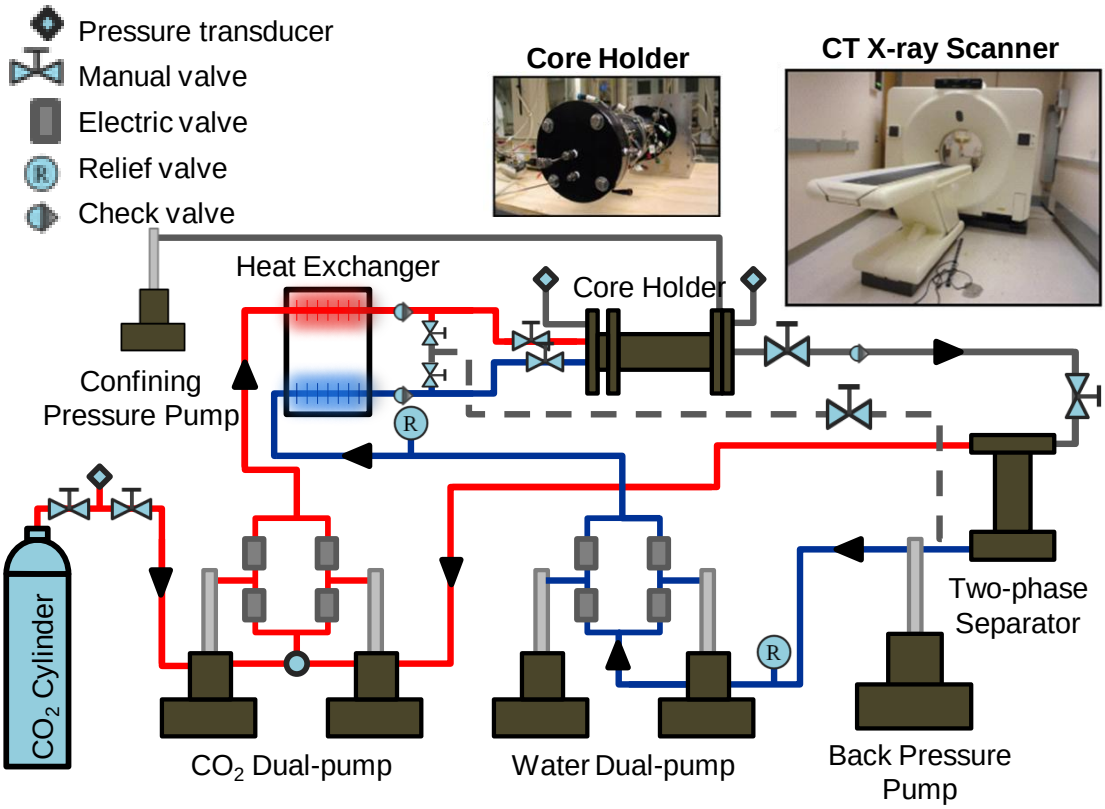

Figure 3. 1. Horizontal core flooding experimental setup and photographs of the core holder and CT x-ray scanner. Modified from Krevor et al. (2012) so that CO_2 and water lines enter the inlet separately.

The system was brought to reservoir conditions of 9 MPa fluid pressure and 12.4 MPa confining pressure. To ensure an experimental temperature of 50ºC, the confining fluid was heated using an electric heater. A pump (Teledyne Isco, model 1000D) was used to maintain the outlet pressure in the core at 9 MPa. Upon exiting the core, fluids entered a two-phase separator (TEMCO AMS-900), were redistributed to their respective dual-pump systems, and continued circulating.

Computed tomography imaging

A General Electric Hi-Speed CT/I x-ray computed tomography scanner was used to collect saturation data during the core flooding experiment (Figure 3. 1). The core-flooding apparatus was built around and through the CT scanner such that the core holder could be passed through for x-ray scans. The scanner was used to construct 3D maps using 2D scans taken every 1 mm along the length of the core. The scanner provides converted x-ray attenuation coefficients as CT values (Akin and Kovscek, 2003; Krevor et al., 2012). Scans were performed at 120 kV and 200 mA with a field of view of 25 cm. CT values were used to calculate porosity distribution across the core and saturation data during relative permeability experiments using the following relationships:

$$\Phi = \frac{CT_{\text{watersat}} - CT_{\text{drycore}}}{I_{\text{water}} - I_{\text{air}}} \tag{3. 10}$$

$$S_{\text{CO}_2} = \frac{CT_{\text{exp}} - CT_{\text{watersat}}}{CT_{\text{CO}_2\text{sat}} - CT_{\text{watersat}}} \tag{3. 11}$$

where Φ is porosity, CT_{drycore}, CT_{watersat}, and $CT_{\text{CO}_2\text{sat}}$ are background CT values taken when the core was dry, fully water- or CO_2-saturated, respectively; I_{water} and I_{air} are CT values representing water or air, $I_{\text{water}} = 0$ and $I_{\text{air}} = -1000$, S_{CO_2} is the CO_2 saturation, and CT_{exp} is the CT value obtained during the multiphase displacement experiment (Akin and Kovscek, 2003; Krevor et al., 2012).

Rock and fluid properties

A homogeneous Berea sandstone sample was used for the core flooding experiments. The relatively high average porosity (19-26%) and permeability (~100–2,500 mD) of Berea sandstone are characteristic of target CO_2 storage formations (Churcher et al., 1991). The core measured 10 cm in length and 5 cm in diameter with no apparent bedding planes. The core was fired at 700ºC prior to experiments to stabilize swelling of clays. Carbon dioxide and tap water were injected into the core during experiments. Experimental conditions were 50ºC and 9 MPa, ensuring CO_2 remained above the critical point. The viscosity of the fluids were taken to be μ_{CO2} = 2.3 x 10^{-5} Pa•s for $scCO_2$ and $\mu_{w=}$ 5.5 x 10^{-4} Pa•s for water, and the densities of the fluids were calculated at ρ_{CO_2} = 282 kg/m^3 for $scCO_2$ and ρ_w = 992 kg/ m^3 for water (Lemmon et al., 2011).

Porosity measurement

After the preliminary scan of the dry core, the fluid lines and core were flushed with CO_2 to remove air from the system. The core was then pressurized with CO_2 up to 9 MPa. At this point, a CT scan was taken to provide the background scan of the core fully saturated with $scCO_2$. Subsequently CO_2 was vented from the core, which was allowed to depressurize to atmospheric pressure. Next, water with no dissolved CO_2 was introduced to the core and several pore volumes were injected at atmospheric pressure. Water in the core was then pressurized and at least ten pore volumes of water with no dissolved CO_2 were injected through the core to dissolve remnant CO_2. At this point a scan was taken and the porosity distribution within the core was calculated by combining scans of the

dry- and water-saturated core (equation 10). An average porosity of 22% was obtained with minimal variations along the length of the core (Figure 3. 2).

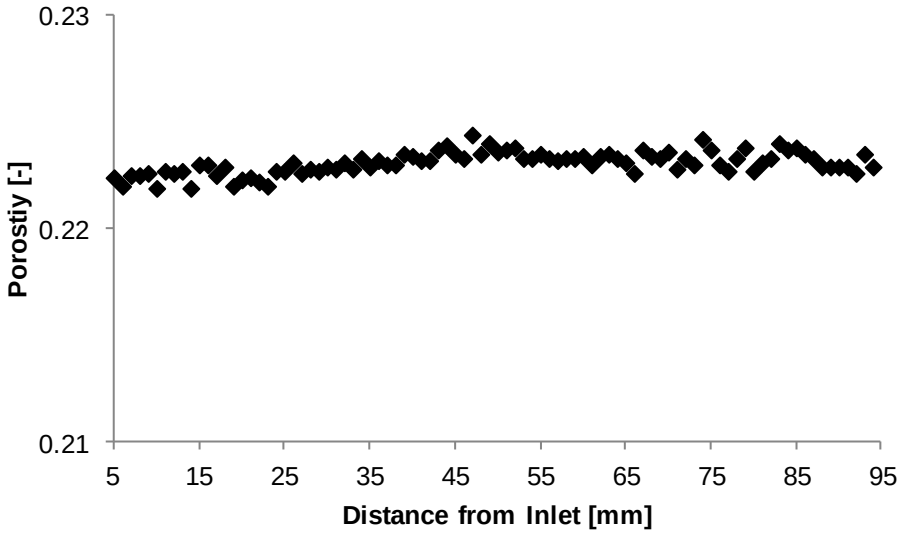

Figure 3. 2. Slice-averaged porosity along the core calculated from CT scans.

Absolute permeability measurement

Absolute permeability to water was calculated using pressure differences measured across the core for a series of ten flow rates (Figure 3. 3). At each flow rate, water was flushed until it reached a stable pressure drop across the core. A weighted linear regression (Meister, 2009) fit to this series of data provides an average ratio of pressure drops to flow rates used to calculate absolute permeability from Darcy's law. A total of three different permeability experiments were performed with this core (Table 3. 2). The results give an average absolute permeability of 931 mD, with an uncertainty of 18 mD, as obtained from the difference between the average and the maximum (or minimum) measured values.

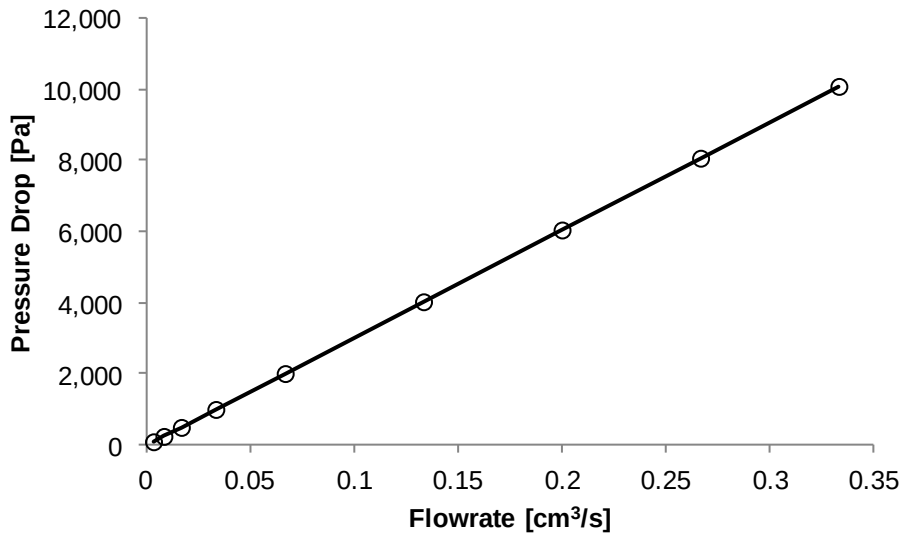

Figure 3. 3. Steady state measurements of pressure drop at varying flow rates in the water-saturated core. A fitted linear regression is used for calculations of absolute permeability.

Table 3. 2. Average absolute permeabilities (k) and standard deviations (σ_k) from average calculated for the same Berea core.

Experiment	***k*(mD)**
Krevor et al. (2012)	913
Previous unpublished experiment	949
This study	930
Representative average	931 +/-18

Experimental procedure

Once the background scans were acquired and absolute permeability measurements were completed, fluids were allowed to pre-equilibrate at 50 ºC outside the core holder overnight. Fluids were pre-equilibrated to ensure that flow was immiscible during core flooding. The core was then fully saturated with CO_2-saturated water and

incrementally pressurized to reservoir conditions at 9 MPa. Three cycles of drainage and imbibition were completed to collect saturation and relative permeability data. These cycles are referred to as A, B, and C in chronological order. The pre-equilibrated phases were injected simultaneously at a total flow rate of 20 ml/min beginning with a larger fractional flow of water than CO_2. Several fractional flows were chosen for each cycle in order to determine the relative permeability (Figure 3. 4, Table 3. 3). During drainage, fractional flow of CO_2 was increased between steps. During imbibition, fractional flow of CO_2 was decreased between steps. The second and third drainage cycles began from previous CO_2 residual saturations. This method differs from previous experiments where saturations were returned to initial conditions (S_w = 1) between drainage/imbibition cycling events (Akbarabadi and Piri, 2013).

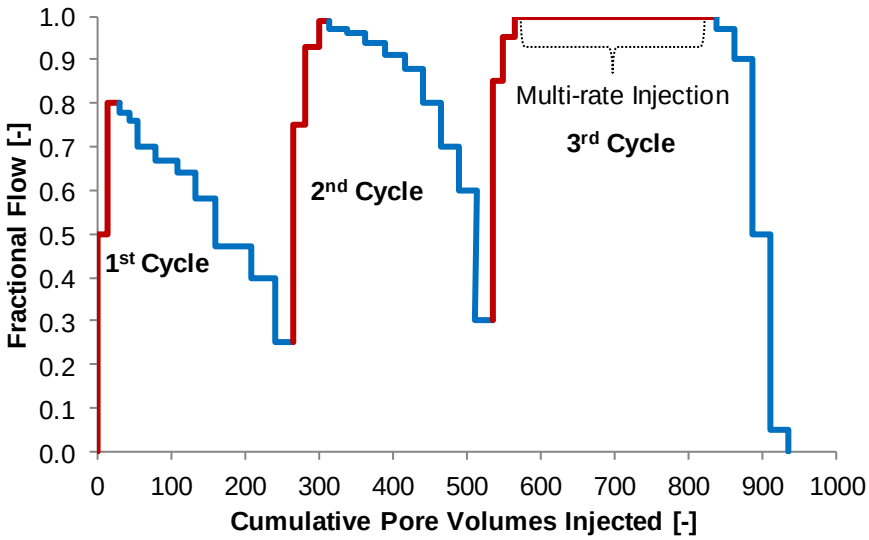

Figure 3. 4. CO_2 injection scheme. Red lines show wetting phase drainage (ff_{CO2} increase) and blue lines show wetting phase imbibition (ff_{CO2}decrease).

Table 3. 3. Fractional flows of CO_2 (ff_{CO_2}) used for drainage/imbibition cycles *A*, *B*, and *C* (*Dr.* is drainage, *Imb.* is imbibition). Pore volumes (V_p) flushed for each fractional flow. Total flow rate held at 20 ml/min for all fractional flows except 100% CO_2 injection steps. Cumulative pore volumes flushed at 100% CO_2 given. (*Dr.* is drainage, *Imb.* is imbibition).

Cycle A			Cycle B			Cycle C		
	ff_{CO_2}	V_p		ff_{CO_2}	V_p		ff_{CO_2}	V_p
Dr.	0.50	12.99		0.75	16.12		0.85	15.67
	0.80	14.78	***Dr.***	0.93	17.47		0.95	16.12
	0.78	13.43		0.99	14.33		0.995	23.73
	0.76	12.99		0.97	24.18	***Dr.***	ff_{CO_2} = 1.0 Q_{CO_2}[ml/min] = 20, 21, 22, 30, 31, 32, 40, 41, 42, 50, 51, 52 V_{ptot} = 272.75	
	0.70	23.73		0.96	24.63			
	0.67	28.66		0.94	27.76			
Imb.	0.64	24.63		0.91	25.97			
	0.58	28.66	***Imb.***	0.88	25.07			
	0.47	47.01		0.80	23.73		0.97	24.18
	0.40	33.13		0.70	23.73	***Imb.***	0.90	24.18
	0.25	25.07		0.60	24.18		0.50	25.07
				0.30	21.49		0.05	24.18

Equilibrated water was never injected at ff_w equal 1.0 during imbibition steps due to experimental difficulties at such conditions; instead small fractional flows of CO_2 were injected such that relative permeability was very low (<0.01). During the third cycle, ff_{CO2} was increased to 1.0 during drainage. Total flow rate was then incrementally increased from 20 ml/min in order to reach a maximum CO_2 saturation in the core. This method is further described by Pini and Benson (2013). The maximum flow rate was 50 ml/min while maintaining 100% CO_2 injection (Table 3. 3).

The pressure drop across the core in the water phase was measured once uniform saturation was reached as confirmed by the CT scans. A minimum of 10 pore volumes was required to pass through the core before taking a scan. Pressure readings were collected over the duration of the CT scan, in which time approximately 1.8 pore volumes of flow occurred. Measurements were smoothed using a moving average filter spanning 10 point subsets (Figure 3. 5, Table 3. 4). For each fractional flow, standard deviations of pressure drop were within 5% of the average pressure drop. Measurements were then used to calculate relative permeability from equation 9.

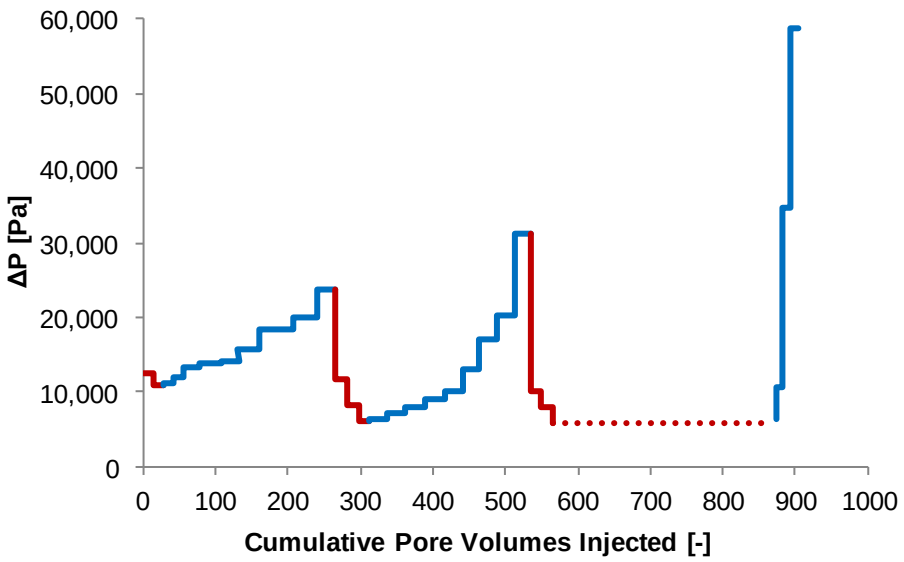

Figure 3. 5. Average pressure drop at steady-state for each fractional flow per pore volumes flushed through the core. Red lines show wetting phase drainage steps and blue lines show wetting phase imbibition steps. Dotted red region represents unknown pressure drop during 100% CO_2 injection.

Table 3. 4. Results by fractional flow of CO_2 for pressure drop (*ΔP*) across the core and standard deviation of pressure measurements (σ_p). Shown for drainage/imbibition cycles *A*, *B*, and *C*.

	Cycle A				Cycle B				Cycle C		
	ff_{CO_2}	*ΔP(Pa)*	σ_p *(Pa)*		ff_{CO_2}	*ΔP(Pa)*	σ_p *(Pa)*		ff_{CO_2}	*ΔP(Pa)*	σ_p *(Pa)*
Dr.	0.00	12,468	0.0	***Dr.***	0.75	11,745	179.73	***Dr.***	0.85	10,223	104.87
	0.50	10,875	250.61		0.93	8,371	118.00		0.95	7,878	111.14
	0.80	11,169	238.94		0.99	6,206	108.66		0.995	5,873	121.51
Imb.	0.78	11,896	316.23	***Imb.***	0.97	6,397	150.09		1.00	-	-
	0.76	13,348	186.11		0.96	7,081	163.83	***Imb.***	0.97	6,368	112.16
	0.70	13,809	225.99		0.94	7,847	90.53		0.90	10,708	204.16
	0.67	14,198	211.44		0.91	9,001	107.81		0.50	34,633	860.77
	0.64	15,748	523.52		0.88	10,106	241.15		0.05	58,829	425.50
	0.58	18,503	272.66		0.80	13,181	605.68				
	0.47	20,118	486.83		0.70	16,940	419.56				
	0.40	23,796	369.47		0.60	20,305	980.14				
	0.25	12,468	678.41		0.30	31,295	542.45				

An error analysis was performed to calculate a comprehensive range of relative permeability values (Appendix A). Error propagation calculations considered variance in absolute permeability measurements and variance in recorded pressure drops during relative permeability experiments. Results presented in Appendix A show these sources had little influence on final relative permeability values (Tables A-1 and A-2).

Results

CO_2 saturations

As higher CO_2 saturations are achieved during drainage steps, higher CO_2 saturations are trapped in pore space following imbibition steps (Figures 3. 6 and 3. 7). CO_2 saturation data show an essentially uniform distribution across the core (Figure 3. 6) confirming homogeneous porosity and permeability distribution and indicating negligible gravity effects (Figure 3. 7). These observations were needed to confirm the assumptions used in relative permeability calculations. Note that maximum observed saturations and relative permeabilities are limited by the capillary pressure that could be achieved in the experiment and may not represent endpoint values. Maximum core-averaged CO_2 saturations of 0.21, 0.39, and 0.51 were achieved during successive cycles, while minimum core-averaged saturations of 0.14, 0.20, and 0.25 were reached during imbibition (Figures 3. 6 and 3. 7, Table 3. 5). Drainage steps began at the phase saturations of the prior imbibition step, as opposed to recovering the system to 100% water saturation.

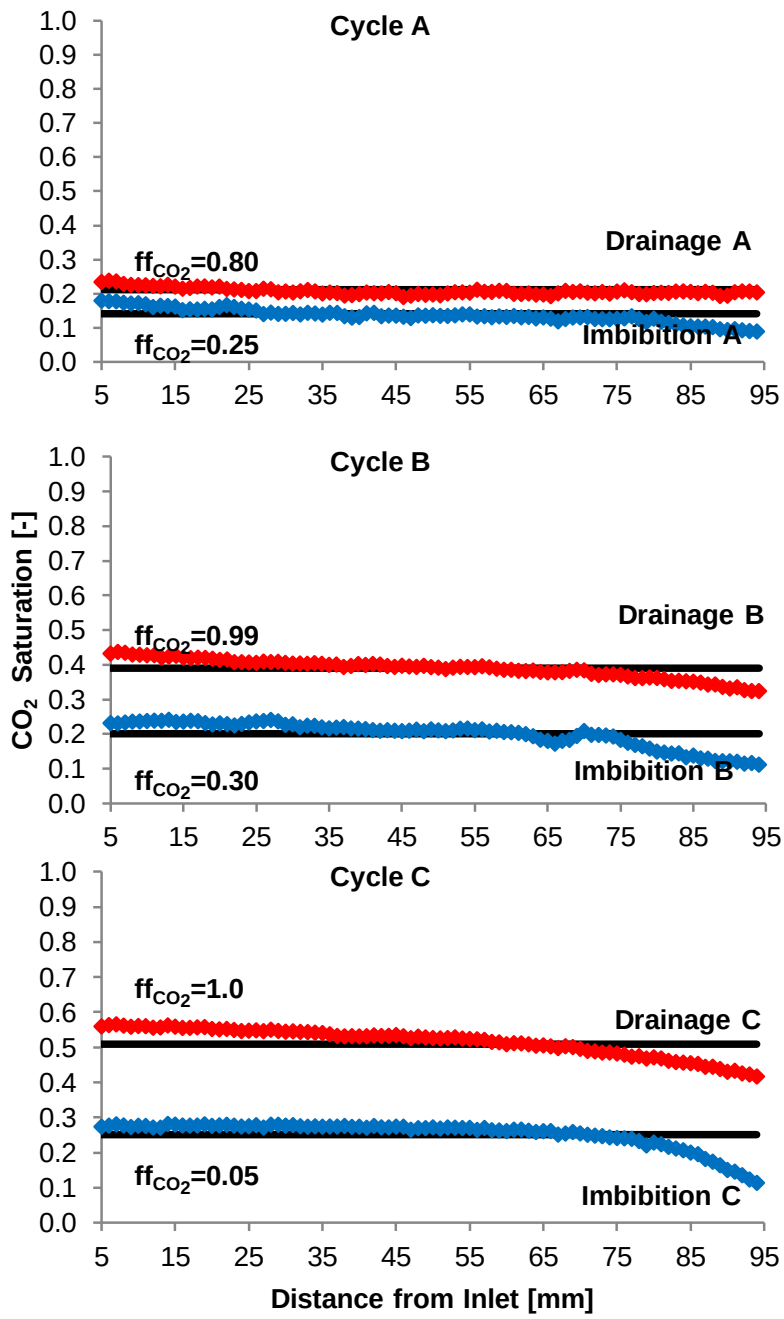

Figure 3. 6. Slice-averaged CO_2 saturation profiles. Measured across the core at steady state. Average saturation data for each slice is shown (red and blue points) as well as the core averaged value (black line). Red points are saturation data measured during the maximum CO_2 fractional flow of each cycle. Blue points are saturation data measured during the minimum CO_2 fractional flow of each cycle. Data were trimmed by 5 mm on either side to remove interference from the inlet and outlet ends of the core holder.

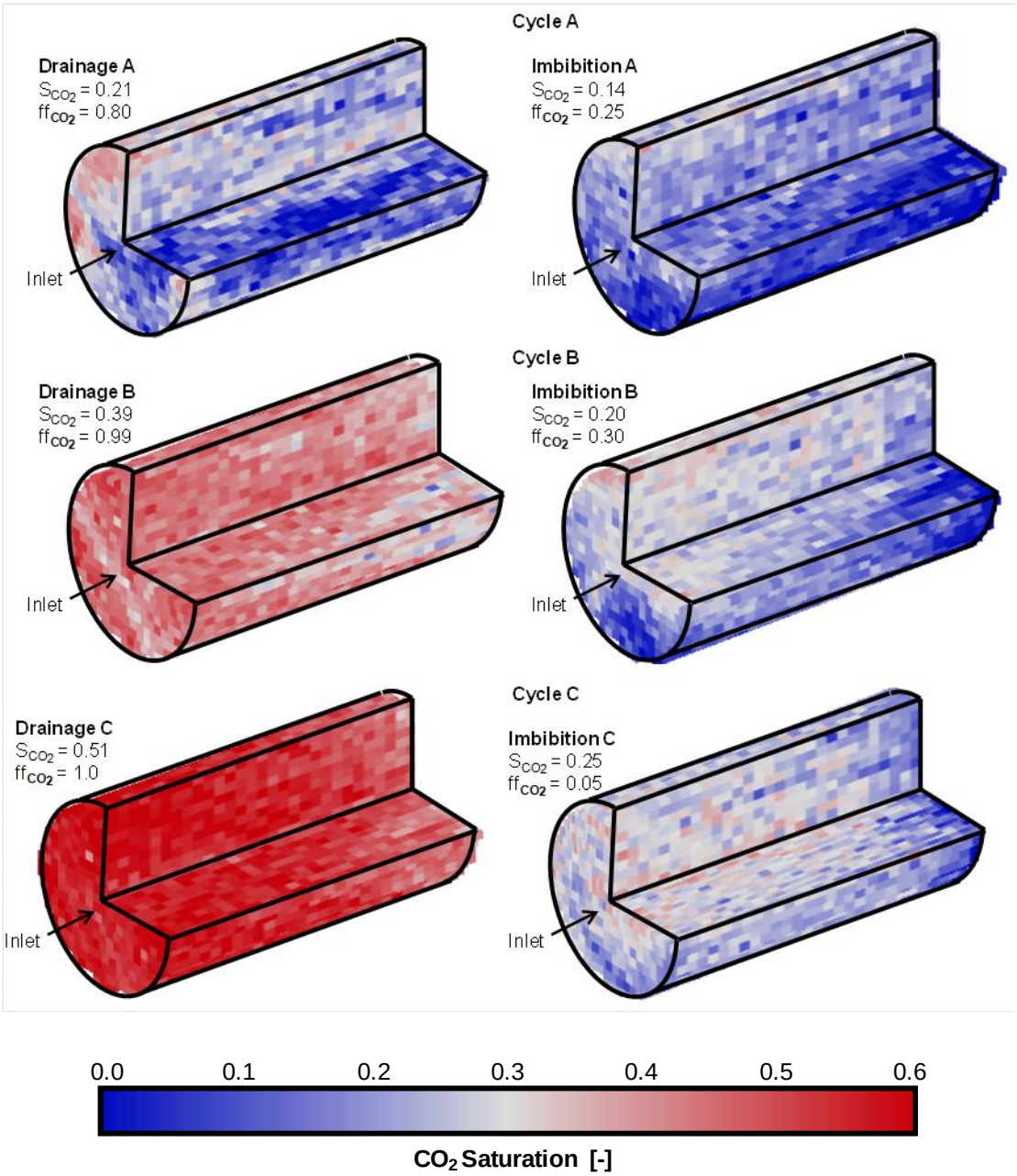

Figure 3. 7. CT scan of CO_2 distributions. Maximum and minimum recorded saturations per cycle at steady state. Core average saturations given. Data was trimmed to remove inlet and outlet of the core holder by 5 mm on either side. Colorbar maximum S_{CO2} = 0.6 to reflect the maximum achievable saturations in these core floods.

Carbon dioxide fractional flow versus the CO_2 saturation data show a steep fractional flow curve, with ff_{CO2} near 1.0 reached at relatively low CO_2 saturations (0.3-0.4) (Figure 3. 8). This is due to a large viscosity contrast between fluids. During water imbibition, ff_{CO2} to CO_2 saturation decreases sharply, which results in the trapping of CO_2 at higher saturations. Trends in fractional flow behavior were used to estimate residual saturations where fractional flow equals zero.

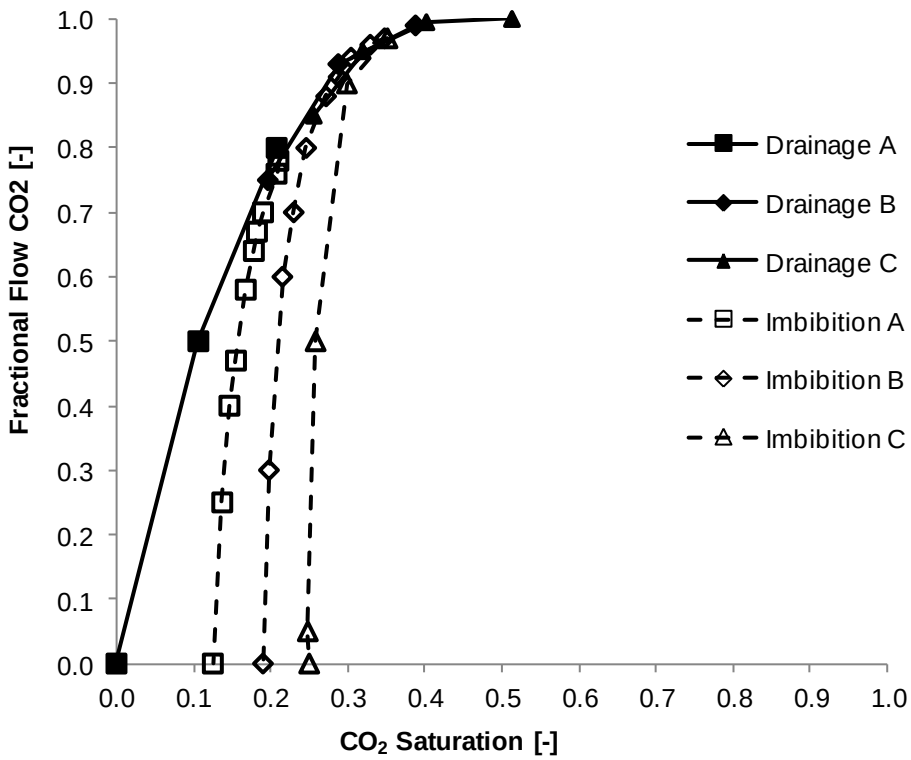

Figure 3. 8. CO_2 phase fractional flow versus saturation plot. Solid line follows wetting phase drainage path for all cases, dash lines represent wetting phase imbibition paths for cycle A, B, and C. Estimated residual saturations are extrapolated and plotted with data at fractional flows equal zero.

Relative permeability measurements

Carbon dioxide relative permeability data exhibit strong hysteresis, while water relative permeability data follow a non-hysteretic curve (Figure 3. 9). Core-averaged CO_2 relative permeability data from this experiment fall on a single bounding primary drainage curve and three imbibition scanning curves, the latter representing the three cycles (Figure 3. 10). Drainage data in both phases match previous measurements taken under similar pressure/temperature conditions from the same Berea core by Krevor et al. (2012). Maximum calculated CO_2 relative permeability was achieved during cycle C at 0.357 (Table 3. 5) and was obtained upon application of the technique described in Pini and Benson (2013), which uses observations from 100% $scCO_2$ drainage experiments at increasingly higher flow rates. CO_2 saturations approach three distinct residually trapped saturations as imbibition relative permeability values approach zero.

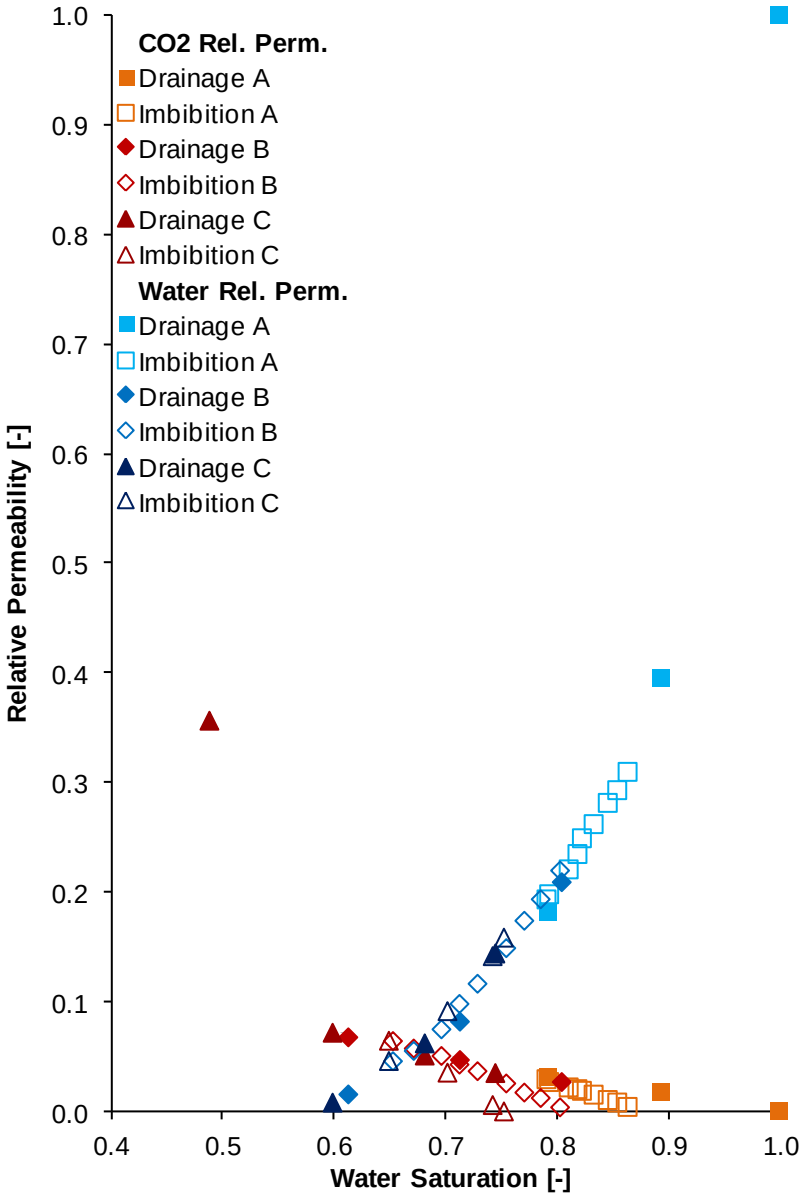

Figure 3. 9. Core-average relative permeability measurements as a function of water saturation.

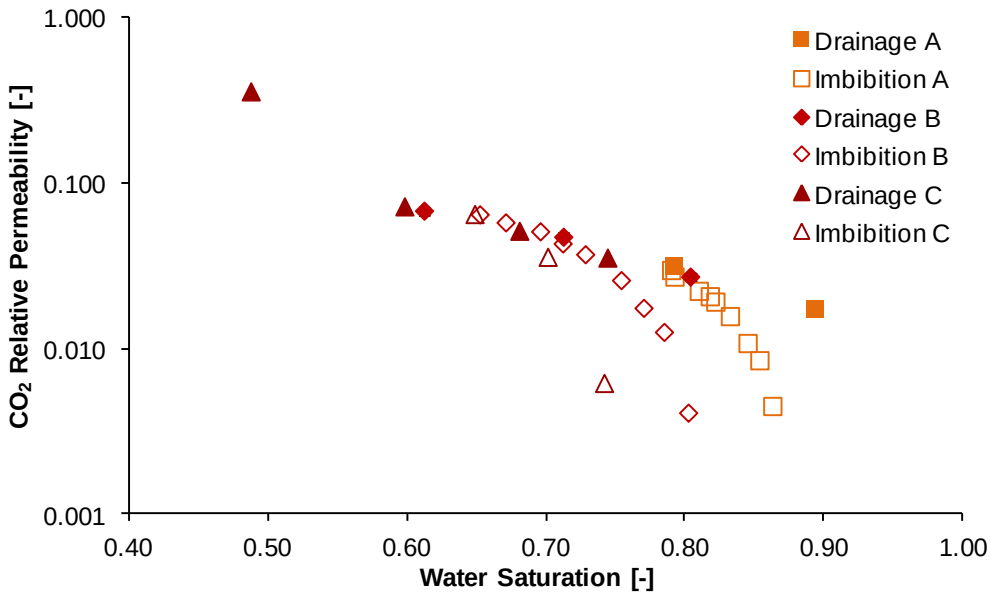

Figure 3. 10. Hysteresis in CO_2 relative permeability measurements.

Table 3. 5. Results by fractional flow of CO_2 for core average water saturation and relative permeability data. Shown for drainage/imbibition cycles *A*, *B*, and *C*.

	Cycle A					Cycle B					Cycle C			
	ff_{CO_2}	S_w	k_{rCO_2}	k_{rw}		ff_{CO_2}	S_w	k_{rCO_2}	k_{rw}		ff_{CO_2}	S_w	k_{rCO_2}	k_{rw}
	0.00	1.00	0.000	1.000		0.75	0.80	0.027	0.215		0.85	0.74	0.035	0.148
Dr.	0.50	0.89	0.017	0.405	***Dr.***	0.93	0.71	0.047	0.084	***Dr.***	0.95	0.68	0.051	0.064
	0.80	0.79	0.031	0.186		0.99	0.61	0.068	0.016		0.995	0.60	0.072	0.009
	0.78	0.79	0.030	0.199		0.97	0.65	0.065	0.047		1.00	0.49	0.357	0.000
	0.76	0.79	0.027	0.204		0.96	0.67	0.058	0.057		0.97	0.65	0.065	0.048
	0.70	0.81	0.022	0.227		0.94	0.70	0.051	0.077	***Imb.***	0.90	0.70	0.036	0.094
	0.67	0.82	0.021	0.241		0.91	0.71	0.043	0.101		0.50	0.74	0.006	0.146
Imb.	0.64	0.82	0.019	0.256	***Imb.***	0.88	0.73	0.037	0.120		0.05	0.75	0.000	0.163
	0.58	0.82	0.016	0.269		0.80	0.75	0.026	0.153					
	0.47	0.85	0.011	0.289		0.70	0.77	0.018	0.179					
	0.40	0.85	0.009	0.301		0.60	0.79	0.013	0.199					
	0.25	0.86	0.005	0.318		0.30	0.80	0.004	0.226					

Water relative permeabilities follow one bounding primary drainage and imbibition curve (Figure 3. 11). Water was initially at maximum relative permeability of 1.0. The lowest recorded water relative permeability was during cycle *C*, reaching 0.009 at 60% water saturation. Following full CO_2 injection during drainage cycle *C*, the Pini and Benson (2013) method was used to calculate maximum CO_2 relative permeability at 0.357 and water saturation 49%.

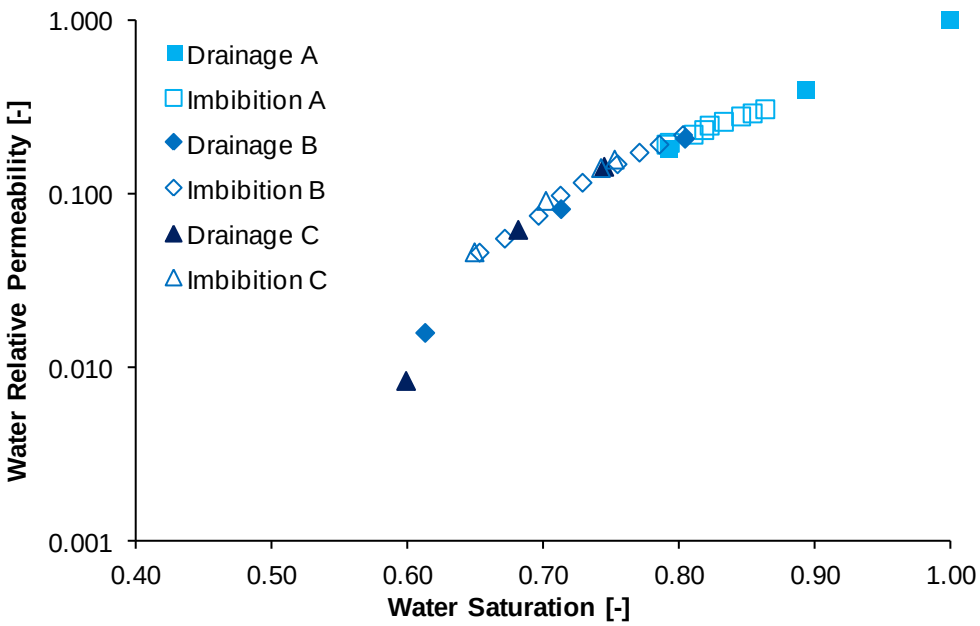

Figure 3. 11. Nonhysteretic water relative permeability measurements.

Residual trapping

Trapped residual CO_2 saturation was found to increase for each increase in turning point saturation. Residual CO_2 saturations were ultimately determined by relative permeability imbibition scanning data extrapolated to $k_{rCO_2}= 0$ (Figures 3. 9 and 3. 10). Residually trapped CO_2 saturations were calculated at 0.13, 0.19, and 0.25 for cycles A,

B, and C respectively. Trapping data are consistent with published results from studies of CO_2/brine and CO_2/water systems at reservoir conditions (Figure 3. 12) (Pentland et al., 2011; Krevor et al., 2012). The maximum and residual observed CO_2 saturations from Krevor et al. (2012) were implemented into the fitted data set as they were observed from the same core under the same conditions. Experimental data were fit by linear and Land trapping models. The linear trapping model provides the best fit to data when $f_r = 0.5$ (equation 2) at an R^2 value of 0. 978. The Land model with *Land C* = 1.9 provides an R^2 value of 0.937 (equation 1). Linear nonwetting phase trapping behavior has also been observed by Aissaoui (1983), Kleppe et al. (1997), Suzanne et al. (2003), Johnson and Adamski (2005), and Pentland et al. (2010).

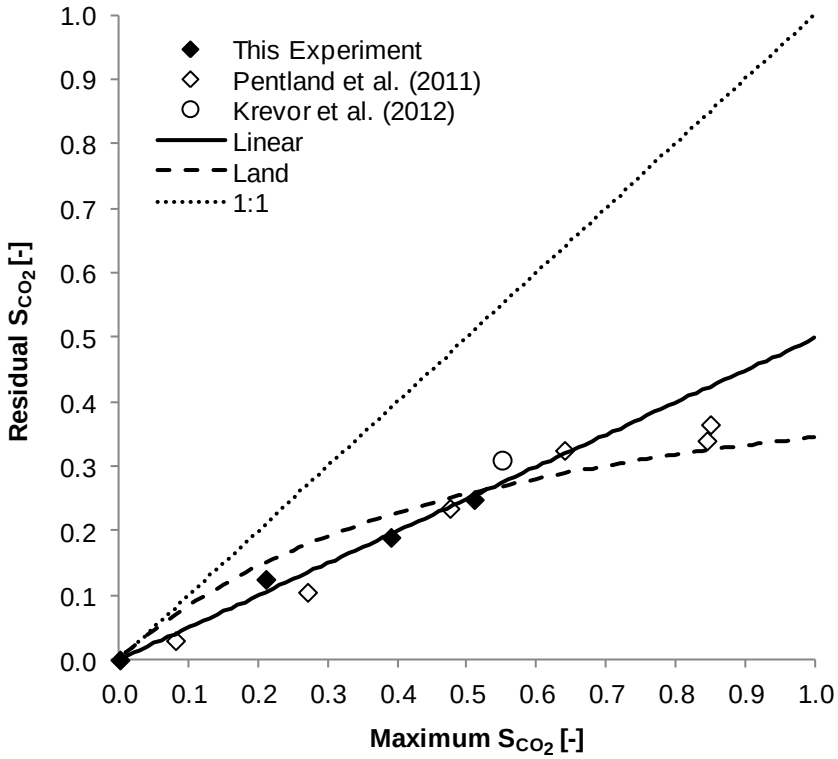

Figure 3. 12. Residual saturation as a function of the maximum, or turning point, saturations per

cycle for core-averaged data. Core-averaged trapping data from previous CO_2/brine (Pentland et al., 2011) and CO_2/water (Krevor et al., 2012) experiments on Berea sandstone are shown for comparison. Linear (Kleppe et al, 1997) and Land (1968) trapping curves are fit to data. One-to-one line is shown as complete trapping bound.

Discussion

Experimental results provide insight into multi-phase fluid behavior by defining relative permeability functions that may be applied to larger scale CO_2 storage applications to predict the mobility of CO_2 plumes over time. Experimental data were fit by each of the common capillary- pressure-based relative permeability models from Table 3. 1. The best fit was provided by Van Genuchten-Burdine models for both nonhysteretic wetting relative permeability and hysteretic nonwetting relative permeability (Figure 3. 13). These models also fit previous experimental results from Krevor et al. (2012) (Figure 3. 13).

A couple of comments are worth making with respect to the hysteretic models chosen. First, continuously updating the value of S_{nr} results in an alteration of the shape of the bounding primary drainage curve compared to traditional non-hysteretic approaches. As a result, the fitting parameters (e.g. tortuosity term C, Van Genuchten m, and Brooks and Corey λ) had to be slightly modified in order to match the bounding primary drainage curves. Second, when applied to numerical simulations, the use of equation 4 with a continuous update of S_{nr} leads to relative permeability curves that are smooth and continuously differentiable thus providing good numerical performance (Patterson and Falta, 2012).

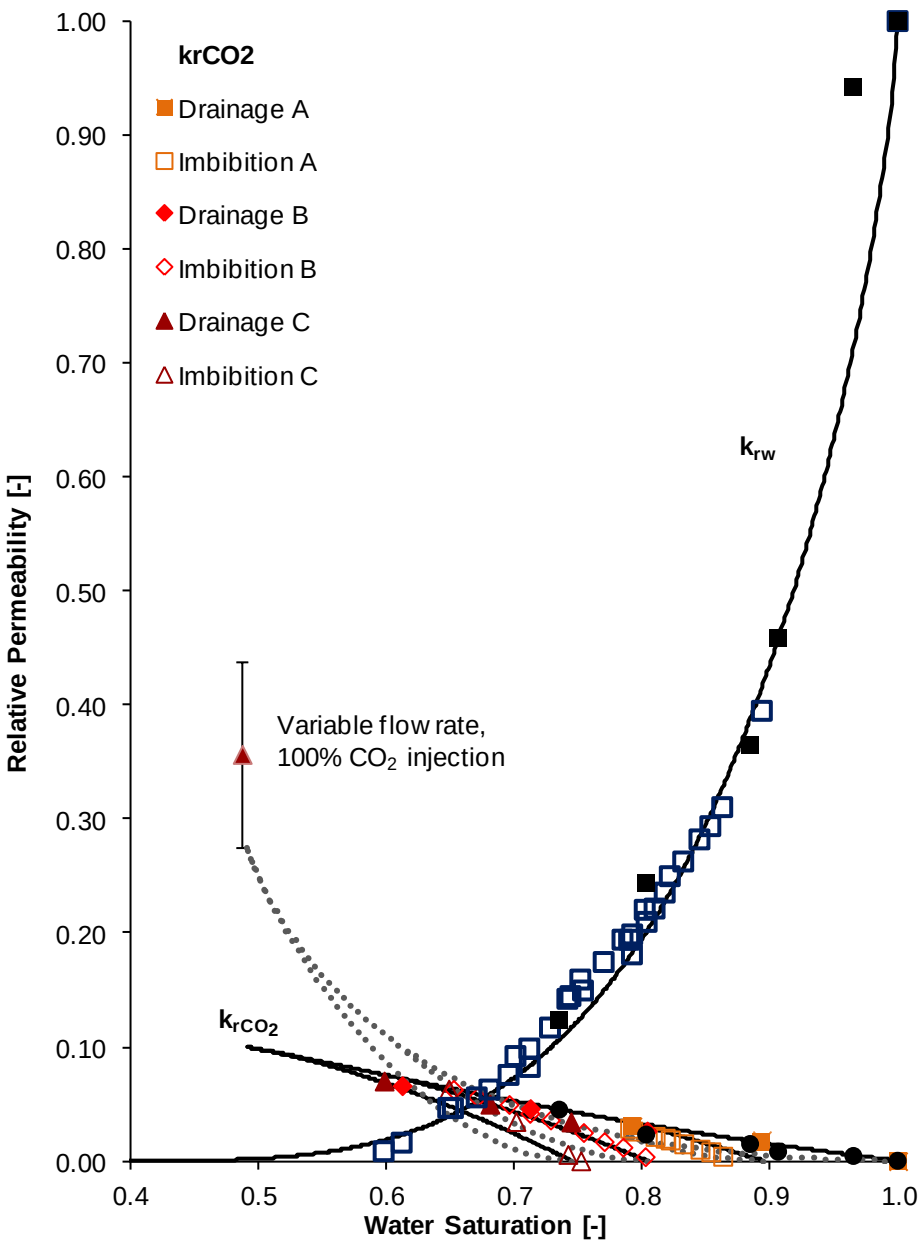

Figure 3. 13. Van Genuchten-Burdine models fit to nonhysteretic water relative permeability data and scaled hysteretic CO_2 relative permeability data - the solid lines represent the experimental end point extrapolated from data and the dotted lines represent the experimental end point calculated by the Pini and Benson (2013) method. Blue squares include all water relative permeability data, drainage and imbibition. Fitting parameters given in Tables 3. 7 and 3. 8.

Water relative permeability was best fit using a nonhysteretic model, with tortuosity term C = 0.5 and Van Genuchten m = 1.62. Carbon dioxide relative permeability curves were best fit by employing the linear trapping model in a scaled Van Genuchten-Burdine model. The residual CO_2 saturation was calculated as a linear function of f_r = 0.5. Two fits were made; the first used the Pini and Benson (2013) method to estimate a maximum experimental k_{rCO2} based on variable flow rates at 100% CO_2 injection and the second used only the data measured during the constant flow rate injection. All models used a residual water saturation of 0.49 as the experimental minimum.

The first model fit was scaled by the maximum experimental k_{rCO_2} calculated at 0.357; it should be noted that this is not representative of the final relative permeability end point. The tortuosity term was fit by C = 0.5 and the Van Genuchten parameter was m = 1.25. The second model fit was scaled by a maximum experimental k_{rCO_2} extrapolated to 0.10. This extrapolation was based on the model parameters that best fit the constant flow rate data. The tortuosity term was fit by C = 0.5 and the Van Genuchten parameter was m = 0. 50. A comparison of best fit parameters for each of the four models and both methods of addressing the maximum k_{rCO_2} is given in Tables 3. 6 and 3. 7. All resultant curves produced good fits to unweighted k_{rCO_2} data, but demonstrate different behavior at the experimental end point. Including the maximum k_{rCO_2} calculated from the Pini and Benson (2013) method shows a concave upwards trend; excluding this point and

extrapolating to the maximum k_{rCO_2} results in a concave downwards trend and a better fit to the data.

Table 3. 6. Unweighted best fit comparison between common hysteretic nonwetting relative permeability functions. Fits to experimental end point calculated by the Pini Benson (2013) method shown in parenthesis.

Model	***C***	***VG, m***	***BC, λ***	R^2
Brooks and Corey - Burdine	1.15 (1.0)	-	0.46 (3.0)	0.87 (0.82)
Brooks and Corey - Mualem	0.60 (0.93)	-	0.50 (2.0)	0.91 (0.84)
Van Genuchten - Burdine	0.5 (0.5)	0.50 (1.25)	-	0.92 (0.88)
Van Genuchten - Mualem	0.5 (0.4)	0.35 (0.88)	-	0.92 (0.86)

Table 3. 7. Unweighted best fit comparison between common wetting relative permeability functions.

Model	***C***	***VG, m***	***BC, λ***	R^2
Brooks and Corey - Burdine	2.76	-	3.5	0.965
Brooks and Corey - Mualem	2.15	-	2.10	0.955
Van Genuchten - Burdine	0.5	1.62	-	0.997
Van Genuchten - Mualem	0.5	0.85	-	0.985

For comparison, the procedure outlined in section 2 was followed to characterize the trapping relationship and CO_2 relative permeability curve from data collected by Akbarabadi and Piri (2013). Land and linear models both provided excellent fits to trapping data, with R^2 = 0.99 and 0.98 respectively (Figure 3. 14). The Van Genuchten-Burdine model was again successfully fit to data, this time using the Land trapping relationship (Figure 3. 15). Results showed a higher proportion of CO_2 trapping, near

78% each cycle, and a consistently higher CO_2 relative permeability to water saturation than our experimental results. Despite these differences, the resultant curves behave similarly to those fit only by our constant flow rate data; demonstrating a concave downward trend at the experimental end point. These results demonstrate the need to improve experimental techniques used to measure the nonwetting phase relative permeability end point in the case of fluid pairs with strong viscosity contrast. In the case that there is a sharp increase in CO_2 relative permeability as the end point is approached, as determined by the Pini and Benson (2013) method, models may need to be modified to fit this inflection towards the end point.

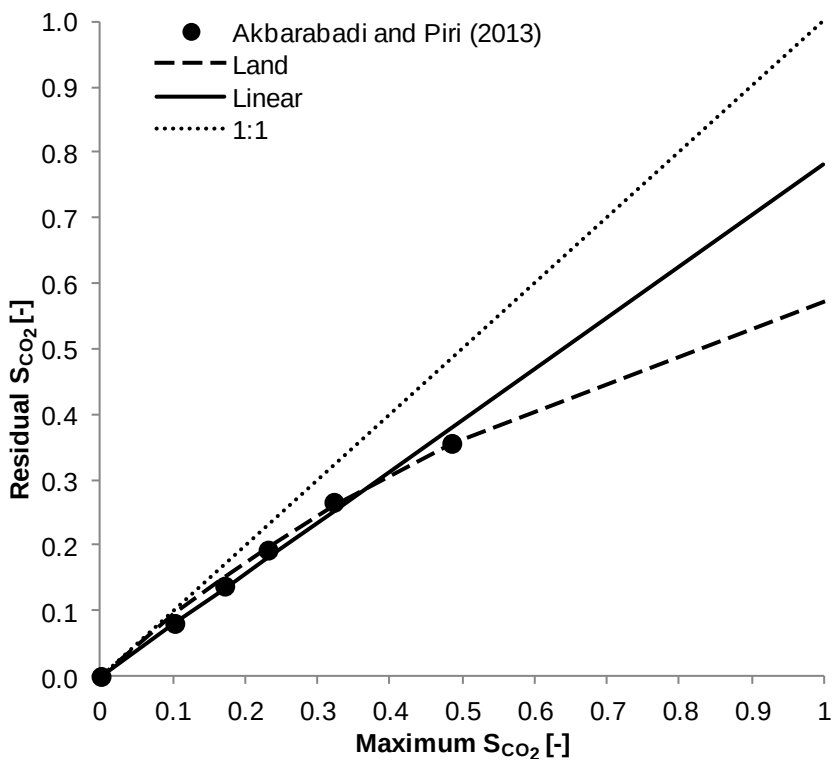

Figure 3. 14. Residual saturation as a function of the maximum, or turning point, saturations per cycle for core-averaged data. Core-averaged trapping data from Akbarabadi and Piri (2013). Linear (Kleppe et al, 1997) and Land (1968) trapping curves are fit to data. The linear fraction is

fit to 0.78 and the Land C is fit to 0.75. One-to-one line is shown as complete trapping bound.

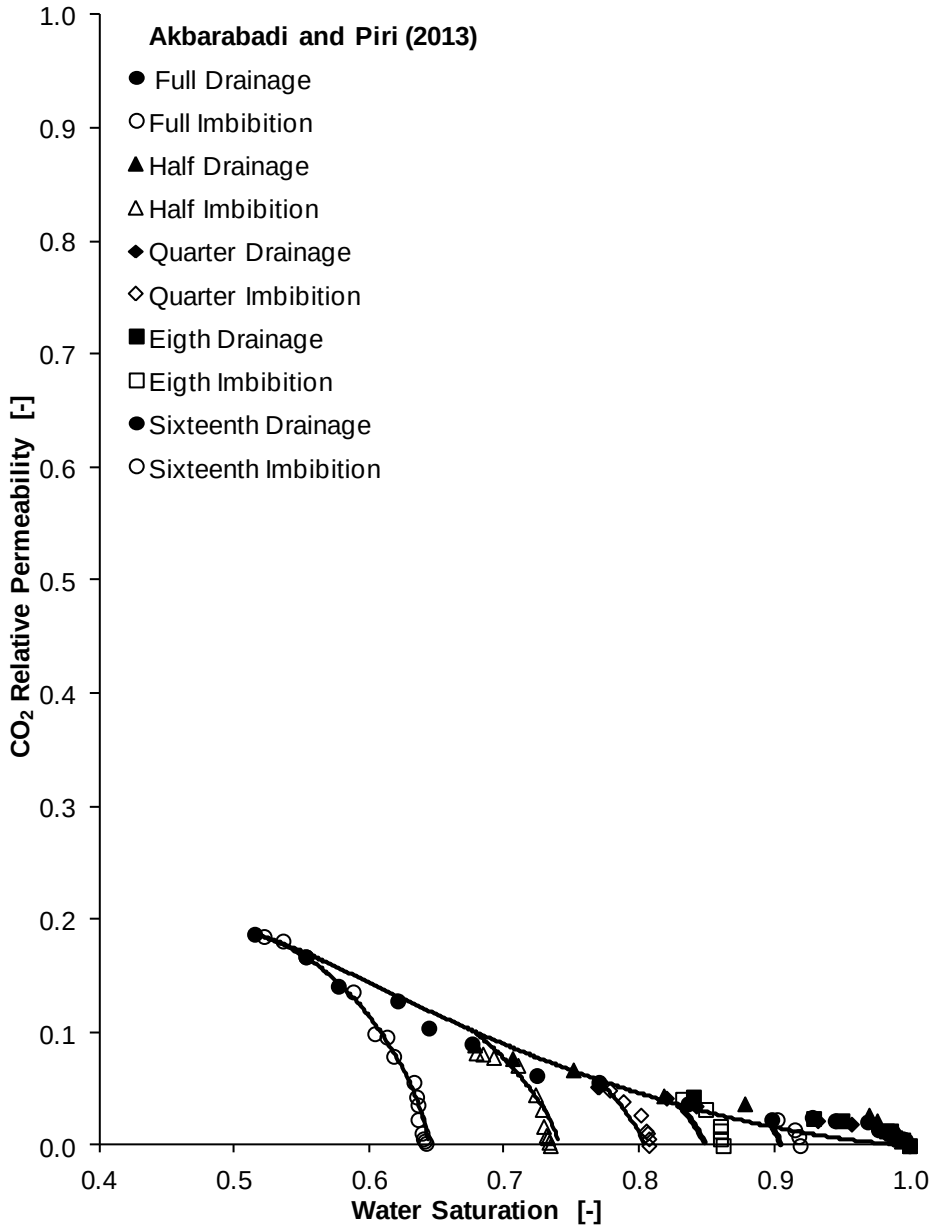

Figure 3. 15. Van Genuchten-Burdine model fit to scaled hysteretic CO_2 relative permeability data from Akbarabadi and Piri (2013). Van Genuchten m = 0.45, Swr = 0.52, krmax = 0.19, tortuosity C = 0.25. The Land trapping model was incorporated to provide hysteretic effects, Land C= 0.75.

With relevance to the hysteretic character of the relative permeability curve, it has been observed that a small portion of the drainage curve is retraced before a unique imbibition curve can be identified (Naar et al., 1962). Interestingly, this behavior was observed in this experimental study as well as the Akbarabadi and Piri (2013) study (Figures 3. 14 and 3. 15). The reason for this phenomenon can be traced back to the particular geometry and topology of the pore space, as studies on glass micro-models have shown that a small pore-to-throat ratio might lead to dynamics of multiphase flow that are completely reversible (Wardlaw, 1980). Regardless of the actual mechanism, this example further highlights the need for more experimental observations of the $scCO_2$ /water system in different rock types at conditions relevant to geologic carbon sequestration, as this phenomenon could significantly affect the amount of CO_2 that can be immobilized by residual trapping within a storage formation and eventually play a large role in the long term security of a storage project.

Conclusions

Saturation and relative permeability data were collected for a $scCO_2$/water system using the steady state method at PT conditions typical of CO_2 storage. Three core flooding cycles were completed by incrementally increasing and decreasing the fraction of CO_2 to water while maintaining a constant total volumetric flow rate. Carbon dioxide fractional flows were chosen such that the turning point saturation of CO_2, as measured by a CT scanner, was increased each cycle.

Results show strong residual trapping dependence on the saturation history of the core for the nonwetting CO_2 phase. The trapped CO_2 saturation was consistent with previous findings and fits a linear relationship to the turning point saturation (maximum CO_2 saturation). A linear trapping model previously developed for applications in multiphase contaminant transport was fit to data with a value of 0.5 describing the relationship between the turning point CO_2 saturations and the residual CO_2 saturations of each respective cycle.

Water relative permeability exhibited nonhysteretic behavior while CO_2 relative permeability exhibited hysteresis due to trapping during imbibition events. Van Genuchten-Burdine models were shown to fit both sets of data after incorporating a linear trapping model into nonwetting phase calculations. Additionally, Van Genuchten-Burdine models were shown to fit relative permeability data collected for a $scCO_2$/water system in a different Berea core after incorporating the Land trapping model (Akbarabadi and Piri, 2013). Results demonstrated the need to improve experimental techniques to measure end point relative permeability in the case of fluid pairs with strong viscosity contrast.

Predictions of the distribution and storage of injected CO_2 are dependent on the residual gas trapping and relative permeability behavior. These experimental results may be useful in modifying existing multiphase codes to be more suitable for CO_2 storage applications. In this case, existing models were shown to fit experimental data for

constant flow rate experiments, but future models may need to be modified to fit relative permeability behavior as kr_{CO2} approaches the end point.

Works Cited

Aissaoui A., 1983. Etude théorique et expérimentale de l'hystérésis des pressions capillaires et desperméabilités relatives en vue du stockage souterrain de gaz. PhD thesis, Ecole des Mines de Paris. Paris, France.

Akbarabadi, M., Piri, M., 2013. Relative permeability hysteresis and capillary trapping characteristic of supercritical CO_2/brine systems: An experimental study at reservoir conditions. Adv. Water Resour. 52, 190-206.

Akin, S., Kovscek, A.R., 2003. Computed tomography in petroleum engineering research. Applications of X-Ray Computed Tomography in the Geosciences. The Geological Society of London, London. 215(1), 23–38.

Brooks, R. H., Corey, A. T., 1964. "Hydraulic properties of porous media." Hydrology paper No. 3, Colorado State Univ., Fort Collins.

Burdine, N.T., 1953. Relative permeability calculations from pore size distribution data. Trans. AIME. 198, 71-78.

Carlson, F.M., 1981. Simulation of relative permeability hysteresis to the nonwetting phase. SPE 10157, presented at the 57th annual Technical Conference and Exhibition, San Antonio, 5-7 October.

Churcher, P.L., French, P.R., Shaw, J.C., Schramm, L.L., 1991. Rock Properties of Berea Sandstone, Baker Dolomite, and Indiana Limestone. Publication SPE 21044.

Proceedings of the 1991 SPE International Symposium on Oilfield Chemistry. Anaheim, California, USA. 20-22 February.

Doughty, C., 2007. Modeling geologic storage of carbon dioxide: Comparison of non-hysteretic and hysteretic characteristic curves. Energ Convers Manage. 8, 1768–1781.

Dullien, F. A. L., 1979. Porous media fluid transport and pore structure. New York: Academic Press.

Dury, O., Fischer, U., and Schulin, R., 1999. A comparison of relative nonwetting-phase permeability models. Water Resour. Res. 35(5), 1481-1493.

Fatt, I., Klikoff, W.A., 1959. Effect of Fractional Wettability on Multiphase Flow Through Porous Media. AIME Transactions, 216-246.

Fagerlund, F., Niemi, A. , Illangasekare, T.H., 2008. Modeling of nonaqueous phase liquid (NAPL) migration in heterogeneous saturated media: Effects of hysteresis and fluid immobility in constitutive relations. Water Resour. Res. 44(3).

Hesse, M.A., Tchelepi, H.A., Cantwell, B.J., Orr Jr., F.M., 2007. Gravity currents in horizontal porous layers: transition from early to late self-similarity. J. Fluid Mech. 577, 363–383.

Intergovernmental Panel on Clim. Change (IPCC), 2005. Underground geologic storage: IPCC special report on carbon dioxide capture and storage, Chap. 5. Cambridge University Press, New York.

Jerauld, G.R., 1997. Prudhoe Bay gas/oil relative permeability. SPE Reservoir Eng. 12, 66–73.

Johnston, C., Adamski, M., 2005. Relationship between initial and residual LNAPL saturation for different soil types. Proceedings of the 2005 Petroleum Hydrocarbons and Organic Chemicals in Groundwater®: Prevention, Assessment, and Remediation Conference. 17-19 August, Costa Mesa, 29-42.

Juanes, R., Spiteri, E.J., Orr, F.M., Blunt, M.J., 2006. Impact of relative permeability hysteresis on geological CO_2 storage. Water Resour. Res. 42(12).

Lemmon, E.W., McLinden, M.O., Friend, D.G., 2011. Thermophysical properties of fluid systems. NIST chemistry WebBook. NIST Standard Reference Database Number 69. Eds. P.J. Linstrom and W.G. Mallard, National Institute of Standards and Technology, Gaithersburg MD.

Lenhard, R.J., Parker, J.C., 1987. A model for hysteretic constitutive relations governing multiphase flow: 2. Permeability-saturation relations, Water Resour. Res. 23(10), 2197-2206.

Luckner, L., Van Genuchten, M.T., Nielson, D.R., 1989. A consistent set of parametric models for the two-phase flow of immiscible fluids in the subsurface.Water Resour. Res. 25(10), 2187-2193

Kaluarachchi, J.J., Parker, J.C., 1992. Multiphase flow with a simplified model for oil entrapment. Transport Porous Med, 7(1), 1-14.

Killough, J.E., 1976. Reservoir simulation with history-dependent saturation functions. SPEJ 16(1), 37-48.

Kleppe, J., Delaplace P., Lenormand R., Hamon, G., Chaput, E., 1997. Representation of Capillary Pressure Hysteresis in Reservoir Simulation. Publication SPE 38899. Proceedings of the SPE annual Technical Conference and Exhibition, San Antionio, Texas, USA, 5-8 October.

Krevor, S. C. M., Pini, R., Zuo, L., Benson, S. M., 2012. Relative permeability and trapping of CO_2 and water in sandstone rocks at reservoir conditions. Water Resour. Res. 48.

Ku, H. H., 1966. Notes on the use of propagation of error formulas. J. Res. Natl. Bur. Stand. 70C(4), 263-273.

Lake, L. W., 1989. Enhanced Oil Recovery. NJ: Prentice Hall.

Land, C.S., 1968. Calculation of imbibition relative permeability for two- and three-phase flow from rock properties. SPEJ 8, 149–156.

Meister, A., 2009. Deconvolution problems in nonparametric statistics. Vol. 193. New York: Springer.

Mualem, Y., 1976. A new model for predicting the hydraulic conductivity of unsaturated porous media. Water Resour. Res. 12(3), 513-522.

Naar, J., Wygal, R., Henderson, J., 1962. Imbibition relative permeability in unconsolidated porous media. SPEJ 2, 12-17.

Niemi, A., Bodvarsson, G.S., 1988. Preliminary capillary hysteresis simulations in fractured rocks, Yucca Mountain, Nevada. J. Contam. Hydrol. 3, 277- 291.

Parker, J.C., Lenhard, R.J., 1987. A parametric model for constitutive properties governing multiphase flow in porous media. Water Resour. Res. 23(4), 618-624.

Patterson, C., Falta, R.W., 2012. A simple history-dependent nonwetting phase trapping model for the TOUGH simulations. Proceedings of the TOUGH Symposium 2012. Lawrence Berkeley National Laboratory, Berkeley, California. 17-19 September.

Pentland, C. H., Itsekiri E., Al-Mansoori S., Iglauer S., Bijeljic B., Blunt M. J., 2010. Measurement of Nonwetting Phase Trapping in Sandpacks, SPEJ, 15(2), 274-281.

Pentland, C.H., El-Maghraby, R., Iglauer, S., Blunt, M., 2011. Measurements of the capillary trapping of supercritical carbon dioxide in Berea sandstone. Geophys. Res. Lett. 38, L06401.

Perrin, J.C., Benson, S., 2009. An experimental study on the influence of sub-core scale heterogeneities on CO_2 distribution in reservoir rocks. Transport Porous Med. 82(1), 93–109.

Pini, R., Benson, S., 2013. Simultaneous determination of capillary pressure and relative permeability curves from core-flooding experiments with various fluid pairs. Water Resour. Res. 49(6), 3516-3530.

Pope, G.A., 1980. The application of fractional flow theory to enhanced oil recovery. SPEJ 20(3), 191-205.

Spiteri, E. J., Juanes, R., Blunt, M.J., Orr, F.M., 2008. A new model of trapping and relative permeability hysteresis for all wettability characteristics. SPEJ. 13(3), 277–288.

Steffy, D.A., Barry, D.A. Johnston, C.D., 1997. Influence of antecedent moisture content on residual LNAPL saturation. J. Soil Contam. 6, 113-147.

Suzanne, K., Hammon, G., Billiotte, J., Trocme,V., 2003. Experimental relationships between residual gas saturation and initial gas saturation in heterogeneous sandstone reservoirs. Paper SPE 84038 presented at the SPE Annual Technical Conference and Exhibition. Denver, CO, 5-8 October.

Qi, R., LaForce, T.C., Blunt, M.J. 2009. Design of carbon dioxide storage in aquifers. Int. J. Greenh. Gas Control. 3(2), 195‑205.

Van Genuchten, M.T., 1980. A closed-form equation for predicting the hydraulic conductivity of unsaturated soils, Soil Sci. Soc. Am. J. 44, 892-898.

Wardlaw, N.C., 1980. The effects of pore structure on displacement efficiency in reservoir rocks and in glass micromodels. SPE/DOE Enhanced Oil Recovery Symposium. Society of Petroleum Engineers.

CHAPTER FOUR:

COST EFFECTIVE CO_2 STORAGE DESIGN TO ENHANCE SECONDARY GAS TRAPPING

Introduction

The goal of geologic carbon storage (GCS) is to safely store industrially produced CO_2 deep in the subsurface. Minimizing the amount of mobile CO_2 in storage formations reduces risks associated with leakage and may reduce overall GCS costs (Keith et al., 2005; Ide et al., 2007; Leonenko and Keith, 2008; IEAGHG, 2010; Zhang and Agarwal, 2012, 2013, 2014). Water/CO_2 co-injection strategies aim to achieve this goal by injecting saline water or brine following, alternating, or simultaneously with CO_2 injection (IEAGHG, 2010). Co-injection strategies are intended to increase the rate of CO_2 immobilization over standard supercritical CO_2 (scCO_2) injection by enhancing secondary gas trapping mechanisms (IEAGHG, 2010). For these injection strategies, secondary gas trapping mechanisms primarily refer to residual gas trapping (capillary trapping) and dissolution of CO_2.

Studies have been done to quantify costs of the separate elements of carbon capture and storage based on standard scCO_2 injection, breaking down projects based on capture costs, transportation costs, storage costs, monitoring costs, and financial responsibility (Rubin et al., 2007; Benson et al., 2004; EPA, 2010a, 2010b, 2011). The most expensive component is always CO_2 capture, representing ~73% of total costs at \$42-83/tCO_2 captured (Rubin et al., 2007). Transportation costs vary with pipeline

dimension, pressure of CO_2, and landscape, ranging from \$1–9/tCO_2 transported per 100 km of pipeline (Pires, et al., 2011). Storage costs depend on the formation class; for deep saline aquifers the cost ranges from \$14-18/tCO_2 (IEAGHG, 2005). Estimates previous to recent EPA guidance documents (2010b, 2012, 2013) predicted monitoring fees to be \$0.10-0.60 /tCO_2 (Benson, 2004; CSWG, 2009). These estimates required less frequent assessments (Benson, 2004) or shorter monitoring periods (CSWG, 2009) than what are now recommended (EPA, 2010b, 2012, 2013). The financial responsibility of the operator to cover liability is suggested to be between \$0.30-1.70/tCO_2 depending on site specific risk (CSWG, 2009). It follows that total project costs may fall between \$57-112/tCO_2.

Water/CO_2 co-injection methods increase capital and operating costs of GCS. Methods involving two-phase flow within the well-bore are expected to increase bottom-hole pressures as a result of relative permeability effects (Juanes et al., 2006; IEAGHG, 2010). This will increase operation costs as additional energy is required to overcome the greater bottom-hole pressures. There are also additional costs associated with drilling, completion, operation, and maintenance of brine production and injection wells. It has been proposed that additional costs may be out-weighted by reductions in monitoring fees and increased storage security, as buoyancy driven scCO_2 leakage is less likely (Keith et al., 2005; IEAGHG, 2010). However, a detailed cost analysis has not been developed to assess this relationship.

Co-injection Methods

Proposed schemes to improve storage security vary over a wide range of water injection rates and configurations (IEAGHG, 2010). Ex-situ CO_2 dissolution methods propose that injection occur as a CO_2 saturated brine (Keith et al., 2005; Leonenko et al., 2006; Burton and Bryant, 2007; Leonenko and Keith, 2008; Eke et. al. 2009; Fang et. al. 2010; Jain and Bryant, 2011). Water-alternating-gas (WAG) methods cyclically inject CO_2 and brine through the same well (Juanes et al., 2006; Leonenko et al., 2006; Zhang and Agarwal, 2012, 2013, 2014). Simultaneous water and gas (SWAG) injection would use separate wells for each fluid injected at the same time (Keith et al., 2005; Ide et al., 2007; Anchliya and Ehlig-Economides, 2009). Direct water/scCO_2 co-injection schemes propose simultaneously injecting both fluids through the same well (Qi et al., 2009). Post-CO_2 injection water flushes have been suggested through either the injection well or a separate well (Leonenko and Keith, 2008; Qi et al., 2009).

Ex-situ Dissolution

Ex-situ dissolution takes advantage of dissolved phase trapping by fully dissolving CO_2 in brine prior to injection and injecting the mixture as a single phase saturated brine (Lake, 1989; Burton and Bryant, 2007; Leonenko et al., 2006; Eke et. al. 2009; Fang et. al. 2010; Jain and Bryant, 2011). Single phase flow eliminates complications associated with saturation fronts, mobility ratios, viscous fingering, and reduced phase permeabilities (Burton and Bryant, 2007). Over time, the solution will tend to sink as a result of density differences with the native brine, removing the need for a perfect seal and allowing safe injection at shallower depths (Fang et. al., 2010).

Dissolution may use brine retrieved from the storage formation to reduce pressure buildup and direct the dissolved plume flow (Burton and Bryant, 2007), or ex-situ CO_2 dissolution may be retrofitted into existing brine disposal operations. These operations already account for pressure buildup and monitor dissolved plume migration. Simple calculations predict annual energy costs to be approximately $80,000 for one million tons of brine injection ($0.08/t$CO_2$), with a power requirement of 90 kW per year for the ex-situ dissolution process (Leonenko and Keith, 2008).

WAG

Water-alternating-gas injection through the same well has been successfully implemented in enhanced oil recovery (EOR) applications since the 1950's (Michael et al., 2011; IEAGHG, 2010). WAG injection is useful for breaking up large plumes, improving sweep in homogeneous aquifers, increasing dissolution rates, and increasing residual trapping (Gorell, 1990; Juanes et al., 2006; Zhang and Agarwal, 2012, 2013, 2014). WAG methods are most efficient at residual trapping when high CO_2 saturations are reached before water injection (Ide et al., 2007).

Previous simulations have applied WAG schemes to vertical and horizontal wells at annual and monthly cycles (Ide et al., 2007; Zhang and Agarwal, 2012, 2013, 2014, Zhang 2013). Cycle durations were arbitrary, based on the conclusion that WAG cycle duration does not lead to significant difference in oil recovery efficiency (Nasir and Chong, 2009; Zhang and Agarwal, 2012). Results found WAG injection via horizontal

wells favorable over vertical injection wells due to reduced CO_2 migration, lower gas saturation, and reduced pressure buildup (Zhang and Agarwal, 2012).

SWAG

Simultaneous water and gas injection via separate wells is also a technique developed for EOR to direct oil reserves to supply wells (IEAGHG, 2010). SWAG is applicable to GCS applications to enhance mixing of CO_2 in formation fluids (Keith et al., 2005; Ide etal., 2007; Anchliya and Ehlig-Economides, 2009; IEAGHG, 2010). Anchliya and Ehlig-Economides (2009) developed a SWAG system with two horizontal injectors in parallel (brine at the top of the formation, CO_2 at the bottom) and two brine producers flanking the CO_2 injector to avoid aquifer pressurization and direct the plume. Models showed this method prevented CO_2 accumulation at the top of the aquifer and trapped 90% of the CO_2 within 50 years from the start of injection, resulting in a storage efficiency of 8.5%.

Keith et al. (2005) developed a SWAG approach referred to as "in-situ dissolution", intended to dissolve sequestered $scCO_2$ by use of a long-term (~200-300 year) brine flush (Leonenko et al., 2006; Leonenko and Keith, 2008). This method would be applied to flat-lying formations via horizontal brine injection wells at the top of the storage aquifer (Keith et al., 2005). Brine production and injection would occur simultaneous to CO_2 injection and continue for 200 years post-CO_2 injection. Results show that 77-97% of injected CO_2 could be trapped in the dissolved phase by this

method, depending on the water injection rate. The cost of this method is predicted to be less than 1% of CCS capture costs (Keith et al., 2005).

Direct Co-injection and chase brine

Direct brine/scCO_2 co-injection has been suggested by Qi et al. (2009) as a means to reduce the mobility ratio during injection. By this method, scCO_2 and brine were simultaneously injected via the same well at prescribed fractional flow rates. The aquifer was then flushed with a chase brine of approximately 25% the mass of CO_2 stored. The chase brine is intended to reduce the buoyancy drive in the gas phase by displacing the source of high gas saturation surrounding the well. Results show a fractional flow of 0.85 or lower (scCO_2 to brine) will result in stable displacement (mobility ratios less than 1). Combined with the brine flush, 90% of the CO_2 was trapped in the modeled system. Additional costs are expected to be less than 3% of the total CCS implementation costs.

Objectives

This study has two objectives: (1) to determine a cost function that identifies economically efficient injection strategies to increase storage security through enhanced secondary trapping mechanisms and (2) to determine the effect of five different water/CO_2 co-injection methods on GCS costs and CO_2 trapping in comparison to standard scCO_2 injection in a representative storage formation. Co-injection strategies included dissolved CO_2 injection, SWAG injection, WAG injection, direct co-injection, and post CO_2-injection water flush. Long-term (200-300 year) in-situ dissolution strategies were excluded from simulations.

Methods

Lawrence Berkeley National Laboratory's iTOUGH2 and TOUGH2-ECO2N were used to obtain best estimates of water injection rates for water/CO_2 co-injection strategies to maximize CO_2 trapping and minimize cost. iTOUGH2 combines the simulation capabilities of TOUGH2-ECO2N with optimization techniques to support the design of CO_2 storage systems (Finsterle, 1999; Pruess et al., 1999). The cost function was minimized by adjusting water injection rates to improve CO_2 storage design based on certain observational output parameters. Following from iTOUGH2 applications to groundwater plume remediation design (Finsterle, 2006), solving this optimization problem required two steps. First, a cost function was defined as a function of TOUGH2-ECO2N output variables which depended on a variable water injection rate. Second, the Levenberg-Marquardt minimization algorithm updated water injection rates in order to reduce the value of the cost function for co-injection strategies. Supercritical CO_2 injection, dissolved CO_2 injection, SWAG, WAG, direct co-injection, and a post-CO_2 injection water flush were evaluated by this cost function. Following optimizations, separate simulations of water supply wells were run to determine the feasibility of producing the quantities of water needed from the storage formation for each method.

TOUGH2 model set-up

CO_2 injection models

Supercritical CO_2 injection, dissolved CO_2 injection, SWAG, WAG, direct co-injection, and a post-CO_2 injection water flush were simulated by TOUGH2-ECO2N

using a 3-D polygonal grid (Figure 4.1). These models took advantage of the symmetry of a homogeneous horizontal formation and only simulated one quarter of an 8km x 8km x 100m domain. Initial conditions reflected a formation at 1600 m depth, with pressures and temperatures ranging from 15 MPa and 38°C at top of formation to 16 MPa and 40°C at depth. Salinity was not included in the formation or injected fluid to simplify the problem.

A 400 m horizontal CO_2 injection well was at the center of all models in the middle of the formation thickness. Horizontal injection wells were chosen over vertical injection wells to improve the sweep in the formation and reduce injection pressures (IEAGHG, 2010). For the SWAG cases an additional 500 m horizontal water injection well was at the top of the formation. Fixed state boundary conditions were assigned to outer edges of the domain (opposite injection) and no-flow boundaries were assigned to the top, bottom, and along the boundaries including the injection well and adjacent elements. Hydrogeologic properties are characteristic of potential storage formations (Table 4.2, Cheng et al., 2013).

Supercritical CO_2 injection, SWAG, direct co-injection, and the post-CO_2 injection water flush models simulated 3.16 MtCO_2 injected over 20 years at a rate of 5 kg/s. This is equivalent to 20 kg/s for the total screened well in the system (Table 4.1). WAG injection required 25 years to inject the same mass of CO_2 in cycles of 1.5 years CO_2 injection at 6.66 kg/s to 1.0 year water injection. Preliminary results showed dissolved CO_2 injection needed to be split between four horizontal injection wells in

order to manage the pressure buildup while injecting the same mass of CO_2 as the other models. Only one of the four dissolved CO_2 injection wells was simulated, injecting 1.25 $kgCO_2/s$ over 20 years. No water supply wells were simulated in these models.

Table 4. 1 CO_2 injection schemes. Rates given for the total system.

Injection Strategy	**CO_2 injection**	
	Rate [kg/s]	*Duration [years]*
Supercritical CO_2	20	20
Dissolved CO2	20	20
Water Flush	20	20
WAG	26.7	1.5 (x10)
SWAG	20	20
Direct Co-injection	20	20

All simulation cases ran for 50 years post-CO_2 injection to monitor the plume, as recommended by the EPA (2010b, 2012, 2013). Results for all cases were calculated based on the CO_2 plume in the entire system, representing 12.6 Mt CO_2 total. This was equivalent to four of the modeled quadrants for $scCO_2$, WAG, SWAG, direct co-injection, and water flush methods and sixteen quadrants for the dissolved CO_2 strategy.

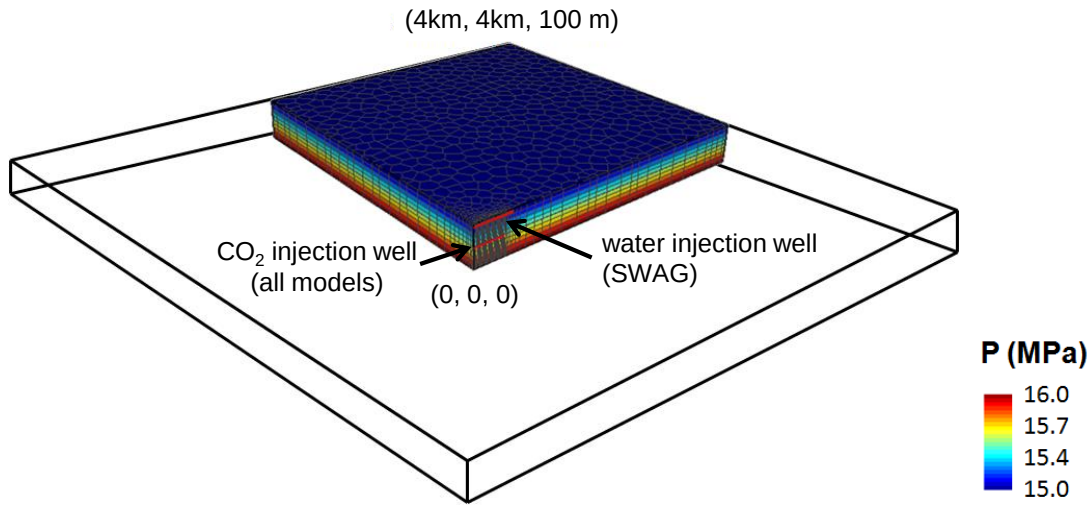

Figure 4. 1. Model initialization. Red lines show injection wells.

Table 4. 2. Hydrogeologic properties of the storage formation.

Porosity	φ	0.20
Horizontal permeability	k_r	5×10^{-13} m^2
Vertical permeability	k_z	5×10^{-14} m^2
Van Genuchten parameter	m	0.457
Residual S_w	S_{lr}	0.20
Residual S_{CO2}	S_{gr}	0.10
Capillary entry pressure	α^{-1}	1.95 kPa

Models were assessed at the end of a 50 year monitoring period based on plume extent, storage efficiency, secondary trapping percentage, maximum plume velocity, maximum mobility ratio of CO_2 to water, water use, and the cost relative to standard CO_2 injection. Storage efficiency calculations used the maximum areal extent of the plume multiplied by the formation thickness as the available storage volume.

Water Production Models

Separate TOUGH2-ECO2N simulations were run to determine the potential for water supply from the storage formation for use with co-injection strategies (Figure 4.2). The models were set up with alternating high and low permeability material layers extending to the surface. High permeability layers had the same hydrogeologic properties as the storage formation in Table 4.2, and low permeability layers were two orders of magnitude less permeable in all directions with reduced porosity to 5%. The model represented one quarter of a 40km x 40km x 1.6km domain. This larger domain was modeled in order to capture pressure changes due to injection and production processes without boundary effects. Initial conditions were set from atmospheric conditions to 16 MPa and 40º C at depth. A supply well was added 2.83 km from center of the injection well. This represented one supply well of four surrounding the injection well.

Water production simulations were run for each co-injection case using best estimates for water injection flow rates from ITOUGH2 optimizations. To simplify these models, multiphase flow processes were removed by injecting an equivalent slug of water in place of CO_2. Therefore, the total volume of fluid injected represented the total volume of water and CO_2 needed for each strategy. Supply wells were screened over the entire formation thickness and set up as wells on deliverability in TOUGH2. This approach used a prescribed bottomhole pressure. The bottomhole pressure was manually iterated until pumping produced the necessary amount of water for each case without causing drawdown at the surface. The flowing wellbore pressure used by TOUGH2 accounts for gravity effects through multiple layers and calculates the bottom-hole pressure using the

pressure set in the well elements above it (Pruess et al., 1999). The pressure given in a layered simulation is then the fixed pressure at the top of the well screen.

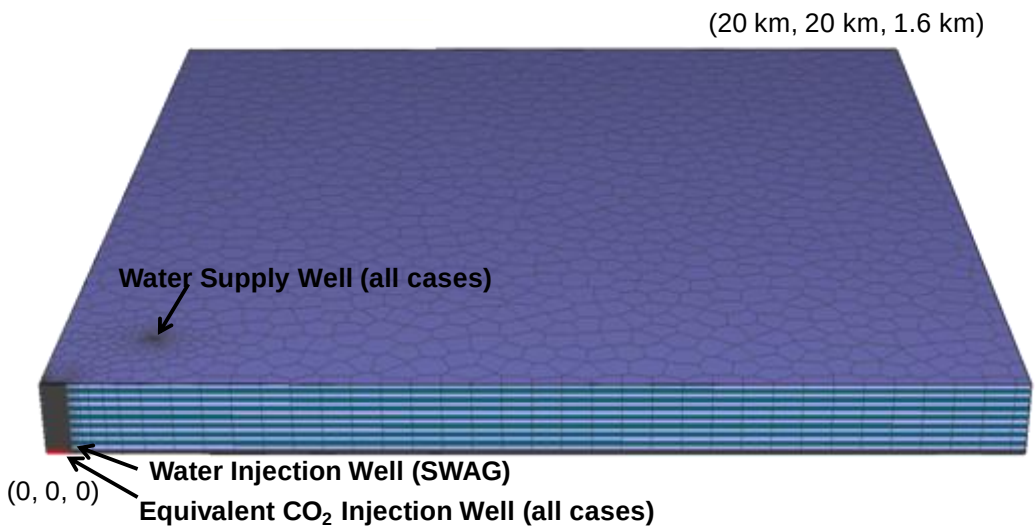

Figure 4. 2. Water supply model set up used to assess each co-injection strategy.

Cost analysis

A cost function was defined based on cost terms that would be affected by a change in the injection strategy. Terms in the cost function reflected capital and operating costs of water injection and production, and costs of monitoring, liability, and pore space leasing. The cost function did not include costs that must be paid regardless of injection strategy. For example, at least one CO_2 injection well was needed regardless of the strategy; therefore, well drilling and completion costs for that one horizontal CO_2 injection well were not included. In the dissolved case, the costs of the three additional

CO_2 injection wells were included. In this way, the cost function was only used to determine the change in cost from standard $scCO_2$ injection and results should *not* be considered a total cost. The contributions from the different costs were weighted in terms of 2013 US$. The L1-estimator was used to express the cost function as the sum of weighted costs (Finsterle, 2014).

$$C = \sum_i w_i \left| z_i \right| \tag{4. 1}$$

where *w* is the weight (2013 US$ per unit of z), z is the un-weighted variable cost, and *i* is the measurement time.

Capital and operating costs of water injection and production

Cost of electricity

Electrical requirements for injection and supply wells are included in the cost function as a sub-function of time and power. To estimate how the cost of electricity will change with time, historical and predicted data from the U.S. Energy Information Administration (EIA) for the industrial sector was considered. The EIA Annual Energy Review 2011 provides historical data on electricity prices from 1960 to 2011 (EIA, 2012, 2014). The EIA Annual Energy Outlook (AEO2013) predicts the U.S. energy supply, demand, and prices through 2040 based on a wide range of trends and issues that could have implications on the energy market (EIA, 2013). AEO2013 reports on six cases in-depth, varying assumptions about economic growth, oil price, nuclear plant lifetimes, renewable fuels, coal cost, liquids markets, and several policy changes. Results from the reference case, business-as-usual trends, are shown in Figure 4.3. This assumption results

in policy-neutral costs, as current laws and regulations are maintained. Industrial energy prices are compared to predictions by the Interindustry Forecasting Project of the University of Maryland (INFORUM), IHS Global Insight (IHSGI), and historical industrial energy prices (EIA, 2012, 2013).

These predictions do not account for change in electrical price due to CO_2 capture, which is estimated to increase the cost of electricity for a pulverized coal burning power plant by 42 to 65 percent (Rubin et al., 2007). The effect of CO_2 storage on overall industrial energy costs is uncertain. Electricity prices could gradually increase as more power plants incorporate CO_2 capture technologies, but capture costs are predicted to decrease over time as more research and development will be dedicated to improving capture technologies as they are implemented (DOE, 2014). It seems likely that the net effect will be an increase in electricity costs over current policy-neutral predictions. To account for this increase, the historical trend was extrapolated to predict future electricity prices. This trend was implemented into the cost analysis to provide a conservative cost estimate.

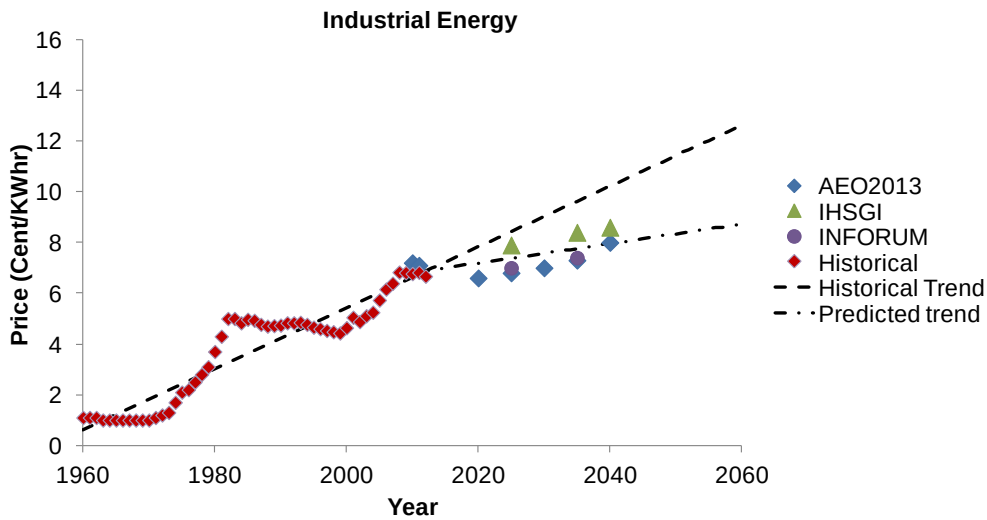

Figure 4. 3. Historical and predicted electricity prices for the industrial sector (EIA, 2012, 2013, 2014). Adjusted to 2013 USD. Dashed line indicates values used to weight the cost function through time.

To account for these predictions in the cost function, prices adjusted to 2013 US$ were set as weights, w_i, ($/kWhr) for measurement times at the beginning and end of simulation. The simulation was started at year 2015 and ended at year 2085 for all cases except WAG, when it ended at 2090. A linear interpolation matching the historical trend from Figure 4.3 was performed between weighted data points for observation times during the simulation. The cost of injection was then

$$C_1 = \sum_i w_i P \Delta t \tag{4. 2}$$

$$\Delta t = t_i - t_{i-1} \tag{4. 3}$$

where P is the power requirement in Watts, and the total electrical energy cost was calculated discretely at each observation time, t_i, where t_0 is zero.

Simplified electric power requirements for injection and production were given by

$$P = Eff \times Q \times \Delta p \tag{4. 4}$$

where *Eff* is the pump efficiency, set at 70% (Leonenko and Keith, 2008), *Q* is the total volumetric flow rate in the injection well, and *Δp* is the surface pump pressure in Pa (bottom-hole injection pressure minus hydrostatic pressure). The total volumetric flow rate included the flow rates of both $scCO_2$ and liquid water. It was assumed there was no capillary pressure within the well, so the surface pump pressure was taken as the same value for both phases. Electrical requirements of water supply wells were assumed to be equal to that of water injection. This was a conservative estimate as it is likely less electricity will be required to produce water from the pressurized formation once CO_2 injection begins.

A user defined function was written into the source code to include power as an observation variable in iTOUGH2. This function took advantage of existing iTOUGH2 observation variables "CUMULATIVE" and "DRAWDOWN". The "CUMULATIVE" command observes the cumulative mass of a phase or component injected by a source (Finsterle, 2014). In this case, the cumulative gas and liquid masses were observed and converted to cumulative volumes over an observation time step

$$V_{\beta.i} = \frac{M_{\beta,i} - M_{\beta,i-1}}{\rho_{\beta,i}} \tag{4. 5}$$

where $V_{\beta,i}$ is the cumulative volume of phase β injected between the current and previous observation times, t_i and t_{i-1}, $M_{\beta,i}$ and $M_{\beta,i-1}$ are the cumulative masses of phase β injected at the current and previous time, and $\rho_{\beta,i}$ is the density of phase β injected at the current time. The cumulative volume was used to solve for the volumetric flow rate in equation 4.4. The "DRAWDOWN" command observes the pressure difference from a specified reference pressure (Finsterle, 2014). It is designed to be used for observing drawdown during pumping tests, but was used to observe surface pump pressure in terms of pressure buildup in this case.

iTOUGH2 is structured such that it loops through observation times, observation types, and observation elements in a nested format. The cumulative volume and injection pressure were set as the first and second observation types; the power was set as the third observation type. Once the power observation type was reached, it was commanded to exit the element loop and calculate power at time t_i, based on the previous observation types using equation 4.4.

At this point, if the pressure buildup within the formation was greater than the fracture pressure (1.5 x hydrostatic pressure), there was a penalty applied to the cost of electrical power so the cost function would be excessively large. If the pressure build-up was below the fracture pressure, the cost of power was calculated based on the price of electricity at time t_i. To account for water supply wells the final cost was multiplied by two.

Additional well drilling and completion

Water supply wells are not simulated in the CO_2 injection models, but the associated capital costs were included as a constant in the cost function at the end of simulation runs. Quantifying the drilling cost for water supply wells is challenging due to restrictions in data collection and availability, or constraints with modeling (Kaiser, 2007). The Joint Association Survey on Drilling Costs (JAS) relies on an extensive amount of data collected annually about well completions for oil and gas operations in each state (API, 1998, 2001; Kaiser, 2007). Wells are specified as onshore or offshore, exploratory or development, and oil, gas, or dry. The depth, direction, and cost per foot are also reported. From this data, average cost estimates can be determined for individual vertical wells taking the form

$$C_2 = \mathrm{a}_1 \mathrm{e}^{\mathrm{a}_2 \mathrm{d}} \tag{4.6}$$

where a1 and a2 are location specific regression coefficients and d is the well depth in meters (API, 1998, 2001; McCoy and Rubin, 2009; Heddle et al., 2003).

JAS data from 2001 were used to determine appropriate regression coefficients for a water supply well at a potential CO_2 storage site in the Mid-continent region (API, 2001; McCoy and Rubin, 2009). The estimated cost adjusted to 2013 U.S. dollars is

$$C_2 = 136,213 e^{0.000804 d} \tag{4. 7}$$

At a targeted storage depth of 1600 m, the average cost of vertical well installation and completion is expected to be near $500,000 per water supply well.

For all co-injection strategies, it was assumed four water supply wells would surround one horizontal CO_2 injection well. This pattern could be extended to a field of CO_2 injection wells, in which case, water supply wells are shared. The more CO_2 injection wells in a field, the lower the ratio of water supply to CO_2 injection wells becomes. For patterns including one to nine injection wells, the ratio of water supply to CO_2 injection wells is between 4.0 and 1.78 (Figure 4.4). For the cost term, a ratio of two to one water supply to CO_2 injection wells was assumed and the capital cost of water supply wells was

$$C_2 = 2 \times \left(136,213 e^{0.000804d}\right) = \$986,109 \tag{4. 8}$$

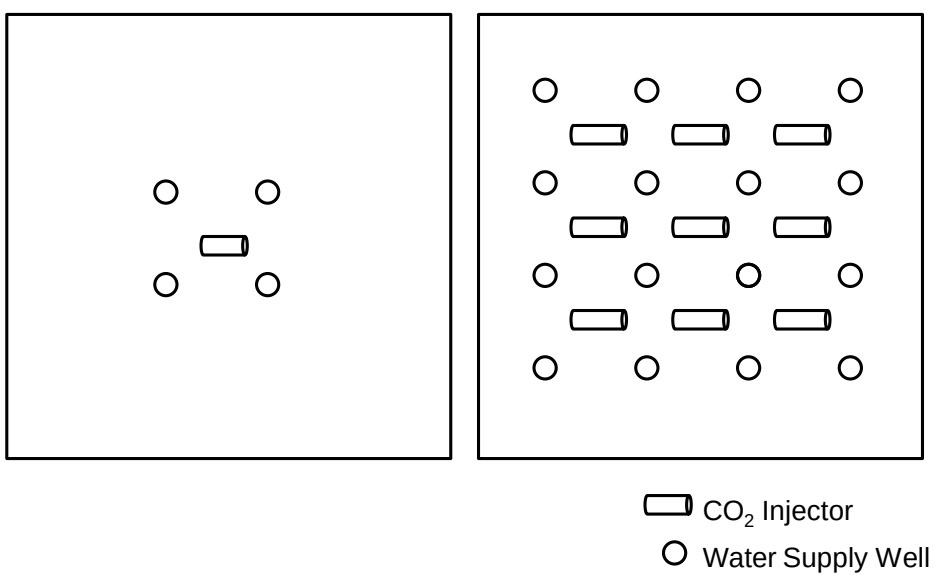

Figure 4. 4. Conceptual water supply well pattern. Four water producing wells surround the CO_2 injection well. Not to scale.

For SWAG injection, a horizontal water injection well was required. Horizontal wells cost 1.5 to 2.5 times more than vertical wells of the same length (Joshi, 2003). An additional capital cost was included in the C_3 term to account for a 2,500 m injection well in this scenario, where 1000 m was the horizontal length component and 1,500 m was the vertical component. To make a conservative estimate, it was assumed this well would cost 2.5 times the estimated vertical cost due to the depth required.

$$C_2 = 2 \times \left(136,213 e^{0.000804 d_1}\right) + 2.5 * \left(136,213 e^{0.000804 d_2}\right) = \$3,527,611 \tag{4. 9}$$

where d_1 was 1,600 m and d_2 was 2,500 m.

Three additional horizontal injection wells were added to the cost function of dissolved CO_2 injection to account for splitting up the total mass of CO_2 and water. These wells were 2,350 m in length and required two water supply wells each. For this case, 800 m was the horizontal length component and 1,550 m was the vertical component The cost term for dissolved injection became

$$C_2 = 8 \times \left(136,213 e^{0.000804 d_1}\right) + 3 \times 2.5 \times \left(136,213 e^{0.000804 d_2}\right) = 10,702,711 \tag{4. 10}$$

where d_1 was 1,600 m and d_2 was 2,350 m.

Monitoring Costs

Monitoring protocol depends on storage site characteristics and injection strategy, and generally includes remote sensing, geophysical methods, ground water and deep formation fluid sampling, surface flux monitoring, and pressure monitoring (Benson et al., 2004; Benson, 2004, 2006; EPA, 2010a; CSWG, 2009). For these simulations, the

monitoring methods were based on recommendations from a range of contributors, representing regulators (EPA, 2010a), legislators (CSWG, 2009), operators (Allinson, 2009), and scientists (Benson et al., 2004) (Table 4.3). Methods chosen to track injected CO_2 and monitor for leakage were interferometric synthetic aperture radar (InSAR), eddy covariance air monitoring, soil zone CO_2 monitoring, shallow monitoring wells, and 3D seismic imaging. InSAR is a remote sensing technique used to monitor land deformation and indirectly map CO_2 migration (Benson et al., 2004). It is particularly useful if dissolved CO_2 injection is implemented, as geophysical methods may not be able to distinguish the aqueous CO_2 from native formation fluid. Eddy covariance systems or eddy flux towers are used to measure CO_2 concentration in the air above a storage site to determine if there is leakage (Benson et al., 2004; EPA, 2010a). Soil zone CO_2 monitoring evaluates CO_2 flux in the first tens of feet below surface and is used to measure CO_2 seepage above natural fluctuations. Shallow monitoring wells above the injection zone allow for fluid sampling to protect groundwater resources (Benson et al., 2004; EPA, 2010a). Seismic imaging uses man-made or natural sources of acoustic energy to image subsurface fluids and is capable of distinguishing $scCO_2$ from native formation fluid (Benson et al., 2004). Periodic seismic surveys are generally cited as a necessary technique to characterize the plume distribution in the storage formation in high resolution (Benson, 2006; EPA, 2010a). In the dissolved CO_2 injection simulation, 3D seismic imaging was removed from monitoring costs as it is difficult to distinguish CO_2 saturated brine from formation brine by this method. These methods are all dependent on the spatial distribution of the plume and highlight advantages and

disadvantages of various injection strategies on plume migration when incorporated into the cost function.

The monitoring costs were assessed at the listed frequencies (Table 4.3) over the entire Area of Review (AOR), defined by the EPA (2013) to be the maximum expected plume extent. For these simulations, the AOR was the maximum areal plume extent plus a 10% buffer zone as recommended by the Wyoming Carbon Sequestration Working Group (CSWG, 2009). In simulations including $scCO_2$, the maximum areal extent, $A_{max,scCO_2}$, was determined by the calculating the sum of the areas of elements containing mobile $scCO_2$ along the caprock. This was done using the "VOLUME" observation type in iTOUGH2 (Finsterle, 2014). If an element along the caprock contained $scCO_2$, the volume of the element was added to a cumulative volumetric extent. The layer thickness was the same throughout the model, the areal extent of the mobile $scCO_2$ saturation was found by dividing the final volumetric extent by the thickness. The maximum areal extent term was stored and compared to each new areal extent calculated to determine if a new maximum was achieved. For dissolved CO_2 injection, the areal extent was calculated in terms of the maximum areal extent of the dissolved CO_2 plume, $A_{max,\ aqCO2}$. The minimum cutoff was an aqueous CO_2 mass fraction of 0.001.

Table 4. 3. Monitoring Costs.

Monitoring Method	Cost (2013 US$)	Quantity	Frequency	
			Injection	Monitoring
Remote sensing –				
InSAR[1]	$3,144/km^2		every 2 years	
Air, Soil Gas Tracers –				
Eddy Covariance System[2]	$38,673.75/system	1 system/ 5 km^2	1 time fee	
Soil CO_2 Monitors[2]	$14,956.70/monitor	1 monitor/ 2.5 km^2	1 time fee	
Eddy Survey Costs[2]	$10,683.36/survey	1 survey/ 5 km^2	every year	
Soil CO_2 Survey Costs[2]	$641.00/2.5 km^2	600 samples/ station	every 2 years	
Water/Brine Sampling –				
Monitoring Wells[2]	$85,466.85/well	1 monitoring well/4 km	1 time fee	
Geophysical –				
3D Seismic[2,3,4]	$13,600 /km^2		1, 3, 5, 10, 15, 20	every 5 years

1. Corra et al., 2009
2. EPA, 2010a
3. Benson et al., 2004
4. Allinson et al., 2009

At the end of the simulation, a bulk weight was multiplied by the maximum areal extent representing the sum cost of monitoring methods in terms of dollars per meter squared (Table 4.3). This bulk weight varied for the WAG case and the dissolved injection case. The WAG injection required 5 additional years of monitoring and the dissolved case disregarded 3D seismic costs.

Table 4. 4. Monitoring costs of injection strategies. Cost was weighted in terms of $/m^2.

Injection Strategy	**Cost, C_3**	**Equation**
$scCO_2$, direct co-injection, SWAG, water flush	$1.07A_{max,scCO2}$	(4. 11)
WAG	$1.13A_{max,scCO2}$	(4. 12)
Dissolved CO_2 injection	$0.27A_{max,aqCO2}$	(4. 13)

Pore space leasing

Property rights to lease the pore space were also applied to the maximum areal extent as an additional fee of $55 per acre (Table 4.4) (EPA, 2010a). This is representative of an upfront fee for the pore space use and not a continued fee per ton of CO_2 (EPA, 2010a).

Table 4. 5 Cost of Pore space leasing per injection strategy. Cost was weighted in terms of $/m^2.

Injection Strategy	**Cost, C_4**	**Equation**
$scCO_2$, direct co-injection, SWAG, WAG, water flush	$0.0136A_{max,scCO2}$	(4. 14)
Dissolved CO_2 injection	$0.0136A_{max,aqCO2}$	(4. 15)

<u>Liability insurance</u>

The amount of CO_2 trapped by secondary methods impacts the cost of financial assurance needed to cover GCS projects. Financial assurance instruments, including public liability insurance, bonds, and trust funds, aim to offer assurances to the public and

private sector, and appropriately manage the risks inherent to GCS activities (CSWG, 2009; EPA, 2011). Forms of financial assurance are designed based on site specific risks. While current documentation does not specifically address liability in terms of the amount of trapped CO_2, it is reasonable to infer that liability costs related to plume migration and CO_2 leakage will be reduced appropriately in accordance with enhanced secondary trapping (CSWG, 2009; EPA, 2011).

A financial assurance policy was developed by the Wyoming CSWG (2009) to quantify general liability insurance fees related to GCS in their state. They recommended that $35M be allotted to insurance for 60 Megatons of CO_2 injection over 30 years at 2 Mt/year (plus or minus $10M depending on the site) (CSWG, 2009). This simplifies to $0.58/t$CO_2$.

Breaking down this recommendation for use in the cost function, fees related to water quality contamination, entrained contaminant releases (non-CO_2), modified surface topography, or other accidents affecting infrastructure were considered necessary for all injection strategies and were excluded from the cost function. Fees related to mitigating a large volume gas release or chronic low-level gas releases to the surface were considered necessary dependant on the mass of mobile scCO_2. These fees are recommended to cost $22M of the $35M total (CSWG, 2009). This results in a liability insurance fee of $0.37 per ton of sc$CO_2$. The cost function applied this fee on the maximum mass of mobile scCO_2 during the simulation.

$$C_5 = 3.66 \times 10^{-4} M_{CO_2,f} \tag{4. 16}$$

where $M_{CO_2,f}$ (kg) is the mass of free, or mobile, CO_2 at the end of injection.

The mass of mobile CO_2 was determined by modifying the "TOTAL MASS" observation type in iTOUGH2 to include mobile CO_2 as a separate phase (Finsterle, 2014). Mobile $scCO_2$ was differentiated from total $scCO_2$ by adding an "if/then" statement to iTOUGH2 that considered mobile CO_2 to be present in any element with CO_2 saturation greater than the residual saturation; otherwise, the CO_2 was considered to be immobilized.

Cost Function

The final cost function is given by the sum of the costs,

$$C = C_1 + C_2 + C_3 + C_4 + C_5 \tag{4. 17}$$

Minimization Algorithm

The Levenberg-Marquardt method was chosen to solve minimization problems based on reported efficiency and accuracy (Finsterle, 2006). As described by the *iTOUGH2 User's Guide* (Finsterle, 1999), by this method, the vector **p** contains all operational parameters (water injection rates) that are automatically adjusted to minimize C. The iterative minimization of C involves computing a correction vector $\Delta\mathbf{p}_k$ such that the new parameter set $\mathbf{p}_{k+1} = \mathbf{p}_k + \Delta\,\mathbf{p}_k$ leads to a reduction in the cost function, $C_{k+1} < C_k$, at each iTOUGH2 iteration k. The differences between minimization algorithms are

found in the way they calculate $\Delta\mathbf{p}_k$. The Levenberg-Marquardt algorithm calculates $\Delta\mathbf{p}_k$ by

$$\Delta\mathbf{p}_k = (\mathbf{J}_k^T\mathbf{W}\mathbf{J}_k + \lambda\mathbf{I})^{-1}\mathbf{J}_k^T\mathbf{W}\mathbf{z}_k \tag{4. 18}$$

where **J** is the Jacobian matrix, **W** is the weighting matrix, λ is the Levenberg parameter (Levenberg, 1944), **I** is the identity matrix, and **z** is the un-weighted cost vector. The Jacobian matrix is given by

$$\mathbf{J} = \frac{\partial z}{\partial p} = \begin{bmatrix} \frac{\partial z_1}{\partial p_1} & \cdots & \frac{\partial z_1}{\partial p_n} \\ \vdots & & \vdots \\ \frac{\partial z_m}{\partial p_1} & \cdots & \frac{\partial z_m}{\partial p_n} \end{bmatrix} \tag{4. 19}$$

The optimization algorithm is summarized in Figure 4.5 based on the description by Finsterle (1999). The optimization process begins with an initial guess of $\mathbf{p}_0$. The first TOUGH2 simulation is run and the initial cost, $C(\mathbf{p}_0)$, is determined from the observational parameters $z(\mathbf{p}_k)$. Equation 4.18 is applied to calculate the new $\mathbf{p}_k$. A new TOUGH2 simulation is run. After each TOUGH2 simulation, the cost is assessed. If the new cost is greater than the old cost, the Levenberg parameter is multiplied by the Marquardt (1963) parameter and another new TOUGH2 simulation is run. If the new cost is less than the old cost, the Levenberg parameter is divided by the Marquardt parameter and the convergence criteria are evaluated. If convergence criteria are not met, a new iTOUGH2 iteration is performed. This iterative process is continued until some convergence criteria is met; for example, when the norm of the gradient vector is smaller than a specified tolerance (Finsterle, 1999). The cost function is usually substantially

reduced during the first few steps. It is recommended by Finsterle (1999) to limit the number of iterations to reduce inefficiencies related to small steps at later iterations. These optimization runs were all limited to 10 iterations.

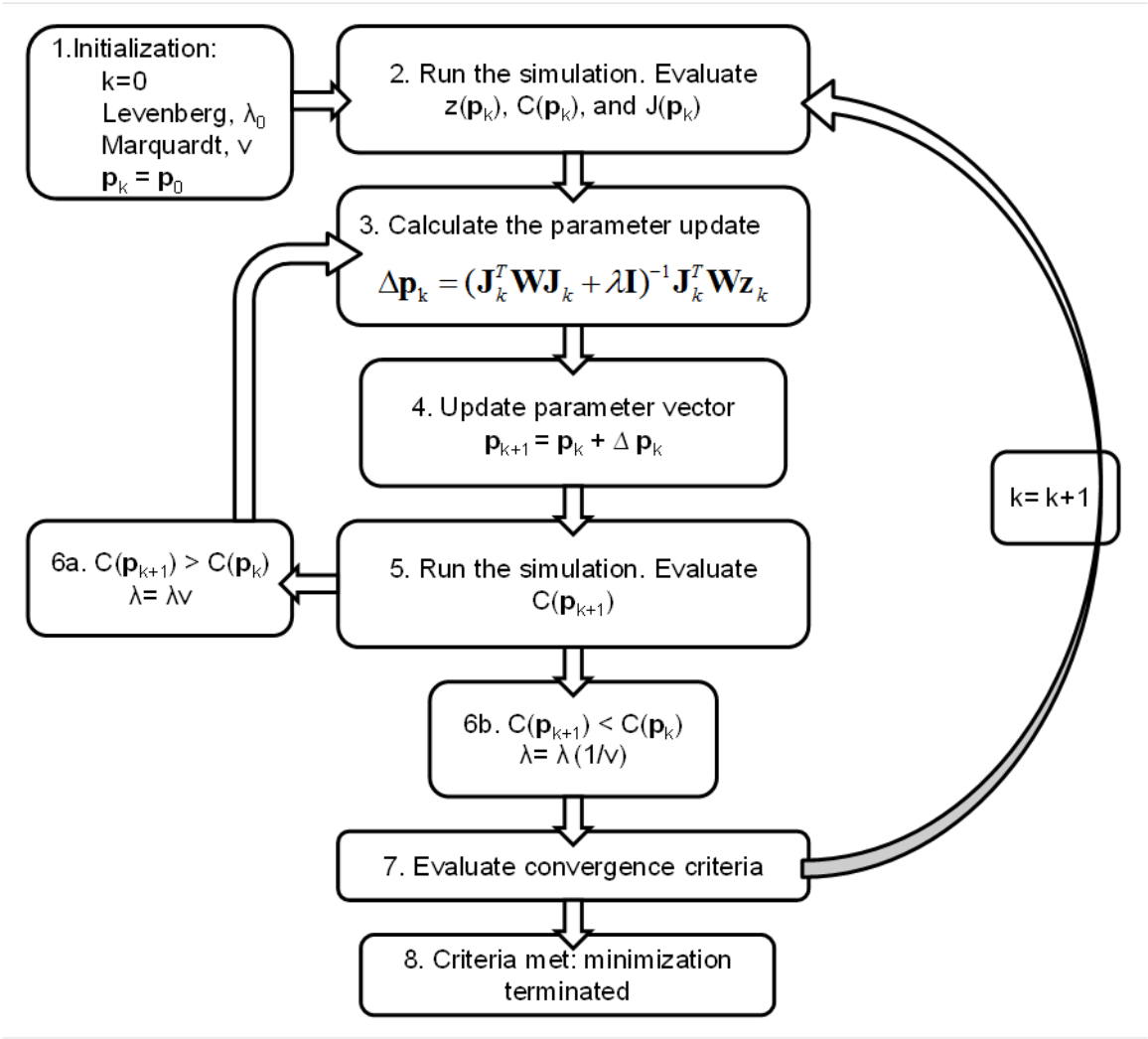

Figure 4. 5. Levenberg-Marquardt minimization algorithm employed by iTOUGH2.

Results

Best estimates for water injection rates were predicted by the Levenberg-Marquardt method (Table 4.6). Cost analyses showed that SWAG, WAG, and post-injection water flush strategies will be able to reduce costs below standard $scCO_2$ injection costs (Table 4.7). SWAG and WAG methods reduced the areal extent of the CO_2 plume and all co-injection strategies increased CO_2 secondary trapping rates (Table 4.8).

Table 4. 6. Best estimates for water injection rates. The number of iTOUGH2 iterations and TOUGH2-ECO2N simulations performed is given.

Injection Strategy	**iT2 Iter.**	**T2 Sim.**	**Best Estimate for Water Injection**		
			Rate[kg/s]	*Duration [years]*	*Total [Bgal]*
Supercritical CO_2	1	1	n/a	-	-
Dissolved CO_2	1	1	100 kg/s	20	16.7
Water Flush	10	34	57.2 kg/s	5	2.4
WAG	10	25	86.6	1 (x10)	7.2
SWAG	9	34	74	20	12.4
Direct Co-injection	9	36	3.2	20	0.5

Table 4. 7. Minimized cost functions. The cost is given for the total system.

Injection Strategy	**Cost Function**	
	Total [M$]	*per-ton [$/t$CO_2$]*
Supercritical CO_2	14	1.14
Dissolved CO_2	23.8	1.89
Water Flush	14.4	1.14
WAG	12.4	0.98
SWAG	10.5	0.83
Direct Co-injection	14.6	1.16

Table 4. 8. Plume properties. *A* is the maximum areal extent, S_E is the storage efficiency, *M* is the mobility ratio, and ***v*** is the Darcy velocity.

Injection Strategy	***A***	S_E	**Secondary Trapping**		***M***	***v***
	[km²]	*[%]*	*Residual Gas [%]*	*Dissolved CO_2 [%]*	*[-]*	
Supercritical CO_2	9.9	8	21	21	4.12	1.75 cm/day
Dissolved CO_2	19.5	4	0	100	1.00	2.1 mm/day
Water Flush	9.9	8	23	26	3.70	3.9 mm/day
WAG	7.3	11	31	33	3.20	3.1 mm/day
SWAG	4.1	19	49	37	9.31	2.5 cm/day
Direct Co-injection	9.9	8	21	22	4.20	1.6 cm/day

Supercritical CO_2 injection

Supercritical CO_2 injection was simulated using one ITOUGH2 iteration consisting of one TOUGH2-ECO2N simulation to establish a baseline cost for CO_2 storage design (Figure 4.6). CO_2 was injected at a rate of 5 kg/s for 20 years and monitored for 50 years. In this time, the plume spread 2.48 km^2 along the top of the model domain, equating to 9.92 km^2 for the total plume (rotated about all four quadrants) and a storage efficiency of 8%. Ultimately, 42% of the CO_2 was trapped, split equally between dissolved and residual trapping. Mobile scCO_2 was still flowing at the end of simulation, with unstable displacement along the caprock, at a maximum mobility ratio of 4.12 and a maximum velocity of 1.75 cm/day.

The cost function calculated for the base case injection strategy was $14,401,791 or $1.14/t$CO_2$. The majority of this cost was due to monitoring (75%), followed by liability insurance (24%).

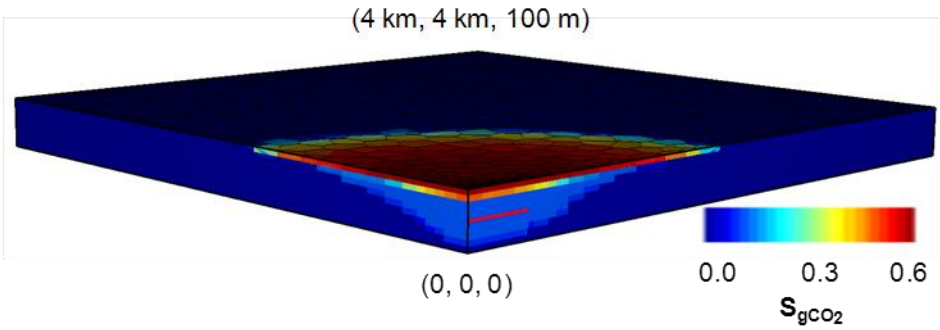

Figure 4. 6. Supercritical CO_2 injection. 70 years from beginning of injection.

Ex-situ dissolved CO_2 injection

Dissolved CO_2 injection was simulated using one ITOUGH2 iteration consisting of one TOUGH2-ECO2N simulation (Figure 4.7). The minimization algorithm was not needed as the limited solubility of CO_2 dictated the water injection rate. Injection was performed at 1.25 kg/s CO_2 to 25 kg/s water for 20 years. This method required 16.7 billion gallons of water per injection well (taking into account all four quadrants of the system).

The dissolved plume in the model domain was 1.22 km^2. This is 4.88 km^2 for one of four injection sites needed to inject the same mass of CO_2 as the other cases. This results in 20 km^2 of dissolved CO_2 to monitor. The dissolved plume had a storage efficiency of 4%, which is lower than $scCO_2$ injection, despite the improvement in vertical sweep, because of the greater volume needed to inject the equivalent mass of CO_2 while managing pressure buildup. While the storage efficiency was lower, the storage security was higher than $scCO_2$ injection as 100% of the CO_2 was trapped in the aqueous phase at all times through simulation. Following the monitoring period, the

plume migrated with stable displacement (mobility ratio of 1) at a maximum velocity of 2.1 mm/day.

The cost analysis calculated this strategy to be $9.4M more than the $scCO_2$ injection based on the chosen four-well injection scheme. This results in an increase of $0.75/t$CO_2$. The majority of this cost was due to well drilling and completion (45%) and electrical power (32%).

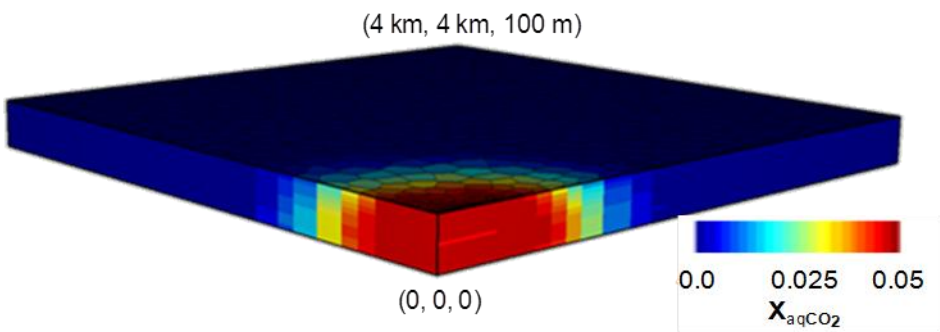

Figure 4. 7. Dissolved CO_2 injection. 70 years from beginning of injection.

WAG injection

WAG injection was optimized using 10 ITOUGH2 iterations consisting of 36 TOUGH2-ECO2N simulations (Figure 4.8). Cycles consisted of 1.5 years $scCO_2$ injection at 6.67 kg/s to 1.0 year of water injection for 25 years. The injection rate of water was optimized to a best estimate of 21.64 kg/s. This method required 7.2 billion gallons of water total.

The $scCO_2$ plume was reduced to 1.82 km^2 in the model domain, or 7.28 km^2 total, by the end of monitoring. The storage efficiency was improved to 11% and secondary CO_2 trapping was enhanced to 64% (33% dissolved and 31% residually trapped). The maximum mobility ratio of CO_2 to water was reduced to 3.0, and the $scCO_2$ plume had a maximum 3.1 mm/day.

The cost function calculated this method to be $2M less than the base case, a decrease of $0.16/t$CO_2$. Monitoring costs were the most expensive portion of the cost (66%), followed by electrical power (18%), liability insurance (8%), and supply well drilling and completion (8%).

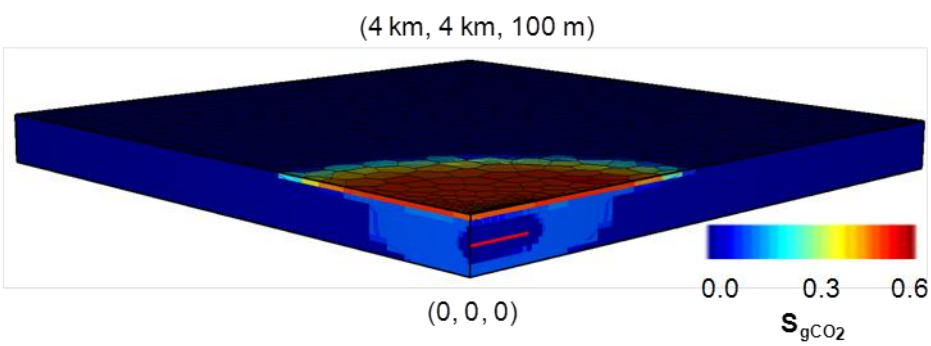

Figure 4. 8. WAG injection. 75 years from beginning of injection.

SWAG injection

SWAG injection was optimized using 9 ITOUGH2 iterations of 34 TOUGH2-ECO2N simulations (Figure 4.9). The best estimate for water injection rate was 18.51

kg/s for CO_2 injection at 5 kg/s over 20 years. This method required 12.4 billion gallons of water total. This method resulted in the largest overall cost reduction.

The $scCO_2$ plume was reduced to the smallest extent at 1.03 km^2 within the model domain, or 4.12 km^2 total, with the greatest storage efficiency at 19%. Eighty-six percent of the CO_2 was trapped by the end of the simulation (37% dissolved and 49% residually trapped). This is in close agreement with previous simulations predicting 90% trapping (Anchliya and Ehlig-Economides, 2009). The mobile portion of the plume was migrating at a maximum velocity of 2.5 cm/day. The maximum mobility ratio was increased to 9.31.

The cost analysis calculated this method to be $3.9M less than the base case, saving $0.31/t$CO_2$. Monitoring costs were the greatest portion of the final cost (43%), followed by well drilling and completion (34%), electrical power (17%), and liability insurance (6%).

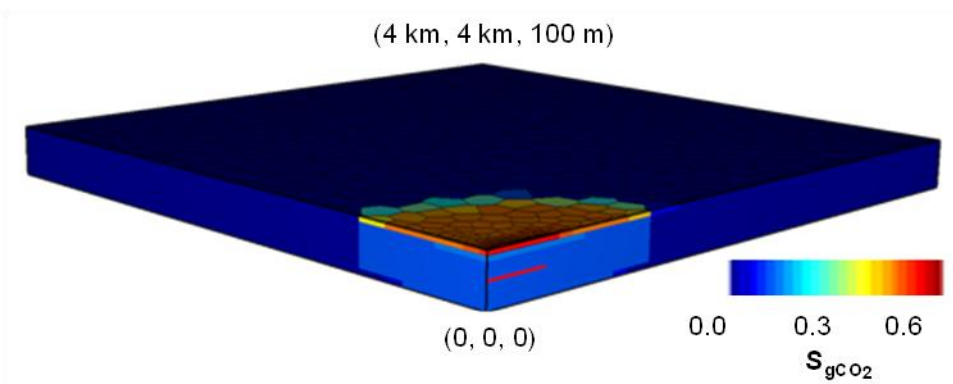

Figure 4. 9. SWAG injection. 70 years from beginning of injection

Direct co-injection

Direct water/CO_2 co-injection optimizations took 9 ITOUGH2 iterations and 37 TOUGH2-ECO2N simulations (Figure 4.10). The best estimate of water injection rate was 0.80 kg/s to 5 kg/s CO_2 injection over 20 years. This was 83% fractional flow of CO_2 to water is within the suggested range of 85% or less (Qi et al., 2009). This method required 0.5 billion gallons of water total.

The $scCO_2$ plume extent was not changed from the base case, at 2.48 km^2, resulting in the same storage efficiency. There was a small enhancement of secondary trapping, at 43% (22% dissolved and 21% residually trapped). The maximum mobility ratio at the end of monitoring was 4.12 and the maximum velocity was slightly reduced to 1.6 cm/day. During injection the mobility ratio in source elements was less than one, in agreement with calculations of Qi et al. (2009), but without the chase brine flush, the secondary trapping does not reach the predicted 90%.

The cost analysis calculated that this method would add \$0.02/tCO_2. The 1% improvement in trapping decreased the cost of liability insurance by 7.5%, but the additional cost of supply wells and electrical power out-weighted this benefit. The cost of monitoring was unchanged.

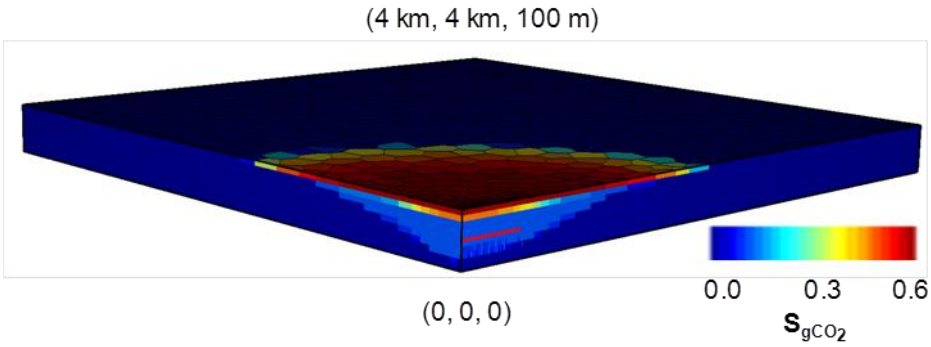

Figure 4. 10. Direct co-injection. 70 years from beginning of injection

Water Flush

The post-CO_2 injection water-flush optimizations took 10 iTOUGH2 iterations and 34 TOUGH2-ECO2N simulations (Figure 4.11). Supercritical CO_2 injection was performed as in the base case and the best estimate for water flush rate was determined to be 14.29 kg/s for five years. The water flush was included in the 50 year monitoring period. This method required 2.4 billion gallons of water total, 72% of the mass of injected CO_2. This is three times more water than optimized by Qi et al. (2009), with one difference being the well orientation. Qi et al. (2009) used vertical injection wells that required lower flow rates to flush the CO_2 plume than the horizontal ones used in this study.

This method did not affect the $scCO_2$ plume extent or storage efficiency, but did enhance secondary trapping to 49% (26% dissolved and 23% residually trapped). The water flush successfully displaced the high CO_2 saturation near the injection well, reducing the buoyancy force acting on the plume and thus reducing the maximum velocity to 3.9 mm/day. The maximum mobility ratio was slightly reduced to 3.75.

The cost analysis calculated no significant difference between this method and standard $scCO_2$ injection on a per-ton basis but did distribute costs differently among terms. Monitoring fees were still the most expensive portion of the cost function (75%). Liability insurance was reduced by 7% (17% total), but supply well development and completion increased the cost by 7%.

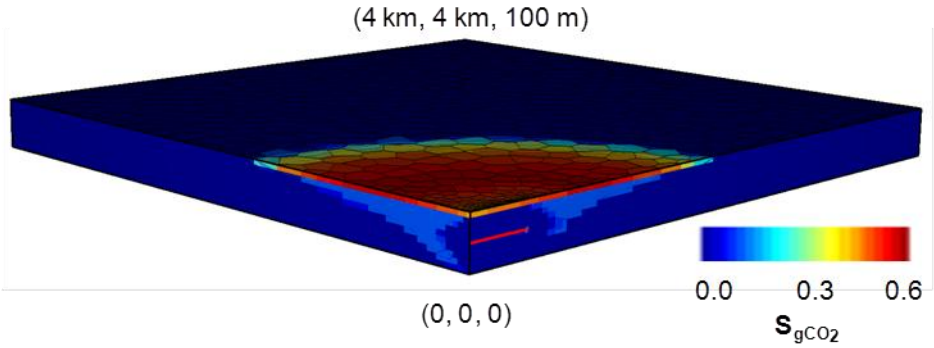

Figure 4. 11. Post- CO_2 injection water flush. 70 years from beginning of injection.

Water Production

Pumping was required for all cases to meet water needs (Table 4.9). Pumping rates were varied manually until results were able to provide the necessary water supply without reducing hydraulic heads near the surface, protecting drinking water resources. Optimization results showed the post-CO_2 injection water flush would require 2.4 billion gallons of water. To avoid complications of producing and storing this amount of water during CO_2 injection, formation water production began immediately following CO_2 injection and occurred for 5 years. Due to manual iterations, the water produced is slightly larger than necessary. A minimization algorithm could be applied to these models

as well to determine the optimum pumping rate. These results indicate the production of supply water from within the formation may be possible.

Table 4. 9. Water production design. Total quantities of water needed and produced in a five-spot pattern are given in billions of gallons (BG). Fixed pressure was at the top of well screen, where hydrostatic pressure was 15 MPa.

Injection Strategy	Water needs (BG)	Water Produced (BG)	Fixed Pressure (Mpa)
Direct Co-injection	0.5	1.0	15.7
Water Flush	2.4	2.7	14.6
WAG	7.2	7.4	14.2
SWAG	12.4	13.0	13.5
Dissolved CO_2	16.7	17.1	13.4

Discussion

These results can be used to determine when co-injection strategies become favorable in comparison to each other. For instance, Figure 4.12 shows the cumulative cost function over time of each injection strategy. This plot shows which strategies will be less expensive than standard $scCO_2$ injection and at what point in the injection or monitoring periods they become so. WAG becomes less expensive than $scCO_2$ injection first, between five and ten years during the injection period. SWAG becomes less expensive than $scCO_2$ injection between 20 and 25 years, immediately following the injection period. A strong case could be made to implement these two methods as the simulations showed increased storage security (via secondary trapping) and they recovered from the higher initial investment within a relevant time to the project stakeholders.

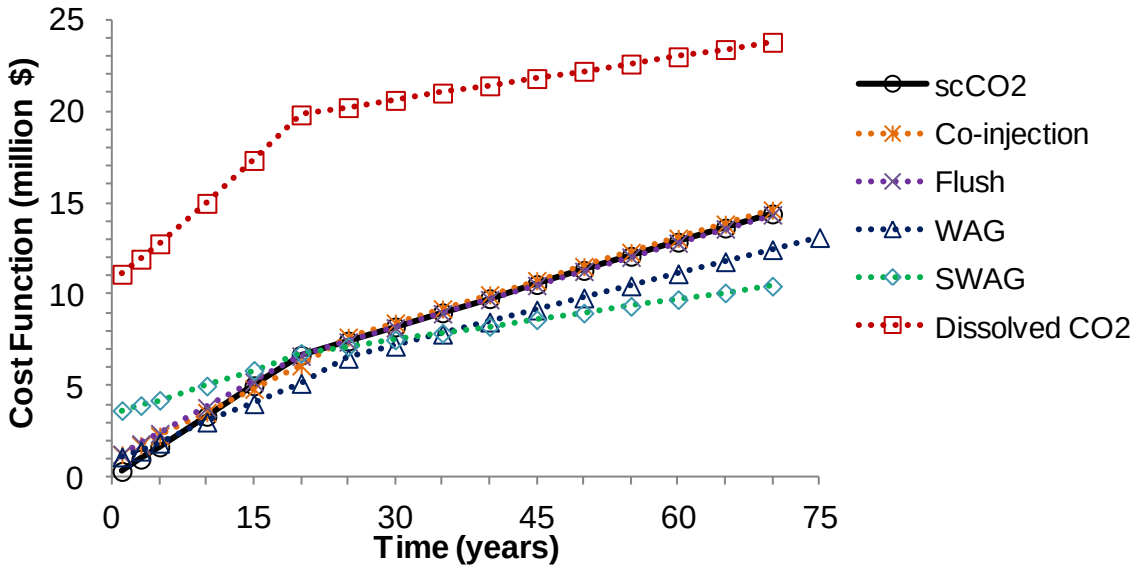

Figure 4. 12. Cost function of each injection strategy over time.

Figure 4.13 shows the secondary trapping performance of each strategy over time. This plot is useful to understand the behavior of trapped CO_2 during injection and monitoring periods. In both the SWAG and WAG cases, a portion of the CO_2 is remobilized following the maximum trapped percentage. During the SWAG case, remobilization occurred five years after injection ended. During injection, the $scCO_2$ plume was pushed down and laterally out by the more dense injected water. Once water injection ended, the small amount of mobile CO_2 at depth buoyantly rose and incorporated residually trapped CO_2 above it. During the WAG case, 100% secondary trapping occurred at year five; this was immediately after the second WAG cycle. Once the third cycle began, the injected CO_2 plume pushed through residually trapped bubbles, remobilizing them. As the CO_2 plume traveled farther from the well, the plume front became less affected by the water cycles and trapping decreased.

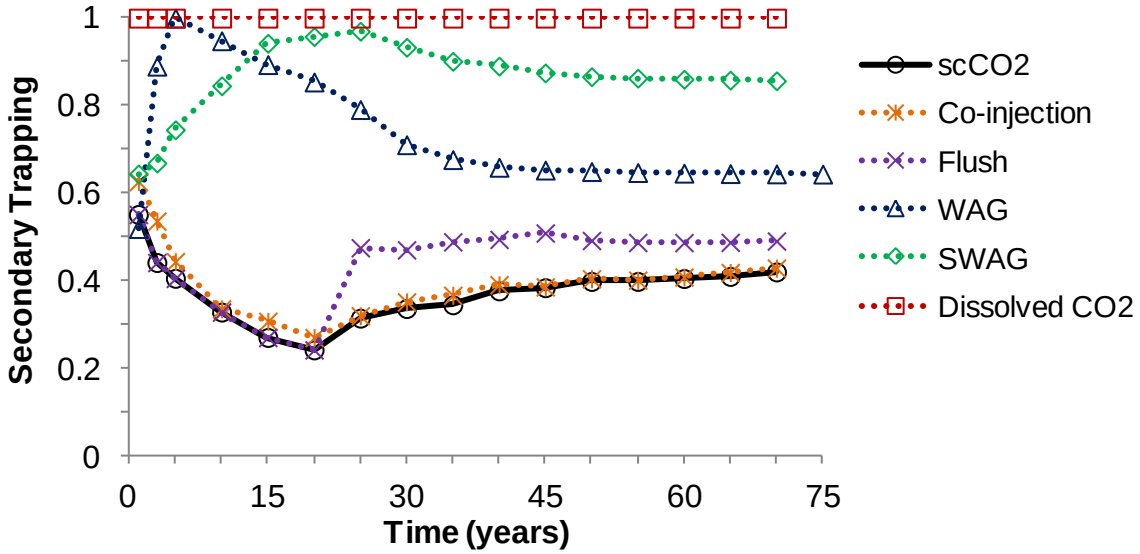

Figure 4. 13. Secondary trapping performance of each injection strategy over time.

It is important to take this dynamic behavior into consideration when establishing expected trapping performance. Liability insurance fees could change based on the time at which secondary trapping is estimated. In these cases, the liability fee took into account the maximum mass of mobile CO_2 in system. For the SWAG and WAG strategies this mass was taken at the end of the monitoring period. For the other cases, this mass was taken at the end of injection.

The trapping performance over time is also useful data to make a case for a post-CO_2 injection water flush. While the cost function did not reflect an advantage or disadvantage to this strategy over standard $scCO_2$ injection, it is clear that the water flush was effective at enhancing secondary CO_2 trapping, a major goal of these storage designs. A post-CO_2 injection water flush may also be effective when used in conjunction with a SWAG ,WAG, or direct co-injection strategy.

Strategies requiring water from the start of injection (direct co-injection, SWAG, and dissolved CO_2 injection) may require pre-CO_2 injection water pumping or supplementary water from an outside source until they are able to switch to a sustainable source from the storage formation. Design considerations could include supplementary water from existing brine disposal operations near the storage site. If available, it might be economically favorable to use this supplementary brine in place of formation brine for the entirety of the lower water use strategies, like direct co-injection or water flush strategies.

Dissolved CO_2 injection could be implemented in conjunction with existing Class II brine disposal wells. In this case, the capital costs for well drilling and completion would be negated, reducing the total cost by 10.7 M$, and bringing this strategy within the range of the other co-injection models. Additional costs need to be evaluated in this case. For example, the need for additional CO_2 pipeline transport to these existing locations. However, this may be a viable option for economically efficient CO_2 storage.

This cost assessment provides a starting point for CO_2 storage design in the planning phase. In reality, storage, monitoring, and liability costs are uncertain due to variability in formation properties, site specific regulations, and many other factors (IEAGHG, 2010; Cheng et al., 2013; Mathias, et al., 2013). For instance, lower intrinsic permeability ($<5\times10^{-13}$) is associated with higher CO_2 storage costs, higher Van Genuchten *m* values (>0.6) are associated with lower storage costs, and lower residual gas saturations (<0.15) are associated with higher costs per-ton of CO_2 injected (Cheng et

al., 2013). Salinity will also decrease the solubility of CO_2 in water. It is recommended to run an assessment like this over a range of expected *k*, *m*, and S_{gr} values and include salinity to determine if one co-injection method is consistently favorable over standard $scCO_2$ injection for specific GCS sites. Future simulations will also be run using higher $scCO_2$ injection rates. These simulations were bounded by the mass of CO_2 used in the dissolved CO_2 injection case. If the dissolved case is neglected, the other co-injection strategies can be simulated at higher, more realistic, injection rates.

Conclusions

This study demonstrated the development of a cost function for use in CO_2 storage design using water/CO_2 co-injection strategies. Terms in the cost function reflected capital and operating costs of water injection and production, and costs of monitoring, liability, and pore space leasing. The cost function was optimized by adjusting water injection rates in five different schemes. In this way, the cost function produced values reflecting advantages or disadvantages of the various co-injection schemes.

Results showed SWAG, WAG, and water flush strategies reduced costs while increasing secondary CO_2 trapping. WAG injection reduced costs the fastest, compensating for additional up-front costs within 5-10 years from start of injection. SWAG injection reduced costs the most, by \$0.31/tCO_2. The post-CO_2 injection water flush decreased costs with the least additional water use, at 2.4 billion gallons. Dissolved CO_2 injection was unable to reduce the cost function, but trapped the most CO_2 of any

method. Direct water/CO_2 co-injection was the only method unable to reduce cost or significantly increase CO_2 trapping.

This methodology for assessing water/CO_2 co-injection strategies could be used to assess specific storage sites for the potential to enhance secondary trapping and increase storage security over standard $scCO_2$ injection cost effectively. This approach is flexible to include or exclude terms or change weights to fit a particular storage project. An assessment over a range of expected hydrogeologic values or weights would provide useful information about which injection strategies are favorable at a targeted GCS site.

Works Cited

Allinson, G., Cinar, Y., Hou, W., Neal, P., 2009. The costs of CO_2 transport and injection in Australia. CO2TECH consultancy report.

Anchliya, A., Ehlig-Economides, C., 2009. Aquifer management to accelerate CO_2 dissolution and trapping. Proceedings of the SPE International Conference on CO_2 Capture, Storage, and Utilization Solution s and Technology for Our Energy and Climate Future. 2-4 November.

American Petroleum Institute (API), 1998. Joint association survey on drilling costs.

American Petroleum Institute (API), 2001. Joint association survey on drilling costs.

Benson, S., Gasperikova, E., Hoversten, M., 2004. Overview of monitoring techniques and protocols for geologic storage projects. IEA GHG R&D Programme. July 2004.

Benson, S., 2004. Monitoring protocols and life-cycle for geologic storage of carbon dioxide. Proceedings of the Carbon Sequestration Leadership Forum. Melbourne, Australia. 13-15 September.

Benson, S., 2006. Monitoring carbon dioxide sequestration in deep geological formations for inventory verification and carbon credits. Proceedings of the 2006 SPE Annual Technical Conference and Exhibition. San Antonio, TX. 24-27 September.

Burton, M., Bryant, S., 2007. Eliminating buoyant migration of CO_2 through surface dissolution: implementation costs and technical challenges. SPE 110650. SPE Ann. Tech. Conf. Exhib. Anaheim, CA.

Wyoming Carbon Sequestration Working Group (CSWG), 2009. Report and recommendations of the carbon sequestration working group to the joint minerals, business and economic committee and the joint judicial committee of the Wyoming state legislature. Corra, J., Doll, T., Surdam, R., Andrews, I., Brokaw, R., Frederick, K., Freudenthal, N., Green, B., Henricks, K., Northam, M., Witham, L. September 2009.

Cheng, C., Gragg, M., White, M., Lemiszki, P., McKay, L., 2013. Sensitivity of injection costs to input petrophysical parameters in numerical geologic carbon sequestration models. Int. J. Greenh. Gas Control, 18, 277-284.

U.S. Energy Information Administration (EIA), 2012. Annual Energy Review 2011. DOE/EIA-0384. September 2012. http://www.eia.gov/totalenergy/data/annual/pdf/aer.pdf, retrieved January 2014.

U.S. Energy Information Administration (EIA), 2013. Annual Energy Outlook with Projections to 2040. DOE/EIA-0383. April 2013. http://www.eia.gov/forecasts/aeo, retrieved January 2014.

U.S. Energy Information Administration (EIA), 2014. Electricity Data Browser. http://www.eia.gov/data/browser, retrieved January 2014.

Eke, P., Naylor, M., Haszeldine, S., Curtis, A., 2009. CO_2 -Brine surface dissolution and injection: CO_2 storage enhancement, Publication SPE 124711, Proceedings of the 2009 SPE Offshore Europe Oil & Gas Conference & Exhibition.Aberdeen, UK.

Environmental Protection Agency (EPA), 2010a. Geologic CO_2 sequestration technology and cost analysis. EPA 816-R10-008. November 2010.

Environmental Protection Agency (EPA), 2010b. Cost analysis for the federal requirements under the underground injection control program for carbon dioxide geologic sequestration wells (final GS rule). EPA 816-R10-013. November 2010.

Environmental Protection Agency (EPA), 2011. Underground injection control program class VI financial responsibility guide. EPA 816-R11-005. July 2011.

Environmental Protection Agency (EPA), 2012. Underground injection control program class VI well project plan development guidance. EPA 816-R-11-017. August 2012.

Environmental Protection Agency (EPA), 2013. Geologic sequestration of carbon dioxide: underground injection control program class VI well area of review evaluation and corrective action guidance. EPA 816-R-13-005. May 2013.

Fang, Y., Baojun, B., Dazhen, T., Dunn-Norman, S., Wronkiewicz, D., 2010. Characteristics of CO_2 sequestration in saline aquifers. Pet. Sci., 7, 83-92.

Finsterle, S.,1999. iTOUGH2 User's Guide. Report LBNL-40040. Lawrence Berkeley National Laboratory, Berkeley, CA. Updated 2007.

Finsterle, S., 2006. Demonstration of optimization techniques for groundwater plume remediation using iTOUGH2. Environmental Modeling and Software, 21(5), 665-680.

Finsterle, S., 2014. iTOUGH2 V7.0 command reference. Report LBNL-40041. Lawrence Berkeley National Laboratory, Berkeley, CA.

Gorell, S., 1990. Implications of water-alternate-gas injection, for profile control and injectivity. SPE/DOE 20210. Proceedings SPE/DOE Seventh Symposium on Enhance Oil Recovery. Tulsa, Oklahoma. April 22-25, 1990.

Heddle, G., Herzog, H., Klett, M., 2003. The economics of CO_2 storage. MIT LFEE 2003-003 RP, Massachusetts Institute of Technology.

Ide, S., Jessen, K., Orr, F., 2007. Storage of CO_2 in saline aquifers: effects of gravity, viscous, and capillary forces on amount and timing of trapping. Int. J. Greenh. Gas Control, 1(4), 481-491.

International Energy Agency Greenhouse Gas R&D Programme (IEAGHG), 2005. Building the cost curves for CO_2 storage: North America. Report 2005/3. February 2005.

International Energy Agency Greenhouse Gas R&D Programme (IEAGHG), 2010. Injection Strategies for CO_2 Storage Sites, 2010/04

Jain, L., Bryant, S., 2011. Optimal design of injection/extraction wells for surface dissolution CO_2 storage strategy. Energy Procedia, 4, 4299-4306.

Joshi, S., 2003. Cost/Benefit of horizontal wells. Society of Petroleum Engineers, SPE 83621.

Juanes, R., Spiteri, E.J., Orr, F.M., Blunt, M.J., 2006. Impact of relative permeability hysteresis on geological CO_2 storage. Water Resour. Res. 42, W12418.

Kaiser, M., 2007. A Survey of Drilling Cost and Complexity Estimation Models. International Journal of Petroleum Science and Technology, 1(1), 1-22.

Keith, D., Hassanzadeh, H., Pooladi-Darvish, M., 2005. Reservoir engineering to accelerate dissolution of CO_2 in brines. Proceedings of 7th International Conference on Greenhouse Gas Control Technologies, Pergamon.

Lake, L. W., 1989. Enhanced Oil Recovery. NJ: Prentice Hall.

Leonenko, Y., D. Keith, 2008. Reservoir engineering to accelerate the dissolution of CO_2 stored in aquifers. Environ. Sci. Technol. 42, 4742.

Leonenko, Y., Keith, D., Pooladi-Darvish, M., Hassanzadeh, H., 2006. Accelerating the dissolution of CO_2 in aquifers. 8TH International Conference on Greenhouse Gas Control Technologies, Trondheim, Norwaym, 19-22 June.

Levenberg, K., 1944. A method for the solution of certain nonlinear problems in least squares. Quart. Appl. Math., 2, 164–168.

Mathias, S., Gluyas, J., Gonzalez Martinez, M., Bryant, S., Wilson, D., 2013. On relative permeability data uncertainty and CO2 injectivity estimation for brine aquifers. Int. J. Greenh. Gas Control, 12, 200-212.

Marquardt, D.W., 1963. An algorithm for least squares estimation of nonlinear parameters. SIAM J. Appl. Math., 11, 431–441.

McCoy, S., Rubin, E., 2009. Variability and uncertainty in the cost of saline formation storage. Energy Procedia, 1, 4151-4158.

Michael, K., Neal, P., Allison, G., Ennis-King, J., Hou, W., Paterson, L., Sharma, S., Aiken, T., 2011. Injection strategies for large-scale CO_2 storage sites. Energy Procedia, 4, 4267-4274.

Nasir, F., Chong, Y., 2009. The effect of different carbon dioxide injection modes on oil recovery. International Journal or Engineering and Technology, 9(10), 66-72.

Pires, J., Martins, F., Alvim-Ferraz, M., Simoes, M., 2011. Recent developments on carbon capture and storage: an overview. Chemical Engineering Research and Design, 89, 1446-1460.

Pruess, K., Oldenburg, C., Moridis, G., 1999. TOUGH2 user's guide, version 2.0, Report LBNL-43134, Lawrence Berkeley National Laboratory, Berkeley, CA. Updated September 2012.

Rubin, E., Chen, C., Rao, A., 2007. Cost and performance of fossil fuel power plants with CO_2 capture and storage. Energy Policy, 35, 4444-4454.

Zhang, Z, 2013. Numerical simulation and optimization of CO_2 sequestration in saline aquifers. PhD thesis. Washington University in St. Louis, St Louis, Missouri, May 2013.

Zhang, Z., Agarwal, R., 2012. Numerical simulation and optimization of CO_2 sequestration in saline aquifers for vertical and horizontal well injection. Comput Geosci, 16, 891-899.

Zhang, Z., Agarwal, R., 2013. Numerical simulation and optimization of CO_2 sequestration in saline aquifers for enhanced storage capacity and secured sequestration. Int. Journal of Energy and Environment, 4(3), 387-398.

Zhang,Z., Agarwal, R., 2014. Numerical simulation and optimization of Sleipner carbon sequestration project. Int Journal of Engineering and Technology, 3(1), 1-13.

Qi, R., LaForce, T.C., Blunt, M.J. 2009. Design of carbon dioxide storage in aquifers. Int. J. Greenh. Gas Control. 3(2), 195‑205

CONCLUSION

This dissertation presented three projects to further the understanding of secondary CO_2 trapping mechanisms in storage systems. The first project compared the storage performance of supercritical CO_2 and dissolved CO_2 injection strategies based on plume distribution and pressure effects using forward numerical simulations. The second project reported on experimental results from an investigation into hysteretic trapping and relative permeability of supercritical CO_2 at reservoir conditions. The third project used inverse modeling techniques to optimize water/CO_2 co-injection schemes based on cost and secondary trapping. Ultimately, results may be used to enhance storage security by designing CO_2 injection strategies that take advantage of CO_2 trapping behavior at targeted depths. The key findings are summarized below.

A Comparison Study of Supercritical CO_2 and CO_2 Saturated Brine Injection Strategies

- There was a difference in results between homogeneous model set-ups and more realistic heterogeneous model set-ups that leads to different conclusions about the storage efficiency of injected CO_2 saturated brine. These differences suggest simple models may not be able to reproduce the behavior of injected dissolved CO_2 in the subsurface accurately.
- Supercritical CO_2 injection would be favorable in highly heterogeneous dipping formations where the mobility ratio to brine is quickly reduced, favoring stable flow. Dipping formations enhance secondary trapping and immobilized the CO_2 plume in less time that injection into flat-lying aquifers.

- Dissolved CO_2 injection resulted in much larger areal extents than $scCO_2$ injection within the more realistic model set-ups. In simple models, the pressure build up was 1.5-2.3 times greater than standard $scCO_2$ injection. These results will limit the possibilities for storage locations, as dissolved injection will require a larger area.
- Further work is recommended to explore possibilities of dissolved CO_2 injection via existing Class II brine disposal wells.

Hysteretic Trapping and Relative Permeability of CO_2 in Sandstone at Reservoir Conditions

- There was a strong residual trapping dependence on the saturation history of the core for the nonwetting CO_2 phase.
- A linear trapping model previously developed for applications in multiphase contaminant transport was fit to data with a value of 0.5 describing the relationship between the turning point CO_2 saturations and the residual CO_2 saturations of each respective cycle.
- Van Genuchten-Burdine models were shown to fit data after incorporating a linear trapping model into nonwetting phase calculations.
- Based on these results, it is important to characterize the trapping relationship within target formations and employ hysteretic trapping models into relative permeability curves to properly simulate subsurface CO_2 storage.

- Results also demonstrated the need to improve experimental techniques to measure end point relative permeability in the case of fluid pairs with strong viscosity contrast.

Cost Effective CO_2 Storage Design to Enhance Secondary Gas Trapping

- Water alternating gas (WAG) injection increased CO_2 trapping to 64%, 22% over the standard injection strategy while reducing costs by \$0.16/tCO_2. This method also reduced costs the fastest, compensating for additional capital costs within 5-10 years from start of injection.
- Simultaneous water and gas (SWAG) injection reduced costs the most, by \$0.31/tCO_2. It increased trapping to 86%, 44% more than standard injection.
- The post-CO_2 injection water flush increased trapping with the least additional water use, at 2.4 billion gallons. The water flush method improves trapping by 7% without increasing costs. It is suggested to use this method in conjunction with another successful co-injection method to optimize trapping.
- Dissolved CO_2 injection was unable to reduce the cost function, but trapped the most CO_2 of any method. This method may prove more economical when integrated into pre-existing brine disposal operations, where the capital costs are reduced.
- Direct water/CO_2 co-injection was unable to reduce cost or significantly increase CO_2 trapping.

APPENDICIES

Appendix A

Plume results summary tables.

Table A-1. Areal Plume Extent and Storage Efficiency. A_{max} is the maximum areal extent and A_{cap} is the extent of the dissolved CO_2 plume along the caprock. 20 years is the end of injection, 100 years is the end of monitoring period.

	$scCO_2$ Injection		**Dissolved CO_2 Injection**		
Formation Case	A_{max}	S_E	A_{max}	S_E	A_{cap}
Homogeneous					
20 years	2.41 km^2	0.035	1.99 km^2	0.042	1.84 km^2
100 years	4.30 km^2	0.019	2.09 km^2	0.040	1.79 km^2
Stratified					
20 years	2.23 km^2	0.036	2.05 km^2	0.042	1.91 km^2
100 years	4.19 km^2	0.020	2.06 km^2	0.041	1.91 km^2
Heterogeneous 1 (flat)					
20 years	5.1 km^2	0.016	15.9 km^2	0.005	5.9 km^2
100 years	6.2 km^2	0.014	15.9 km^2	0.005	5.9 km^2
Heterogeneous 2 (dipping)					
20 years	3.7 km^2	0.022	16.1 km^2	0.005	5.9 km^2
100 years	6.6 km^2	O(300 m)	16.2 km^2	O(300 m)	5.8 km^2

Table A-2. Maximum plume velocity and Mobility Ratios. Velocity ratio given for comparison of injection strategy. 20 years is the end of injection, 100 years is the end of monitoring period.

	Darcy Velocity		**Velocity Ratio** ($scCO_2$/Diss. CO_2)	**Mobility Ratio** ($scCO_2$/water)
Formation Case	*$scCO_2$*	*Diss. CO_2*		
Homogeneous				
20 years	10 cm/d	6 cm/d	1.67	9
100 years	3 mm/d	0.7 mm/d	4.29	9
Stratified				
20 years	10 cm/d	7 cm/d	1.43	10
100 years	5 mm/d	0.7 mm/d	7.14	10
Heterogeneous 1 (flat)				
20 years	5 m/d	32.9 m/d	0.15	9
100 years	7 mm/d	4 mm/d	1.75	9
Heterogeneous 2 (dipping)				
20 years	1.1 m/d	33 m/d	.03	10
100 years	1.7 cm/d	4.6 mm/d	0.37	<1

Appendix B

Error Propagation Derivation

The error propagation for relative permeability was estimated using the variances of the sources. The general form is given by (Ku, 1966):

$$\sigma_{\mathrm{f}} = \left(\left(\frac{\partial f}{\partial x} \right)^2 \sigma_{\mathrm{x}}{}^2 + \left(\frac{\partial f}{\partial y} \right)^2 \sigma_{\mathrm{y}}{}^2 \right)^{\frac{1}{2}} \tag{A-1}$$

where σ_{f} is the standard deviation of f and f is a function of x and y. The assumption is x and y are uncorrelated. For this experiment, standard deviations of relative permeability were calculated from error in absolute permeability and pressure drop measurements as follows:

$$\sigma_{\mathrm{k}_{\mathrm{r}\beta}} = \left(\left(\frac{\partial k_{\mathrm{r}\beta}}{\partial k} \right)^2 \sigma_{\mathrm{k}}{}^2 + \left(\frac{\partial k_{\mathrm{r}\beta}}{\partial \Delta P} \right)^2 \sigma_{\Delta P}{}^2 \right)^{\frac{1}{2}} \tag{A-2}$$

where $k_{r\beta}$ is the relative permeability to phase β, k is the representative absolute permeability and ΔP is the average pressure drop per fractional flow, σ_{k} is the standard deviation absolute permeability, and $\sigma_{\Delta \mathrm{P}}$ is the standard deviation in the average pressure drop.

Substituting into equation A-2 yields,

$$\sigma_{k_{r\beta}} = \left(\left(\frac{Q_\beta \mu_\beta L}{Ak^2 \Delta P} \right)^2 \sigma_k{}^2 + \left(\frac{Q_\beta \mu_\beta L}{Ak \Delta P^2} \right)^2 \sigma_{\Delta P}{}^2 \right)^{\frac{1}{2}} \quad \text{(A-3)}$$

Simplifying equation A-3,

$$\sigma_{k_{r\beta}} = \left(k_{r\beta}{}^2 \left(\left(\frac{\sigma_k}{k} \right)^2 + \left(\frac{\sigma_{\Delta P}}{\Delta P} \right)^2 \right) \right)^{\frac{1}{2}} \quad \text{(A-4)}$$

The standard deviation in the average pressure drop includes deviations during relative permeability experiments. Standard deviation in pressure drop measurements during relative permeability experiments used the variance over the last 1.8 pore volumes of recorded points for each fractional flow. This corresponds to near 110 points over 8 minutes per fractional flow. The resulting standard deviations used for $\sigma_{\Delta P}$ are given in Table 3.4.

Results show the magnitude of error does not disrupt important trends exhibited by data (Table A-3 and A-4).

Table A-3. Results by fractional flow of CO_2 show standard deviations calculated for CO_2 relative permeability data. Shown for drainage/imbibition cycles *A*, *B*, and *C*.

Cycle A			
	ff_{CO_2}	k_{rCO_2}	$\sigma_k_{rCO_2}$
Dr.	0.00	0.000	0.0000
	0.50	0.017	0.0005
	0.80	0.031	0.0009
Imb.	0.78	0.030	0.0009
	0.76	0.027	0.0009
	0.70	0.022	0.0007
	0.67	0.021	0.0007
	0.64	0.019	0.0006
	0.58	0.016	0.0005
	0.47	0.011	0.0003
	0.40	0.009	0.0003
	0.25	0.005	0.0001

Cycle B			
	ff_{CO_2}	k_{rCO_2}	$\sigma_k_{rCO_2}$
Dr.	0.75	0.027	0.0007
	0.93	0.047	0.0012
	0.99	0.068	0.0017
Imb.	0.97	0.065	0.0020
	0.96	0.058	0.0018
	0.94	0.051	0.0016
	0.91	0.043	0.0014
	0.88	0.037	0.0012
	0.80	0.026	0.0008
	0.70	0.018	0.0006
	0.60	0.013	0.0004
	0.30	0.004	0.0001

Cycle C			
	ff_{CO_2}	k_{rCO_2}	$\sigma_k_{rCO_2}$
Dr.	0.85	0.035	0.0008
	0.95	0.051	0.0012
	0.995	0.072	0.0016
	1.00	0.357	*
Imb.	0.97	0.065	0.0014
	0.90	0.036	0.0008
	0.50	0.006	0.0001
	0.05	0.000	0.0000

Table A-4. Results by fractional flow of CO_2 show standard deviations calculated for water relative permeability data. Shown for drainage/imbibition cycles *A*, *B*, and *C*.

Cycle A			
	ff_{CO_2}	k_{rw}	σ_k_{rw}
Dr.	0.00	1.000	0.0000
	0.50	0.405	0.0114
	0.80	0.186	0.0052
Imb.	0.78	0.199	0.0063
	0.76	0.204	0.0064
	0.70	0.227	0.0071
	0.67	0.241	0.0076
	0.64	0.256	0.0080
	0.58	0.269	0.0085
	0.47	0.289	0.0091
	0.40	0.301	0.0095
	0.25	0.318	0.0100

Cycle B			
	ff_{CO_2}	k_{rw}	σ_k_{rw}
Dr.	0.75	0.215	0.0052
	0.93	0.084	0.0021
	0.99	0.016	0.0004
Imb.	0.97	0.047	0.0015
	0.96	0.057	0.0018
	0.94	0.077	0.0024
	0.91	0.101	0.0032
	0.88	0.120	0.0038
	0.80	0.153	0.0048
	0.70	0.179	0.0057
	0.60	0.199	0.0063
	0.30	0.226	0.0071

Cycle C			
	ff_{CO_2}	k_{rw}	σ_k_{rw}
Dr.	0.85	0.148	0.0034
	0.95	0.064	0.0015
	0.995	0.009	0.0002
	1.00	0.000	*
Imb.	0.97	0.048	0.0010
	0.90	0.094	0.0021
	0.50	0.146	0.0032
	0.05	0.163	0.0036